UNIFICATION OF ELECTRON EMISSION MECHANISMS: FROM LIQUIDS TO LASERS
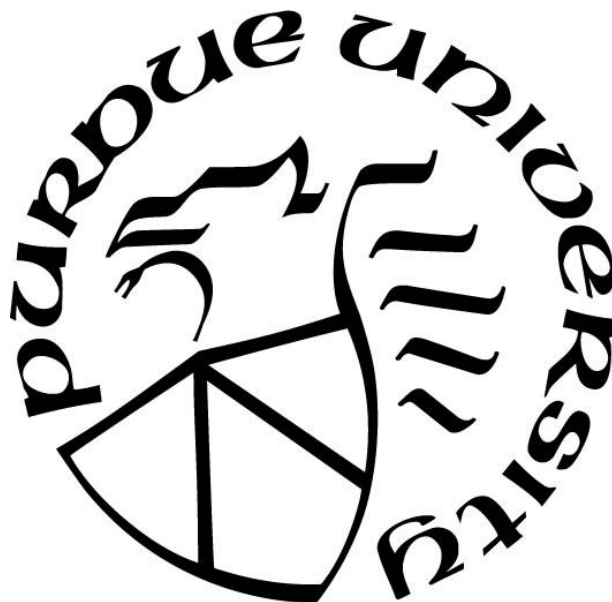
by

Sarah Ashley Lang

A Thesis

Submitted to the Faculty of Purdue University

In Partial Fulfillment of the Requirements for the degree of

Master of Science in Nuclear Engineering

School of Nuclear Engineering

West Lafayette, Indiana

December 2020

THE PURDUE UNIVERSITY GRADUATE SCHOOL
STATEMENT OF COMMITTEE APPROVAL

Dr. Allen Garner, Chair

School of Nuclear Engineering

Dr. Robert Bean

School of Nuclear Engineering

Dr. Jonathan Poggie

School of Aeronautics and Astronautics

Approved by:

Dr. Seungjin Kim

Dedicated to everyone who believed in me.

ACKNOWLEDGMENTS

I wish to express my gratitude to my advisor, Dr. Allen Garner, who provided the guidance and support I needed to continue my academic career. He allowed me to build upon my strengths and weakness by accepting me into his research group and giving me the opportunity to grow in my endeavors. Due to his dedication to help his students, I was able to flourish as a student, researcher, and a professional. His provision of funding through a grant he was awarded from the Air Force Office of Scientific Research allowed me to focus solely on the research at hand.

I would also like to recognize Dr. Robert Bean and Dr. Jonathan Poggie who provided invaluable assistance as my committee members.

I wish to thank the members of the BEEP lab group for their continued support and advice regarding presentations, academics, and other professional aspects of my life.

I would like to pay special regards to my roommates and friends, Thor, Nathan, and Jacob; the insight from their graduate school experience was invaluable.

I would like to express my appreciation and gratitude to my father and mother. My parents made it possible for me to progress this far with their support and guidance in all aspects of my life. Finally, I would like to thank my brother, Andrew, who has been a constant friend filled with understanding.

TABLE OF CONTENTS

LIST OF TABLES

LIST OF FIGURES

ABSTRACT

Electronic processes, such as electronic breakdown and electron emission, in gases and liquids have implications in microplasmas, laser applications, water purification, biomedical applications, geographical mapping, and radiation detection. Electron emission and breakdown mechanisms are heavily researched and characterized in gases. Much of the current research into these mechanisms is focused on unifying breakdown and emission mechanisms. For electron emission, these mechanisms include field emission (FE), space-charge-limited emission (SCLE), thermionic emission (TE), and photoemission (PE), while gas breakdown emission mechanisms include Paschen's law (PL) and Townsend breakdown (TB) with ion-enhanced FE becoming important at microscale. This research first unified SCLE and FE in vacuum and has been extended to include SCLE with collisions (for a gas at non-vacuum) and TE. This thesis extends this approach in electron emission unification, referred to as "nexus" theory, in two directions. First, we will apply this theory to liquids to examine the transition from FE to SCLE and hypothesize about the implications should there be a phase change. Second, we will incorporate PE, which becomes important with increasing interest in ultrafast laser phenomena at nanoscale and development of solar cells, with SCLE, TE, and FE.

Initial nexus theory studies included gas at non-vacuum pressures by including electron mobility in the electron force law. In principle, this behavior should be the same whether the medium is air or liquid. Electron emission and breakdown, which can arise from field emission, are increasingly important in plasma water treatment, pulsed power systems, radiation detection, and even understanding the physics of high electric fields applied to liquid helium for the Spallation Neutron Source. To demonstrate the applicability of nexus theory to liquids, we fit experimental data for electron emission in hydrocarbons to the full theory unifying FE to SCLE with and without collisions. The measured current followed Fowler-Nordheim scaling for FE at lower voltages with space charge beginning to contribute at higher voltages; none of the hydrocarbons study fully transitioned to Mott-Gurney (SCLE with collisions) scaling within the experimentally studied parameter range. Considering a higher mobility representative of a vapor in the theory demonstrates the feasibility of achieving Child-Langmuir (SCLE in vacuum) scaling for the gaps of the size considered experimentally. Thus, this approach may ultimately be applied to model electron emission during both phases changes and transitions between the mechanisms.

We next extended the gas nexus theory to analyze the transitions between PE and the other emission mechanisms. We modified the previous theory that used the generalized thermal-field emission (GTF) theory for electron current to instead use the generalized thermal-field photoemission (GTFP) theory. Using this, we obtained exact solutions for current as a function of applied voltage and demonstrated the asymptotic behavior with regard to the modified Fowler DuBridge (MFD) equation, which models PE. We combined the MFD equation with the other asymptotic solutions to develop state diagrams unifying the various emission mechanisms to provide guidance to the mechanisms and transitions relevant under various conditions of mobility, gap distance, temperature, and laser energy/wavelength/frequency. These diagrams provide guidance on which asymptotic solution or more detailed theory would be necessary to accurately relate current and voltage under various operating conditions.

1. INTRODUCTION

Electronic processes are widely researched in various media due to their importance for numerous fields and industries, such as vacuum electronics (Brayfield *et al*., 2019; Brodie and Schwoebel, 1994; Fu *et al*.; Garner *et al*., 2020a; Go *et al*., 2014; Jensen, 2018; Johnson and Oskam, 1971; Zhang *et al*., 2017), particle accelerators (Birdsall *et al*. 1966; Humphries *et al*. 1990; Reiser, 1994), nuclear applications (Chu *et al*., 1980; Lopes and Chepel, 2003; Schmidt, 1984), geological applications (Caulfield, 1962; Jones and Kunhardt, 1995b; Olson and Sutton, 1993; Rechtien *et al*., 1993; Vogel, 1952), pulsed power (Garner *et al*., 2017; Schoenbach *et al*., 2008;Zahn *et al*., 1986), lasers (Brau, 1998; Jensen *et al*., 2006a; Jensen *et al*., 2006b; O'Shea *et al*., 1993; O'Shea, 1998; O'Shea and Freund, 2001), plasma biology (Xu *et al*., 2017; Xu *et al*., 2017), combustion (Bankston *et al*., 1988;Krejci *et al*., 2017), and propulsion (Gaskell, 1997; Krejci *et al*., 2017; Lemmer, 2017; Levchenko *et al*., 2020; Loscertales and de la Mora, 1995; Marcuccio *et al*., 1998; Toijala *et al*., 2019). The applications relevant to these fields and industries depend on two fundamental electronic processes: charged particle emission and breakdown. Both charged particle emission and breakdown are described by various mechanisms that vary depending on system parameters, such as temperature, pressure, voltage, electric field, experimental geometry, or material characteristics. This thesis examines specifically charged particle emission and unification of emission mechanisms with the ultimate objective (beyond the scope of this thesis) of unifying emission and breakdown.

Charged particle emission is the release of an ion or electron due to certain conditions such as temperature, pressure, electric field, material, or geometry. This emission is typically explained by four main emission types: field emission (FE), thermionic emission (TE), space charge limited emission (SCL), and photoemission (PE) (Fowler and Nordheim, 1928; Jensen, 2017; Zheng *et al*., 2017). Many theories have been developed to explain the different emission types based on different conditions, and these equations and laws have been adapted as other factors have been discovered; however, there are a few main theories that are still used to describe the individual emission mechanisms. Fowler-Nordheim (FN) described the process of FE, which occurs when there is a strong electric field (Fowler and Nordheim, 1928; Jensen, 2018; Lau *et al*., 1994; Murphy and Good, 1956). The Richardson-Laue-Dushman (RLD) equation is one equation used to describe TE; this is the processes in which electrons are released due to the high temperature of the surface

(Dushman, 1923; Dushman, 1930; Jensen, 2018; Millikan and Eyring, 1926; Modinos, 1984; Murphy and Good, 1956; Richardson, 1916; Richardson and Young, 1925). The third emission mechanism, SCL, can be described by two theories. The first theory is the Child-Langmuir (CL) equation which describes SCL in vacuums (Child, 1911; Jensen, 2018; Langmuir, 1913; Millikan and Eyring, 1926). The second theory is the Mott-Gurney (MG) equation which describes SCL with collisions (Darr *et al.*, 2019a; Mott and Gurney, 1940); this theory incorporates the charge mobility of the gas or liquid being analyzed, which is dependent on numerous conditions. One of the main theories that models PE is the Fowler-DuBridge (FD) equation (Dushman, 1923; DuBridge, 1932; DuBridge and Roehr, 1932; Fowler, 1931; Jensen, 2018); PE occurs when electrons are released due to light striking the surface of the material. Although these are the main theories and equations used to describe electron emission, there are other theories that connect the main theories and account for other effects.

Electron emission has been determined to be one of the causes of electronic breakdown which makes research on the transition between electron emission and breakdown common (Auger *et al.*, 2016; Phan *et al.*, 2020; Qian *et al.*, 2005). Similar to electron emission, breakdown is often separated into different mechanisms to describe the unique processes that occur with different conditions and factors. A few of the theories that describe breakdown and the processes involved are Paschen's law (PL) (Paschen, 1889), sometimes referred to as Paschen's curve (PC), Townsend breakdown (TB) (Townsend, 1901; Townsend, 1915), streamer theory (Loveless and Garner, 2017b), and arcing (Kunhardt, 1980). Paschen's law (PL) and TB are the two most well-known theories that describe the onset of breakdown. Streamer theory and arcing are two processes that follow TB. The process of breakdown is important to numerous fields and industries which means that understanding the processes is fundamental to developing new technologies.

Electron emission and breakdown are heavily researched areas due to the potential applications. However, the majority of the previous research focused on one or two theories related to the different processes. Now, the current focus surrounding these fundamental processes is unifying the different theories of electron emission and breakdown. The unification process for the electron emission and breakdown in gases has been relatively successful. This includes the unification of FN, CL, and MG in gases (Darr *et al.*, 2019a), the unification of microscale and macroscale breakdown (Kunhardt, 1980; Loveless and Garner, 2016; Loveless and Garner, 2017a; Loveless and Garner, 2017b), and the unification of FN, RLD, and general thermal field (GTF)

(Jensen, 2018). GTF can be adapted to account for PE (Jensen *et al.*, 2002; Jensen, 2007; Jensen and Cahay, 2006; Jensen, 2018; Jensen, 2019). More recently TE was added to the unification of FN, CL, and MG in gases (Darr *et al.*, 2020). The unification of these different breakdown and emission theories is widely studied in gases; however, they are not heavily researched in the other phases. Understanding the transitions between the mechanisms in liquids, solids, or gas phases could provide useful information regarding which mechanism dominates in the different phases at certain conditions. Once there is an understanding about the transitions in liquids, research into the transitions between phases could be useful for applications that occur at higher temperatures.

Although electronic breakdown and emission are widely researched, there are numerous ways in which theories and experiments can be extended or adapted to model certain conditions. A few gaps in the research for these processes include experimental geometries, lack of uniform mobility studies, and the unification of emission or breakdown mechanisms in different phases; these gaps provide opportunities to further develop the understanding of these electronic processes. Updating the experimental geometries to make the data more consistent or testing new geometries are two avenues of research for investigating the effects of geometry. The mobility of a material is a fundamental value that influences breakdown and emission mechanisms; conducting an extensive study regarding the mobility of different liquids could provide more insight into how the mobility affects emission and breakdown. Finally, the unification of different electronic mechanisms could be further investigated by adding more emission mechanisms or looking at the unification in multiple phases; this could be further developed to look at how the emission mechanisms model the transitions between the phases of the material. These are just few of the many research areas that could be explored to further understand electron emission and electronic breakdown.

Electron emission and electronic breakdown are the foundational processes described in this research; however, electron emission is the main focus of the research. Electronic breakdown is included to highlight how this research could be used in industries and how it could be extended. The goal of this introduction is to provide a literature review containing the fundamental background knowledge regarding the basic theories of electron emission and electronic breakdown. Due to the extensive research regarding these processes, the introduction focuses on the basic theories and variables related to the processes. Chapter 1 is the introduction which includes the literature review. Section 1.1 includes the motivation for conducting this research; it provides brief

descriptions on potential applications. Section 1.2 reviews the theories and background information regarding electron emission and breakdown in different material phases. Section 1.3 provides an extensive review of the electron mobility which is an important variable for emission. Section 1.4 concludes the introduction, and section 1.5 defines the scope of the thesis.

1.1 Motivation

Electron emission and breakdown in various states of matter have important potential implications in fields for health, safety, and power. Electronic processes in gases are important for pulsed power applications, lasers, transmission lines, combustion, and medical applications. Similar to gases, electronic processes in liquids provide the foundational knowledge for numerous fields. This section highlights a few of the potential applications for electron emission and breakdown in liquids and gases. Figure 1.1 highlights the different fields that are affected by electron emission and breakdown.

• Structure of Liquids • Interaction of Low Energy Electrons with Condensed Matter 1	• Electronic States of the Condensed Liquid Phase • Optical and Transport Properties of Charge Carriers 2	• Physics of Insulators • Electron Localization • Traps, Band Structure 3
• Radiation Physics and Radiation Chemistry • Photophysics and Photochemistry • Ionization and Electron Transfer 4	Electric Processes in Dielectric Liquids	• Electric and Laser- Induced Breakdown • Properties of Composite insulation • Oil Filled Transformers 5
• Electrochemistry • Field Induced Polymerization • Ion Radial Chemistry 6	• Nuclear Radiation Detectors and Detectors for High Energy Physics • Liquid Ionization Chambers for Dosimetry • Imaging Devices in Medical Physics 7	• Electrostatic Generators • Power Capacitors • Pulsed Power Apparatus • Flow of Hydrocarbons 8

Figure 1.1. The research areas that use electronic processes in liquids (Schmidt, 1984)

Applications that fall under the fields included in Figure 1.1 are radiation measurement (Schmidt, 1984), combustion (Bankston *et al.*, 1988; Krejci *et al.*, 2017), acoustic devices (Jones and Kunhardt, 1995a), sonar (Naugolnykh and Roy, 1974), decontamination (Foster, 2017; Xu *et al.*, 2017), geological experimentation (Olson and Sutton, 1993; Rechtien *et al.*, 1993), pulsed power systems (Garner *et al.*, 2017; Zahn *et al.*, 1986), or electrospray devices (Toijala *et al.*, 2019). The

18

applications highlighted in this section include radiation measurement, decontamination, geological, pulsed power, and electrospray applications; each of these fields provides a unique perspective on why electronic processes in liquids is an important area of research.

1.1.1   Radiation Measurement

Radiation measurement includes applications used for medical processes and radiation detection. One radiation detection system being researched is liquid ionization chambers for dosimetry (Chu *et al*., 1980) and X-rays (Schmidt, 1984). Liquid ionization chambers record the ionization due to radiation; these chambers provide information regarding the individual doses from neutrons and gammas in a mixed-neutron field and the spatial resolution of the radiation field (Chu *et al*., 1980). Liquid Rare Gas Detectors (LRGD) use rare gases, such as xenon, argon, or krypton, in their liquid form (Lopes and Chepel, 2003) to measure the radiation because they provide better resolution and can be used as scintillators (Lopes and Chepel, 2003). These are only two types of the numerous radiation detectors that use the ionization of liquids.

1.1.2   Decontamination

There are millions of people without clean drinking water, and electronic processes could be used to form plasmas which can potentially purify water sources to provide clean drinking water (Foster, 2017). The water purification systems currently available remove most of the harmful substances, but these conventional systems cannot remove all of the containments. To remove these pollutants, researchers are looking at advanced oxidation using plasmas (Foster, 2017). The electronic processes of interest for this research are pre-breakdown and break-down processes, and the most pertinent mechanism for water purification is bubble formation (Foster, 2017). The bubbles form causing field enhancement which makes it more likely for FE to occur which in return leads to the beginning of an avalanche process; the processes can be used to remove pollutants from water. In addition to contaminants in water, these bacteria and microorganisms can also affect food. Some foods and beverages are thermally pasteurized, but this method can have unwanted effects. One method that has been proposed to replace thermal pasteurization is treatment by high voltage atmospheric cold plasma (Xu *et al*., 2017) or pulsed electric fields

(Garner, 2019). This treatment method uses plasmas generated by basic electric processes in gases and liquids.

1.1.3 Geological

Geological and seismic applications include mapping the ocean floor (Caulfield, 1962; Olson and Sutton, 1993), analyzing bore holes (Olson and Sutton, 1993; Rechtien *et al.*, 1993; Vogel, 1952), and exploring for oil (Caulfield, 1962; Jones and Kunhardt, 1995b; Olson and Sutton, 1993). These applications typically use explosives to provide sound waves, and research has shown that these explosives could be replaced by electrical arcs (Olson and Sutton, 1993). Therefore, the primary mechanism of interest for these applications is arc formation (Olson and Sutton, 1993; Rechtien *et al.*, 1993; Vogel, 1952). The sound produced from the arc formation is then used to classify different materials and landmarks under the water.

1.1.4 Pulsed Power and Insulation

In pulsed power systems, liquids are used for electric insulation and heat transfer agents (Zahn *et al.*, 1986). Dielectrics are the main liquids used because of their insulating capabilities, but some devices also used water for the system. Using liquids in transmission lines to store electrical energy can result in reduced length of the transmission lines (Schoenbach *et al.*, 2008). The length of the transmission line is dependent on the pulse duration which scales with $\sqrt{\varepsilon}$ where ε is the permittivity of the liquid. The high permittivity of liquids results in shorter transmission lines (Schoenbach *et al.*, 2008). In addition, liquids can potentially allow for the rapid exchange of electrical energy between the transmission lines and the switches (Schoenbach *et al.*, 2008). Liquid insulating systems can handle higher operating electrical stresses than gas systems (Jones and Kunhardt, 1995b). These pulsed power systems can also be used for medical applications (Garner *et al.*, 2017) such as treating cancer (Schoenbach *et al.*, 2008). The potential cancer treatments use electric fields to create pores in the cells in which medicine can be injected; this process is known as electroporation (Neal *et al.*, 2014). Another cancer treatment these systems can be used for is electrochemotherapy (Neal *et al.*, 2014).

1.1.5 Electrospray

Field emission is important for electrospray (ES) applications (Toijala *et al*., 2019) because it is a potential source of small ions (Loscertales and de la Mora, 1995). ES can be used for various applications such as mass spectrometry (MS) (Gaskell, 1997) or space applications (Krejci *et al*., 2017; Lemmer, 2017). A very basic definition of ES is that it applies electrical forces to atomize liquids (Jaworek, 2007). Droplet formation, droplet shrinkage, and gaseous ion formation are the three stages of the process (Gaskell, 1997).

Electrospray is used for MS, bioelectrics, and space applications. Mass spectrometry is used to identify materials in certain substances. For this process, an unknown substance is fed into the system in which the process helps identify the substance or compound (Gaskell, 1997). For bioelectrics applications, it can potentially be used to identify malignant or benign skin lesions (Margulis *et al*., 2018), and it could be used for delivering drugs to the body (Wu *et al*., 2012). Another application for this process is for thrusters in spacecraft (Krejci *et al*., 2017; Lemmer, 2017). ES thrusters are a type of electric propulsion (Lemmer, 2017). "Electrospray thrusters are a class of electric thrusters that produce thrust by acceleration of ions or droplets after extraction from an electrically conductive liquid surface under an applied electrostatic field," (p.447, Krejci *et al*., 2017).

1.2   Theory

Electron emission and breakdown research are heavily intertwined for both gases and liquids. This section reviews electron emission and breakdown in gases separately from that in liquids because the majority of the fundamental processes were first derived for gases. This section has a subsection that describes the most relevant theories for each emission mechanism. It is important to note that much of the research regarding these electron emission mechanisms is intertwined. There is a subsection dedicated to work that unifies these theories.

1.2.1   Breakdown and emission in gases

Emission

Electron and ion emission are often divided into the following mechanisms: FE, TE, SCLE with and without collisions, and PE. The following sections will briefly describe each mechanism.

Field Emission (FE)

FE is one of the most commonly researched electron emission mechanism; due to the frequent use, the equations used to model FE have been continuously adapted and corrected. FE occurs when the electric field becomes sufficiently strong to strip electrons from the cathode (Darr *et al.*, 2019; Jensen, 2017; Jensen, 2018; Lau *et al.*, 1994; Zhang *et al.*, 2017). In 1928, Fowler and Nordheim derived what is now known as the Fowler-Nordheim (FN) law, given by (Fowler and Nordheim, 1928)

$$J_{FN}(V) = A_{FN}E^2 \exp\left(-\frac{B_{FN}}{E}\right), \tag{1.1}$$

where E is the electric field, A_{FN} and B_{FN} are semi-empirically determined FN constants that depend on the material under study, and Φ is the work function (WF). While A_{FN} and B_{FN} may be described in a number of ways, one set of definitions is given by

$$A_{FN} = (1.4/\Phi) \times 10^{-6+4.26/\sqrt{\Phi}} \tag{1.2}$$

$$B_{FN} = 6.49 \times 10^9 \Phi^{1.5}, \tag{1.3}$$

with typical values of $A_{FN} \approx 6.85 \times 10^{-6} \ A \cdot V^{-2}$ and $B_{FN} \approx 6.85 \times 10^9 \ V \cdot m^{-1} eV^{-1.5}$ (Darr *et al.*, 2019a; Lau *et al.*, 1994).

The FN equation may also be adapted in an alternative form to account for other effects. Two prominent effects for all emission mechanisms are geometry and emitter surface. Incorporating the field enhancement factor, β, which typically varies between 1.15 and 115, into the equation can account for the emitter's surface properties (Bhattacharjee *et al.*, 2008; Bhattacharjee and Chowdhury, 2009). Common models also account for image correction factors, $v(y)$ and $t^2(y)$, given by (Bhattacharjee *et al.*, 2008; Gomer, 1994)

$$t^2(y) \approx 1.1 \tag{1.4}$$

$$v(y) \approx 0.95 - y^2 \tag{1.5}$$

$$y \approx 3.79 \times 10^{-4} \sqrt{\beta E}/\varphi. \tag{1.6}$$

are added to the equation; φ is the WF corrected for the Schottky barrier. This leads to an alternative description of the FN equation given by

$$J_{FN} = C_{FN}E_s^2 \exp(-D_{FN}/E_s^2). \tag{1.9}$$

where (Garner *et al.*, 2020a; Loveless and Garner, 2017b)

$$C_{FN} = \frac{A_{FN}\beta^2}{\varphi t^2(y)} \exp\left[\frac{(3.79 \times 10^{-4})^2 B_{FN}}{\varphi^{\frac{1}{2}}}\right] \tag{1.7}$$

$$D_{FN} = 0.95\, B_{FN}\varphi^{\frac{3}{2}}\big/\beta . \tag{1.8}$$

While other modifications have been made to the FN equation to account for more of the physics involved, these details are beyond the scope of this thesis.

To determine the validity of fitting data to FN, one can perform an orthodoxy test (Forbes, 2012; Forbes, 2013; Forbes *et al*., 2015). Forbes developed a quantitative test to determine whether the data satisfies the hypothesis and its assumptions (Forbes, 2013). This test involves calculating the range of a scaled barrier field based on the horizontal axis data, which is used to find the slope of the FN region; this range is considered the extracted range. If the range is within bounds for the particular emitter material, it is considered reasonable. Forbes created this test using data from numerous emission experiments to develop his criteria.

Thermionic Emission (TE)

Another important electron mechanism discussed/theorized in the late 19th and early 20th century was TE, which occurs when the temperature of the surface reaches a point causing the release of charged particles. Richardson started researching TE around 1901 (Richardson, 1901; Richardson, 1903), and in 1913, he determined that the coefficient for this emission mechanism had a T^2 dependence (Richardson, 1913; Richardson, 1915; Jensen, 2017), where T is temperature. In 1916, Richardson adapted the base equation for TE, the Nernst heat theorem, to include the work function (WF) (Richardson, 1916; Dushman, 1923; Jensen, 2017); the WF is the amount of energy needed for an electron to escape into the surrounding vacuum, and it is addressed later in the section. In 1918, von Laue confirmed the T^2 dependence (Jensen, 2017). Following the work of Richardson, Dushman further modified the equation to connect the constant from Richardson and von Laue's work to universal constants to model TE (Dushman, 1923; Dushman, 1930; Jensen, 2017; Richardson and Young, 1925). The resulting equation became known as the Richardson-Laue-Dushman (RLD) equation (Dushman, 1923; Dushman, 1930; Jensen, 2017; Richardson and Burndy, 1916; Richardson and Young, 1925) and is given by

$$J_{RLD}(T) = A_{RLD}T^2 \exp\left(-\frac{\Phi}{k_b T}\right), \tag{1.10}$$

where k_b is Boltzmann's constant and A_{RLD} is a constant equal to $(emk_B^2)/(2\pi^2\hbar^3)$.

The Richardson equation was later combined with the Schottky equation to account for the Schottky effect (SE), which includes the potential barrier (Kiziroglou *et al.*, 2008), when modeling TE (Murphy and Good, 1956). Modifying the Richardson equation with the Schottky barrier (SB) yields

$$J_{TE}(T) = A^* T^2 \exp\left(-\frac{q\varphi}{k_b T}\right), \tag{1.11}$$

where q is the elementary charge, A^* is the effective RLD constant, and φ is the WF that accounts for the SB height (Kiziroglou *et al.*, 2008).

As mentioned above, the WF has also been the subject of multiple research studies and experiments. In 1937, Baker and Boltz discussed the relationship of the WF briefly in connection with TE in dielectric liquids. In their research, they noted that the WF will change based on the material in which the electron emission is occurring (Baker and Boltz, 1937). Much research has been completed on how the WF can be calculated; in 1953, Barbour *et al.* determined that the WF can be estimated from the slope of the curve of natural log of the current versus the inverse voltage (Barbour *et al.*, 1953). The WF was thought to have changed throughout the experiment. In 1971, Lang and Kohn developed a model for metals that separated the WF into two parts (Lang and Kohn, 1971), given by

$$\psi_{hkl} = \psi_u + \delta\psi_{hkl} \tag{1.12}$$

where ψ_{hkl} is the WF for the metal, ψ_u is the uniform-background model, and $\delta\psi_{hkl}$ is, the change in the WF due to the change of a crystal face is (Kiejna and Wojciechowski, 1981). Kiejna and Wojciechowski further demonstrated that the material dependence of the WF was strong and depended on the lattice structure (Kiejna and Wojciechowski, 1981).

The complexity often motivates considering a simple definition of WF based on the difference between the Fermi energy level μ_F and the vacuum energy level E_{vac} (Kahn, 2016), which is "the energy level of an electron positioned at rest within a 'few nanometers' outside the solid, i.e. with zero kinetic energy with respect to the sample surface," (p.8, Kahn, 2016). Essentially, μ_F is the highest electron energy level at absolute zero. The basic equation describing the WF is

$$WF = E_{vac} - \mu_F. \tag{1.13}$$

The dependence of the WF on the material due to the lattice structure (Kiejna and Wojciechowski, 1981) and the temperature (Khatoon *et al.*, 2018) continues to be researched. It has also been observed that the type of electron emission can affect the WF. Thermionic emission needs a higher WF (Gomer, 1972), FE deforms the WF (Gomer, 1972), and SCL can lower the WF (Barbour *et al.*, 1953). There are other factors that influence WF that are currently being researched. For example, some studies are looking into how the surface roughness of the material can influence the WF. Malayter and Garner examined how surface waviness, particularly period and amplitude, influences the work function (2020). This may have important implications as material erodes and during repetitive breakdown events (Brayfield *et al.*, 2019). The WF is one of the many areas of research that could be continued further.

Space Charge Limited Emission (SCLE)

Some of the earliest theories developed to model electron emission were analyzed in vacuum conditions. In 1911, Child derived a theory for the condition when a sufficient buildup of ions in the gap prevents further emission additional ions in a planar geometry (1911); this threshold is referred to as the space-charge limited current (SCLC). Child's model was originally created for ions; Langmuir re-derived Child's model to account for other sources besides ions (Langmuir, 1913), leading to what is called today either Child's law or the Child-Langmuir (CL) law to predict SCLE in vacuum conditions for planar diodes. The CL law assumes that there are no ions between the electrodes, the initial velocity of the electrons is negligible, and vacuum to give (Langmuir, 1913)

$$J_{CL}(V) = \frac{4\varepsilon_0}{9d^2}\sqrt{\frac{2e}{m}}V^{\frac{3}{2}}, \tag{1.14}$$

where d is the gap distance, e is the elementary charge ($1.602 \times 10^{-19}\ C$) , V is the potential difference (voltage), m is the mass of the electron ($9.109 \times 10^{-31}\ kg$), and ε_0 is the permittivity of free space ($8.854 \times 10^{-12}\ F \cdot m^{-1}$). Langmuir and Blodgett extended the CL law to derive SCLC for coaxial cylinders (1923) and concentric spheres (1924) in vacuum. These provided correction factors to the classical CL equation.

Further studies were completed in the 1990s and 2000s to add corrections as the geometry changes (Lau *et al.*, 1991, Ang *et al.*, 2003, Ang *et al.*, 2004; Ang *et al.*, 2006). These corrections

were developed to model quantum affects, and they are needed when the gap distance, d, is smaller or similar to λ_0, the de Broglie wavelength (Ang *et al.,* 2003; Ang *et al.,* 2004; Ang *et al.,* 2006; Bhattacharjee *et al.*, 2008; Lau *et al.,* 1991). When quantum effects occur,

$$J_{QSCL}(V) = \frac{\varepsilon_0 \hbar^2 V^{1/2}}{e^{1/2} m_e^{3/2} d^4} \tag{1.15}$$

is used to model the current density from SCLE. In this equation, $\hbar$ is Planck's constant, m_e is the mass of the electron, d is the gap distance, e is the elementary charge of the electron, and ε_0 is the relative permittivity of free space (Ang *et al.,* 2004). Although quantum research is ongoing, this thesis is not heavily connected to these effects. The main equation for SCLE in vacuum used for this research is the classical CL.

While CL accounts for SCLE in vacuum, the Mott-Gurney (MG) law was developed for semiconductors. However, MG was later applied to model liquids and gases with collisions (Mott and Gurney, 1940). The MG law is relatively accurate for modeling the current density due to SCLE with collisions when the single-carrier device is ideal; ideal means that the contacts are Ohmic, there are no traps, and there is no doping (Röhr *et al.*, 2018). There are a few situations in which the law does not accurately model the current density (Röhr *et al.*, 2018), such as when the device is "non-ideal." The MG law is

$$J_{MG}(V) = \frac{9}{8} \mu \varepsilon_0 \varepsilon_r \frac{V^2}{d^3}, \tag{1.16}$$

where ε_r is the relative permittivity of the gas, d is the gap distance, μ is the mobility of the electron specific to the gas (Röhr *et al.*, 2018). Also, μ describes how electrons or charged particles move through the substance. The mobility is often considered constant when addressing SCLE with collisions; however, μ depends on multiple variables such as temperature, electric field, pressure, or structure which will be discussed later.

Photoemission (PE)

PE occurs when light strikes the material surface and causes a release of electrons. Many of the theories explaining PE begin with Einstein's explanation of PE (Jensen, 2017). PE is often analyzed using the quantum efficiency (QE), which is the ratio of excited electrons to incident photons (Jensen, 2017). The number of excited electrons is defined as $\Delta Q/q$ with ΔQ the charge collected and q the elementary charge (Jensen, 2017). This makes the number of incident photons

$\Delta E/\hbar\omega$, where ΔE is the energy deposited and $\hbar\omega$ is the photon energy (Jensen, 2017). From these relationships, QE is

$$QE = \left(\frac{\hbar\omega}{q}\right)\frac{\Delta Q}{\Delta E}. \qquad (1.17)$$

Using Einstein's explanation,

$$QE \propto (\hbar\omega - \Phi)^2, \qquad (1.18)$$

where Φ is the original work function.

In the 1930s, Fowler (Fowler, 1931; Jensen, 2017) and DuBridge (DuBridge, 1932; DuBridge and Roehr, 1932; DuBridge, 1933) continued to work on PE. Fowler continued with the assumption that the electrons obey Fermi-Dirac statistics (DuBridge, 1932; Fowler, 1931; Jensen, 2017), which defines the probability of an electron state with energy E being occupied as (Modinos, 1984)

$$f(E) = 1/[1 + \exp[(E - \mu_F)/k_bT]], \qquad (1.19)$$

where k_b is Boltzmann's constant, T is the absolute temperature, and μ_F is the Fermi energy level (Modinos, 1984). Fowler also theorized that altering the transmission probability term $D(E_x)$ to $D(E_x + \hbar\omega)$ could account for the assumption that one electron absorbed all of the incident photon's energy (Fowler, 1931; Jensen, 2017). Defining the transmission probability as

$$D(E_x) \approx \Theta[E_x + \hbar\omega - (\mu_F + \varphi)] \qquad (1.20)$$

$$D(E) = 1/\left[1 + \exp\left(\theta(E_x)\right)\right], \qquad (1.20)$$

the supply function by

$$f(E_x) = \frac{m}{\pi\beta\hbar^2}\ln\{1 + \exp[\beta(\mu_F - E_x)]\}, \qquad (1.21)$$

and the Gamow function by

$$\theta(E) = 2\frac{\sqrt{2m}}{\hbar}\int_{x-}^{x+}\sqrt{V(x) - E_x}\,dx \qquad (1.22)$$

where $V(x)$ is the image barrier function, yields the general current density as (Jensen, 2007; Jensen, 2017; Jensen, 2018)

$$J(F,T) = \frac{q}{2\pi\hbar}\int_0^\infty D(E_x)f(E_x)\,dE. \qquad (1.23)$$

To account for the Schottky barrier, $\varphi = \Phi - \sqrt{4QF}$ replaces the WF; $Q \approx 0.36\ eVnm$, and F is an electric field with units of $eV \cdot nm^{-1}$ (Jensen $et\ al.$, 2007; Jensen, 2018). From these relationships,

$$\frac{\Delta Q}{\Delta E} \approx \frac{J(\hbar\omega)\Delta t}{I_\lambda \Delta t} = \frac{J(\hbar\omega)}{I_\lambda} \tag{1.24}$$

where $J(\hbar\omega)$ is the current calculated using equation 1.23 with the photon energy and I_λ is the laser intensity (DuBridge, 1932; DuBridge, 1933; Fowler, 1931; Jensen, 2017; Modinos, 1984). From this, QE could be defined as

$$QE \equiv \left(\frac{\hbar\omega}{q}\right)\frac{J_{FD}(\hbar\omega)}{I_\lambda} \propto (\hbar\omega - \Phi)^2, \tag{1.25}$$

which is the Fowler-DuBridge (FD) equation (DuBridge, 1932; DuBridge, 1933; DuBridge and Roehr, 1932; Fowler, 1931; Jensen, 2017; Jensen, 2018). The current density due to the photon energy is given by

$$P_{FD}(\hbar\omega) = \frac{U\big(\beta(\hbar\omega - \varphi)\big)}{U(\beta\mu_F)} \tag{1.26}$$

to account for the electron emission probability (Jensen, 2007; Jensen, 2017), where $U(x)$ is the Fowler-DuBridge (FD) function, a universal function, which is defined as

$$U(x) = \int_{-\infty}^{x} \ln\big(1 + e^{\beta(\mu_F - E)}\big)dE, \tag{1.27}$$

where μ_F is the Fermi energy level in eV, E is the energy, and β is the temperature energy slope factor (Jensen, 2007; Jensen, 2017; Jensen, 2018). The FD function can be approximated to

$$U(x) \approx \frac{\pi^2}{6} + \frac{x^2}{2} - e^{-x} \tag{1.28}$$

as long as $x > 0$ (Jensen *et al.*, 2007; Jensen *et al.*, 2008). Now using this FD function and QE, the FD equation is given by

$$J_{FD}(\hbar\omega) = \left(\frac{q}{\hbar\omega}\right)[1 - R(\theta)]F_\lambda(\hbar\omega, T)I_\lambda P_{FD}(\hbar\omega), \tag{1.29}$$

where F_λ is the scattering factor, $R(\theta)$ is the reflectivity with incident angle θ, and $P_{FD}(\hbar\omega)$ is the emission probability (Jensen, 2007; Jensen *et al.*, 2007; Jensen *et al.*, 2008; Jensen, 2017). The QE for the FD equation may also be defined as (Jensen *et al.*, 2008)

$$QE_{FD}(\hbar\omega) = [1 - R(\theta)]F_\lambda(\hbar\omega, T)P_{FD}(\hbar\omega). \tag{1.30}$$

The FD equation was later modified with a series of coefficients to account for quantum affects (Jensen *et al.*, 2007; Jensen *et al.*, 2008; Jensen, 2017). The current density due to the photon energy is

$$J_{MFD}(\hbar\omega) = \left(\frac{q}{\hbar\omega}\right)[1 - R(\theta)]F_\lambda(\hbar\omega, T)I_\lambda P_{MFD}(\hbar\omega) \tag{1.31}$$

where $P_{MFD}(\hbar\omega)$ is the modified emission probability (Jensen *et al.*, 2008). The updated modified Fowler-DuBridge (MFD) (Jensen *et al.*, 2008) estimates the emission probability to be

$$P_{MFD}(\hbar\omega) = \frac{(\hbar\omega - \varphi)^2 + 2\beta_T^{-2}\zeta(2)(1 + n^2)}{2\hbar\omega(2\mu_F - \hbar\omega)}, \tag{1.32}$$

where $\zeta(2) = \pi^2/6$ is the Riemann zeta function (Jensen *et al.*, 2007), $\beta_T = 1/k_bT$, and $n = n(F,T) = \beta_T/\beta_F$ is the ratio of the energy slope factors (Jensen, 2007; Jensen *et al.*, 2007). Using $P_{MFD}(\hbar\omega)$, $QE_{MFD}(\hbar\omega)$ is given by (Jensen *et al.*, 2008)

$$QE_{MFD}(\hbar\omega) = [1 - R(\theta)]F_\lambda(\hbar\omega, T)P_{MFD}(\hbar\omega). \tag{1.33}$$

Many of these modifications to the MFD have occurred since the 1990s. Jensen provides a general summary of the changes to the FD since it was first developed (Jensen, 2007); these changes were made to account for the errors surrounding the threshold energy. The equations regarding PE are often connected with one of the other electron emission mechanisms.

Unification of Emission Mechanisms

Unifying the different electron emission mechanisms has been an area of interest in since the first derivation of the emission mechanisms. Unification of these theories provides information regarding the conditions and factors that could cause the transition between the different mechanisms. Understanding the transitions is beneficial for developing electronics that require certain operating conditions. Studies regarding the transitions between the mechanisms began soon after they were first derived. Initially, these studies usually focused on unifying two emission mechanisms; many of the studies focused on unifying FE and SCLE or FE and TE. However, more recently, these studies have connected additional mechanisms to add a third or fourth electron emission mechanism to the unification (Garner *et al.,* accepted).

Since the derivation of FE and SCLE, there have been numerous studies connecting these two emission mechanisms (Bhattacharjee and Chowdhury, 2009; Chen *et al.*, 2009; Feng and Verboncoeur, 2006; Forbes, 2008; Lau *et al.*, 1994; Rokhlenko *et al.*, 2010). In 1994, Lau published a paper that connected FN and CL (Lau *et al.*, 1994); this paper became the starting point for the most recent unification work on which this thesis is based. Lau used Poisson's equation and current density to derive asymptotic solutions for CL and FN for specific initial conditions. He then used these limits to find a transition point between these two mechanisms. In 2006, Feng and Verboncoeur analyzed the transition between FN and CL (Feng and Verboncoeur,

2006); this research looked at the effect that the work function had on the transition between these two equations. A higher WF caused a slower transition to the SCL; in addition to looking at the effect that the WF had on the transition, they analyzed the transitions due to the limitations of the geometry (Feng and Verboncoeur, 2006). In 2008, Forbes reviewed the reduction of the electric field across parallel plates due to space-charge (Forbes, 2008). In 2009, Bhattacharjee and Chowdhury experimentally analyzed the transitions between FN and SCL for gap distances in the nanometer range (Bhattacharjee and Chowdhury, 2009). In this study, they looked at how the FE transitioned to the quantum SCL and the classical SCL; the quantum level is not within the purview of this thesis. In the same year, Chen analyzed how field emission nanodevices were affected by space charge (Chen *et al.*, 2009). These few papers solely focused on FE and SCLE in vacuum conditions, and SCLE with collisions was not included until recently.

In 2018, Darr extended the research started by Lau *et al.* in 1994 to connect FN, CL, and MG to derive an exact solution and asymptotic limits in terms of applied voltage, gap distance, and electron mobility (Darr *et al.*, 2019). Darr *et al.* followed the same processes as Lau *et al.*, but modified the electron force balance equation to account for the collisions of the emitted electron with a neutral gas atom by adding a friction term. They then subsequently connected the asymptotic solutions for all three equations at a single nexus point where the resulting three asymptotic solutions for FN, CL, and MG matched. This research explored the effects that mobility μ and gap distance d had on the three regions/transitions (Darr *et al.*, 2019). Because typical emitter experiments use a series resistor as a current limiter, Dynako *et al.* subsequently incorporated Ohm's law (OL) into the unification model of FN, CL, and MG (2019).

The unification of FE and TE was another branch of research that was heavily studied (Benilov and Benilova, 2013; Crowell, 1969; He *et al.*, 2008; Jensen and Cahay, 2006; Jensen *et al.*, 2019; Murphy and Good, 1956; Padovani and Stratton, 1966; Segev *et al.*, 2013; Xu *et al.*, 2000), and this often included connecting PE to either FE or TE (DuBridge and Roehr, 1932; Jensen *et al.*, 2002; Jensen *et al.*, 2019). In 1956, Murphy and Good analyzed the transition region between TE and FE (Murphy and Good, 1956); this analysis focused on the modified Richardson-Schottky (RS) equation for TE and the FN equation for FE. They determined the regions in which the FN equation could be used to model FE for low temperatures and high fields and the RS could be used to model TE for high temperatures and low fields; these equations were dependent on the electric field, temperature, and work function (Murphy and Good, 1956). Following the work of

Murphy and Good, Padovani and Stratton completed an experiment in 1966 to unify FE and TE emission (Padovani and Stratton, 1966). In the 2000s, much of the work regarding the unification of FE and TE included the use of the general-thermal field (GTF) equation which included the effects from PE (Jensen *et al.*, 2002; Jensen and Cahay, 2006; Jensen, 2007; Jensen, 2018; Jensen *et al.*, 2019). The GTF depends on both the thermal dominated current density and the electric field dominated current density and has a general form of

$$J_{GTF}(F,T) = A_{RLD}T^2 N(n,s),\qquad(1.34)$$

where A_{RLD} is the RLD constant which is equal to $(emk_B^2)/(2\pi^2\hbar^3)$ (Jensen, 2018). In equation 1.34, $N(n,s)$ is

$$N(n,s) = n\int_{-\infty}^{\infty}\frac{\ln\left[1+e^{n(x-s)}\right]}{1+e^x}dx\qquad(1.35)$$

where $n(F,T) \equiv \beta_T/\beta_F$ and $s(F,T) \equiv \beta_F(E_0 - \mu_F)$ (Jensen, 2018). Equation 1.34 can be adapted to include the PE regime as s becomes negative and μ_F goes to $\mu_F + \hbar\omega$ (Jensen, 2018). Jensen simplified this equation using conditions to define the regions where certain emission mechanisms dominate based on the values of s, β_F, β_T, and T (Jensen, 2018). Equation 1.34 can then be related to the canonical equations for FE, TE, and PE (Jensen, 2018).

The most recent study connects TE, FE, and SCLE with and without collisions (Darr *et al.*, 2020), which connected various theories for electron emission (FN, RLD, GTF, MG, and CL) with OL (Darr *et al.*, 2020). In addition to deriving a model that connected FE (FN), TE (RLD), SCLE (GCL) (CL), Darr *et al.* constructed phase plots as functions of gap distance to show the regions where OL, CL, MG, FN, and RLD are the most prominent (Darr *et al.*, 2020). PE is one of the main emission mechanisms that is not included in this model.

Breakdown

Electronic breakdown in gases is a highly researched area; it happens when charge carrier multiplication occurs due to the strength of the electric field or an applied voltage across the gap (Fu *et al.*, 2020). Much of the research began with the development of Paschen's law (PL) in 1889 (Paschen, 1889). Paschen derived breakdown voltage V_b as a function of pressure, gap distance, and the secondary emission coefficient (Paschen, 1889; Garner *et al.*, 2020a). PL is given by

$$V_b = \frac{B_p pd}{\left\{ln\left(A_p pd\right) - ln\left[ln(1 + \gamma_{SE}^{-1})\right]\right\}}\qquad(1.36)$$

where p is the pressure, d is the gap distance, A_p and B_p are empirical constants that depend on the gas, and γ_{se} is the secondary emission coefficient. PL is characterized by a minimum V_b that occurs at (Garner *et al.*, 2020a)

$$V_{b,min} = \frac{B_p \exp(1) \ln(1 + \gamma_{se}^{-1})}{A_p}. \tag{1.37}$$

when $pd = \exp(1) \ln(1 + \gamma_{se}^{-1})/A_p$.

Around 1900, Townsend developed the Townsend theory (Townsend, 1901); this theory discussed the avalanche process. Townsend discharge is an ionization process in which the electric field accelerates free electrons causing an avalanche. Townsend avalanche (TA) criteria,

$$\gamma_{se}(e^{\alpha d} - 1) = 1, \tag{1.38}$$

is based on the ionization coefficient α, the secondary emission parameter γ_{se} and the gap distance d (Garner *et al.*, 2020a; Loveless and Garner, 2017b; Townsend, 1901; Venkattraman and Alexeenko, 2012). In 1915, Townsend published a book that discussed α,

$$\alpha = A_p p \exp\left(-\frac{B_p p}{E}\right), \tag{1.39}$$

the ionization coefficient (Townsend, 1915) . The ionization coefficient depends on the pressure p and the electric field E; it is also influenced by the gas properties. Using the breakdown criteria and the ionization coefficients, Townsend defined the total discharge current at the anode due to the avalanche process and secondary emission process as (Fu *et al.*, 2020)

$$J = \frac{J_0 \exp(\alpha d)}{1 - \gamma_{se}[\exp(\alpha d) - 1]}. \tag{1.40}$$

Paschen's law and TA are the two fundamental theories for breakdown in gases; these are the two theories needed for the background of this thesis. However, on a microscale level there are other mechanisms that can influence these factors.

Breakdown and Emission connection

At microscale gaps, the TA no longer drives gas breakdown (Boyle and Kisliuk, 1955) and there are numerous studies that model the effect that FE has on breakdown (Go and Pohlman, 2010; Go and Venkattraman, 2014; Kunhardt, 1980; Loveless and Garner, 2017b; Venkattraman and Alexeenko, 2012). Research has also been done on how space charge affects the breakdown (Go and Pohlman, 2010). Although the FE is thought to be an initial phase of breakdown at microscale,

TE is also thought to cause breakdown in gases (Haase and Go, 2016; Lee *et al.*, 2017a; Lee *et al.*, 2017b; Venkattraman, 2014). Because electronic breakdown can be used for numerous applications, it is important to understand how these fundamental emission mechanisms affect breakdown.

Due to the potential effect of FE, PL is modified to model the breakdown for all gap sizes. In 2010, Go and Pohlman reviewed a mathematical model that could be used to modify this law (Go and Pohlman, 2010). To account for the FE, the ion enhancement coefficient, γ'

$$\gamma' = Ke^{-D_{FN}d/V}, \tag{1.41}$$

is added to the breakdown criteria; this represents the incident ion that enhances electron emission (Go and Pohlman, 2010). In equation 1.41, K is a fitting parameter that includes C_{FN} and D_{FN}; these are the same constants described in equations 1.7 and 1.8. The Townsend avalanche criteria could then be described using the secondary emission coefficient and the ion enhancement (Venkattraman and Alexeenko, 2012); this is given by

$$(\gamma_{se} + \gamma')(e^{\alpha d} - 1) = 1. \tag{1.42}$$

From this research, they verified that the ionization coefficient, α, was different for the microscale and the macroscale regions. To account for the space charge affects as well, the electric field is adapted to include the effects from the positive space charge at the cathode, E^+. The modified FN equation would include this electric field (Venkattraman and Alexeenko, 2012) as given below

$$j'_{FN} = C_{FN}(E + E^+)^2 \exp\left(-\frac{D_{FN}}{E + E^+}\right). \tag{1.43}$$

Their equation resulted in finding the current density in terms of the modified electric field and the ion enhancement coefficient (Venkattraman and Alexeenko, 2012)

$$j_{tot} = \frac{j_{FN}\exp(\alpha d)}{1 - (\gamma_{se} + \gamma')(\exp(\alpha d) - 1)}. \tag{1.44}$$

The only undefined variable in these equations was E^+. They determined the value of E^+ based on Poisson's equation and the charge density; the value E^+,

$$E^+ = \frac{\rho d}{2\varepsilon_0}, \tag{1.45}$$

was assumed to be constant due to a constant charge density from the center of the geometry to the outside from particle-in-cell simulations (Venkattraman and Alexeenko, 2012). In reality, space-charge density cannot be constant across the gap because this electric field is not spatially constant in a practical device since they are typically non-planar. Typical experiments use pin-to-

plate (Brayfield *et al.*, 2019) or pin-to-pin (Meng *et al.* 2019) geometries. Using this simple planar diode assumption yields a new breakdown criterion for avalanches as (Venkattraman and Alexeenko, 2012; Garner et al. 2020a)

$$F_{br} = \frac{2v_d \varepsilon_0 E^2 [1 - \gamma_{se}(\exp(\alpha d) - 1)]}{D_{FN} dj_{FN}(\exp(\alpha d) - 1)}. \tag{1.46}$$

Equation 1.46 cannot be solved analytically for the breakdown electric field E because α depends on E, making the equation transcendental. In 2016, Loveless and Garner used a matched asymptotic analysis to derive scaling laws to look at breakdown from nanogaps to microscale (Loveless and Garner, 2016). They first nondimensionalized equation 1.46 to eliminate unnecessary parameters to obtain

$$F_{br} = \sqrt{\frac{\bar{T}\bar{E}}{\bar{p}\bar{d}^2}} \frac{\exp(1/\bar{E})\left[1 - \gamma_{se}\left(\exp(\bar{\alpha}\bar{d}) - 1\right)\right]}{\exp(\bar{\alpha}\bar{d}) - 1}. \tag{1.47}$$

This equation is universal since all dependence on gas and electrode materials has been eliminated. In 2017, Loveless and Garner proceeded to develop a universal theory for gas breakdown; this theory connected the microscale to PL (Loveless and Garner, 2017b). Based on the scaling constants and empirical constants from previous experiments, they developed the model to represent the transition from FE to breakdown (Loveless and Garner, 2017b). This model yielded the dimensionless applied voltage as a function of dimensionless pressure from small gaps where FE dominates to the classical PL. Figure 1.2 demonstrates the various connections between the emission and breakdown mechanisms. Research has connected SCLE, FE, TE, and breakdown depending on certain conditions and parameters such as gap distance and pressure.
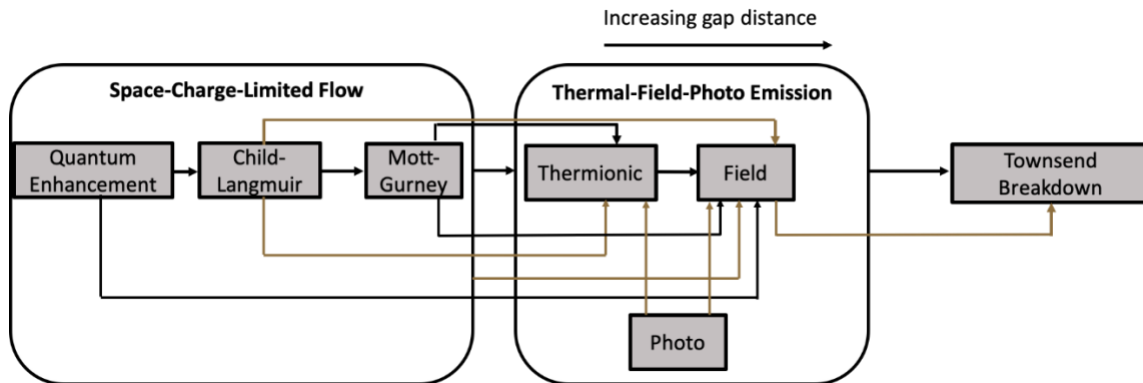
Figure 1.2. This figure shows the possible transitions between the different theories of emission and breakdown (Garner *et al.*, 2020b)

The mechanisms that follow TB are only briefly discussed because the main focus of the thesis is on emission. After Townsend discharge, if the current continues to increase due to a constant resistance, the discharge will transition to glow and then arc discharge (Kunhardt, 1980). At high pressures and large gap distances, the electron avalanche causes a high space charge field; this space charge field leads to streamer formation (Loveless and Garner, 2017b). The streamer theory was developed independently by Meek, Raether, and Loeb, but their theories had the same basic foundation; the photoionization of the gas is the most important variable for breakdown determination after a specific point in the avalanche development occurs (Kunhardt, 1980). Once this particular point is reached, streamers begin to form. Streamers are highly conducting plasma filaments; they grow due to ionization in strong electric fields (D'yakonov and Kachorovskii, 1988). These are only a few of the breakdown mechanisms, but they are the most relevant for the current research and understanding the motivation for this research.

1.2.2 Breakdown and emission in liquids

Electronic processes are just as useful in liquids as they are in gases. Research regarding electronic processes in liquids began around the same time of that in gases; this includes electron emission and breakdown research. Much of the breakdown and electron emission research for liquids were interconnected; this means that the transitions between a few of these mechanisms were being researched. Electron emission is believed to be one of the phases of breakdown in liquids (Auger *et al*., 2016; Phan *et al*., 2020; Qian *et al*., 2005). Unlike the research for gases, the research regarding liquids often included more than one mechanism in a study. In addition, many of the research studies conducted for electronic processes in liquids were experimental.

Research regarding electronic processes in liquids typically utilizes dielectric liquids or water solutions for experimental studies. Dielectric liquids can be both non-polar and polar; generally, they have smaller relative permittivity and higher DC resistivities (Forster, 1990). The small amount of mobile charge carriers is the main connection between dielectric liquids; these mobile charge carriers are often labeled as free (Forster, 1990). For example, some of the non-polar dielectric liquids are hydrocarbons such as hexane, and alcohols are examples of polar dielectric liquids (Forster, 1990). Water is often used for research regarding electronic processes, and salt solutions are utilized as well (Jones and Kunhardt, 1995b). Gases and liquids have different properties that prevent certain theories developed for gases from being used for liquids

such as the streamer theory and CL (Jones and Kunhardt, 1995b). Other theories can be used for liquids, such as FN and MG, but the constants will change due to the physical properties of the liquids.

Emission

One of the first electron emission mechanisms analyzed in liquids was TE. In 1936, Baker and Boltz reviewed the process of TE in liquids which included observing the conditions of the RLD equation that might change as a result of using a dielectric liquid (Baker and Boltz, 1937). These conditions include: a lower WF, a lower operating temperature, current saturation will be less complete at high fields, and collision and attachment of electrons and molecules interfering with the model (Baker and Boltz, 1937). The WF is lower because a vacuum scenario requires more energy for an electron to be released, and the lower operating temperature is so the liquid stays in the liquid phase (Baker and Boltz, 1937). The SE also had to be modified for liquids; the image correction is less influential because of the liquid. In 1940, LePage and DuBridge built upon the Baker and Boltz experiment to look into electron emission in dielectric liquids (LePage and DuBridge, 1940). LePage and DuBridge determined the emitting area was largely affecting the results; the emitting area was determined to be smaller than the geometric area (LePage and DuBridge, 1940). They believed that the equation was not modeling pure TE, but a combination of TE and FE. The work was believed to show a transition between SE and FE; this is a transition between temperature dependent mechanisms and temperature independent mechanisms (Bragg *et al.*, 1954).

Field emission (FE) and SCLE were often observed together in some research and experimental studies. In 1953, Bragg *et al.,* looked at emission and breakdown in dielectric liquids; they analyzed how the cathode affected the different emissions and space charge (Bragg *et al.*, 1954). First, they analyzed FE; the general FN equation could be used as along as the empirical constants accounted for the dielectric prosperities of the liquid. Simple space charge equations similar to those developed by Child and Langmuir could be used for a basic model (Bragg *et al.*, 1954). The dependence of the space charge on mobility was briefly discussed; the mobility has an influence both gases and liquid space charge.

In 1969, Halpern and Gomer completed an experiment that looked at FE and ionization in rare liquid gases liquids: H_2, D_2, O_2, He, N_2, Benzene, and Ar (Halpern and Gomer, 1965; Halpern

and Gomer, 1969a; Halpern and Gomer, 1969b). For this experiment, the assumptions were about the experimental geometry and mobility, μ. This experiment assumed that concentric sphere electrodes could be defined geometrically with $R \gg r_t$, where R is the outer radius of the anode, and r_t is the emitter radius (Halpern and Gomer, 1969a). They set $r_t \approx 10^{-5}$ cm and the solid angle for emission as $\alpha\pi$ with $\alpha = 0.6$ (Halpern and Gomer, 1969a). They also assumed each liquid had a constant μ, which is common for liquid emission studies. The emitters were assumed to be clean tungsten (W), meaning that they neglected any changes to the electrode surface. For the data analysis, they used

$$\ln\frac{I}{V^2} = \ln A - \left[6.8 \times 10^7 \frac{\Phi^{\frac{3}{2}}g(y^2)}{kV}\right],$$
(1.48)

which is a modified FN equation with image correction factor $g(y^2)$ and proportionality constant k. From the experiment, Halpern and Gomer determined that FE (FN) could be observed at lower currents and SCL could be observed at higher currents for the H_2 and D_2 data (Halpern and Gomer, 1969a). For He and Ar, the data demonstrated the transition to SCL emission led to avalanching and bubble formation at the tip of the geometry. Following Halpern and Gomer's experiment, McClintock conducted an experiment looking at FE in liquid helium (McClintock, 1969); he observed the same bubbling at the tip as Halpern and Gomer.

In 1978, Dotoku *et al.* completed an experiment analyzing FE in nonpolar liquids using a pin to plate geometry with a tungsten (W) emitter, but for their calculations, they assumed concentric spherical condenser geometry even though the experimental geometry was pin to plate (Dotoku *et al.*, 1978). This is the main experiment used for the research conducted in this thesis. This experiment sought to determine whether FE and SCLE regimes could be observed by recording the current I resulting from an applied voltage V. They modeled the current by

$$I = \frac{6.2 \times 10^{-6}\mu_F^{\frac{1}{2}}SF^2}{\varphi^{\frac{1}{2}}(\mu_F + \varphi)}\exp\left(-\frac{6.8 \times 10^7\varphi^{\frac{3}{2}}}{F}\right),$$
(1.49)

with constants that included the Fermi energy level μ_F, the emission area S, the work function φ and the electric field strength F, defined as the ratio of the applied voltage to the emitter radius. This experiment allowed them to observe the FE regime and the beginning of SCL.

Figure 1.3 is the digitized data from figure 2 of the paper, and figure 1.4 is the digitized data from figure 5 of the paper (Dotoku *et al.*, 1978). Figure 1.4 only includes the data points from figure 5 and the dashed lines; the dashed lines are the linear best fits for the FN equation.
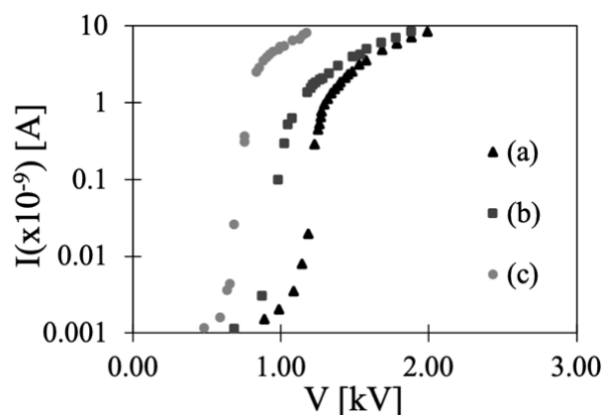
Figure 1.3. In this figure, (a) is n-hexane (triangles), (b) is TMP (squares), and (c) is TMS (circles). Reproduced from Dotoku, K., Yamada, H., and Sakamoto, S., "Field emission into nonpolar organic liquids," J. Chem. Phys. **69** (3), 1121-1125 (1978), with the permission of AIP Publishing.
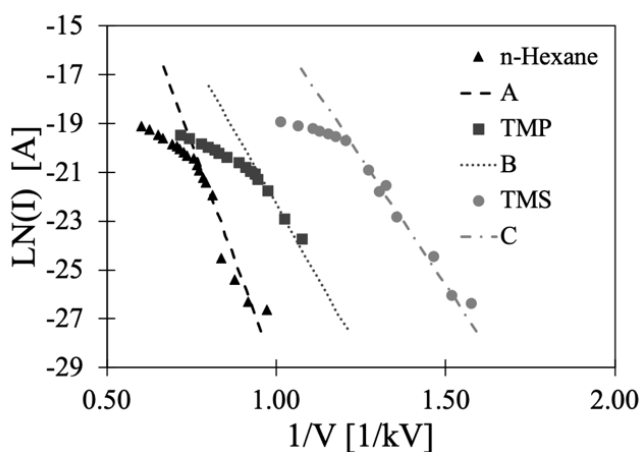
Figure 1.4. In this figure, the triangles are n-Hexane, the squares are TMP, and the circles are TMS. The dashed line (A) is the FN best fit for n-Hexane. The dotted line (B) is the FN best fit for TMP. The dashed-dotted line (C) is the FN best fit for TMS. Reproduced from Dotoku, K., Yamada, H., and Sakamoto, S., "Field emission into nonpolar organic liquids," J. Chem. Phys. **69** (3), 1121-1125 (1978), with the permission of AIP Publishing.

Electron emission in liquids has been studied through theoretical and experimental work; the majority of this research involves looking at no more than two electron emission mechanisms. Due to this lack of unification, there is no universal model, similar to that of gases, that connects

the different electron emission mechanisms in liquids. A universal model describing these mechanisms provides information on transitions between the different regimes, which may potentially aid numerous industries and applications.

Breakdown

Unlike research regarding electron emission in liquids, electric breakdown research is more current. In 1990, Forster went through the different electric properties of dielectric liquids. In 1994, Lewis looked at the basic electric processes in dielectric liquids. His review on the processes mainly focused on charge transport (Lewis, 1994).

In 1994, Tobazcon reviewed a few of the pre-breakdown events in dielectric liquids (Tobazcon, 1994). Breakdown can be divided into pre-breakdown and breakdown with electronic, ionic, optical, thermal, mechanical, and hydrodynamic phenomena involved (Tobazcon, 1994). Hydrodynamic phenomena refer to flow and cavitation, thermal to boiling or change of phases, optical to light emission processes, and mechanical to shockwaves (Tobazcon, 1994). For the thermal processes, the three most important temperatures are the melting, boiling, and critical (corresponding to phase change) temperatures (Tobazcon, 1994). Two additional phenomena of interest are bubbling and cavitation, which both depend on pressure and temperature. When the temperature increases with constant pressure, bubbles of vapor or gas form; this is sometimes referred to as boiling (Tobazcon, 1994). When the pressure is reduced at a constant temperature, cavities composed of vapor or gas form; this is cavitation (Tobazcon, 1994). Streamers and the transition to arc discharge are also addressed as breakdown mechanisms. An arc is "a highly conducting and luminous channel capable of carrying huge currents between electrically stressed conductors," (p. 1132, Tobazcon, 1994). All of the processes that occur in pre-breakdown are irreversible, and breakdown is the final irreversible process (Tobazcon, 1994).

Shortly after Tobazéon's work, Jones and Kunhardart published three papers pertaining to the pulsed dielectric breakdown (Jones and Kunhardt, 1995a; Jones and Kunhardt, 1995b; Jones and Kunhardt, 1995c). One of these papers provided a model for the breakdown in liquids in which it analyzed the breakdown and the initiation process (Jones and Kunhardt, 1995a). The other two papers provided experimental results for the pulsed dielectric breakdown (Jones and Kunhardt, 1995b; Jones and Kunhardt, 1995c). In 2006, Denat continued to look into pre-breakdown phenomena in dielectric liquids at high fields; this research explored the different high-field

conduction mechanisms and the avalanche process and breakdown along with streamers (Denat, 2006). Following Denat, Lesaint published a paper in 2016 regarding the propagation modes for pre-breakdown phenomena. After pre-breakdown, breakdown occurs and, unlike gases, there is no model similar to PL for liquids that predicts the breakdown voltage (Lesaint, 2016). Only a few of the research studies regarding breakdown in liquids are addressed to provide background information for the thesis.

1.3   Mobility

Mobility describes the ability of a charged particle to move through a substance; this substance can be any phase such as gases, liquids, or solids. Mobility, μ, is often measured in units of $cm^2 \cdot V^{-1}s^{-1}$, and it depends on many variables, such as material properties, temperature, the electric field strength, and the pressure (Allen, 1976; Bragg *et al.*, 1954; Borghesani and O'Malley, 2003; Denat, 2006; Hirashima *et al.*, 1981; Jacobsen *et al.*, 1986; Jacobsen *et al.*, 1989; Jones and Kunhardt, 1995a; Jones and Kunhardt, 1995c; Kirkpatrick and Dorfman, 1983; Lesaint, 2016; Lewis, 1994; Muñoz *et al.*, 1987; Röhr *et al.*, 2018; Schmidt, 1977; Schmidt, 1984; Tobazcon, 1994). This section includes information about each of the variables that influence the mobility the most. The first part of the section will address the material properties which include information about the electron states, the structure, and the density. The other three sections will review the temperature, electric field, and pressure.

1.3.1   Material Properties

Material Electron States

The phase of the material being analyzed is one of the most influential factors in regard to the mobility of the substance. The phase determines the available electron states; these electron states are different depending on whether the substance is a gas, liquid, or solid. Each phase has its own electron states, but the electron states for liquids and solids are very similar. This section reviews the different electron states for liquids.

Electrons in liquids are either in delocalized or localized states (Allen, 1976; Lewis, 1994; Schmidt, 1984). The delocalized state describes quasi-free electrons, which are conduction electrons in a metal or semiconductor or electrons moving through a gas (Allen, 1976). For

delocalized states the mobility is usually large ($\mu \gg 1\ cm^2V^{-1}s^{-1}$) (Schmidt, 1984). Increasing the temperature typically decreases the mobility of a quasi-free electron (Allen, 1976). Collisions due to thermal motion limit the motion of these quasi-free electrons (Allen, 1976; Lewis, 1994). When analyzing a quasi-free electron, its energy level in a liquid V_0 (eV) is important for trends and calculations (Allen, 1976); this is also the energy of a conduction band (Jacobsen *et al*., 1986). When the density increases, V_0 increases. Repulsion occurs due to the exchange forces, and polarization induces dipoles. "The greater the attraction compared to the repulsion, the more negative is V_0," (p.3, Allen, 1976). The electron is quasi-free, and the delocalized electron interacts poorly with the liquid, the value of V_0 is highly negative (Tobazcon, 1994). The energy level of a quasi-free electron is important for the delocalized electron states.

The second state is the localized state. Electrons become localized due to the molecular polarizability and permanent dipoles in the liquid. When the electrons are localized in liquids, they are considered solvated electrons (Allen, 1976); localized electrons in solids are considered trapped (Allen, 1976). Solvated electrons have mobilities much smaller than quasi-free electrons (Allen, 1976). For the localized states the mobility is usually small ($\mu \ll 1\ cm^2V^{-1}s^{-1}$); the mobility drops because the electrons are localized (Kirkpatrick and Dorfman, 1983).The mobility of a solvated electron typically increases with increasing temperature (Hirashima *et al*., 1981).

As mentioned in this section, the localized and delocalized states are affected by the liquid's temperature, the density, and energy level. The energy level depends on the liquid properties. The movement of electrons between these two different states depends on variables such as temperature and electric field. All of the same factors that affect the electron states in solids and gases affect the electron states in liquids.

Material Structure

The structure/shape of the molecule also influences mobility. Research has shown that the mobility changes as the shape of the molecule becomes more sphere like; in particular, the mobility will increase (Schmidt, 1977). The structure of TMS is almost sphere like which explains why the mobility is higher than the mobility for the other liquids mentioned. For alkanes, when the chain length increases at room temperature, the mobility decreases (Hirashima *et al*., 1981). Any branching of carbon atoms increases mobility (Schmidt, 1977; Schmidt, 1984). Also, research has

indicated that the type of bonds may affect the mobility. For example, double and triple bonds reduce mobility (p.634, Lewis, 1994).

Material Density

In addition to temperature and pressure, the density of the gas, liquid, or solid can also affect the mobility (Borghesani and O'Malley, 2003; Jacobsen *et al.*, 1986; Jacobsen *et al.*, 1989). The mobility is inversely proportional to the gas density, N (Borghesani and O'Malley, 2003). "In gaseous hydrocarbons, electronic mobilities at low fields are constant; they vary linearly as $1/N$ (N, number of molecules per unit volume; $N = A_N \rho / M$; A_N is the Avogadro number; ρ mass per unit volume; M molecular mass)," (p.1135, Tobazcon, 1994). The normalized mobility is usually defined as $\mu_0 N$ at a zero-electric field. Increasing the density for the saturated vapor decreases μ_0 (Jacobsen *et al.*, 1989). The effects of density depend on the liquid, gas, or vapor being studied; for example, the denser the material, the higher the mobilities which means solids would have the highest mobility. There are some substances in which the density has a negative effect and others in which the density has a positive effect. The density is affected by various factors such as temperature, structure, and pressure.

1.3.2   Temperature

The mobility for all material phases is affected by the temperature. The mobility can be related to the diffusion coefficient,

$$\mu = {}^{De}\!/_{(k_b T)},\tag{1.50}$$

where D is the diffusion coefficient, k_b is Boltzmann's constant, e is the elementary electron charge, and T is the temperature (Allen, 1976). Changing the temperature can increase thermal motion, which may cause electrons to transition between states. There are few equations that model the temperature dependence of the mobility. The one model that is commonly used to model μ as a function of temperature is the Arrhenius temperature relationship; this however is typically used for low mobilities (Muñoz *et al.*, 1987; Schmidt, 1977). Equation 1.51,

$$\mu(T) = \mu_0 \exp(-E_a/(k_b T)),\tag{1.51}$$

is the Arrhenius equation in which the initial, zero-field mobility, μ_0, ranges from 100 to 1000 $cm^2 \cdot V^{-1} s^{-1}$ (Schmidt, 1977). Also, the E_a is the activation energy, and k_b is Boltzmann's

constant. In general, a low mobility will increase with temperature, and a high mobility is practically independent of temperature (Christophorou and Siomos, 1984). Sometimes the mobility follows a T^{-1} dependence (Christophorou and Siomos, 1984), and that is why equation 1.52 is sometimes used to calculate mobility (Muñoz and Holroyd, 1986),

$$\mu(T) = \left(\frac{\mu_0}{T}\right) \exp(-E_a/(k_b T)).$$
(1.52)

The Arrhenius relationship does not work for liquids like TMS because of the high mobility. For TMS at low pressure, the mobility increased as the temperature increased (Muñoz and Holroyd, 1986). When the density for TMS was constant, the mobility decreased as the temperature increased (Muñoz and Holroyd, 1986). At low pressure, the mobility for n-Hexane increased as the temperature increased; an increase in temperature at a constant density lead to the increase in mobility (Muñoz and Holroyd, 1986). Finally, for TMP, the mobility increased as temperature increased, and the density remained constant (Muñoz and Holroyd, 1986). The mobility of a substance is heavily reliant on the temperature.

1.3.3   Electric Field

The electric field also effects the mobility. The following relationship has been provided through numerous sources (Allen, 1976; Halpern and Gomer, 1969a; Schmidt, 1977),

$$v_d = \mu F$$
(1.53)

$$\mu = \frac{v_d}{F}.$$
(1.54)

In this relationship, F is the electric field and v_d is the drift velocity. In general, for $\mu < 1 \, cm^2 \cdot V^{-1}s^{-1}$, the relationship described in equations 1.53 and 1.54 holds. Different relationships between mobility and electric field do exist in the literature. Some results have demonstrated a sublinear relationship between drift velocity and the electric field (Schmidt, 1977), given by $v_d \propto F^{0.5}$. For these sublinear relationships, $\mu > 10 \, cm^2 \cdot V^{-1}s^{-1}$ (Lewis, 1994). This relationship is thought to occur because of the increase of the Boltzmann temperature. This is general behavior, and it appears that the relationship between electric field and mobility changes with the type of liquid or gas being used. For some hydrocarbons, such as ethane and propane, with low mobilities, $\mu < 1 \, cm^2 \cdot V^{-1}s^{-1}$, the relationship is superlinear above a certain electric field strength (Schmidt, 1977). After this superlinear region, there appears to be a linear region with a higher mobility and electric field strength (Schmidt, 1977).

A constant mobility μ_0 can be found for normalized electric field E/n where n is the number density of molecules (number of molecules/m^3), below a certain threshold value. For vapors, μ increased above the E/n threshold (Jacobsen *et al*., 1989). There was a point at which the μ reached a maximum and started to decrease with increasing E/n (Jacobsen *et al*., 1989). These relationships between E and μ appear to depend on the liquid or gas under study.

1.3.4 Pressure

The dependence of μ on pressure seems to be interconnected with T. A few experiments have determined μ for liquids, vapors, and gases at high pressures. To examine this relationship, one experimental study looked at μ for hydrocarbons (TMP, TMS, and n-Hexane) at different temperatures and pressures (Muñoz and Holroyd, 1986; Muñoz *et al*., 1987). For TMS, μ decreased with increasing pressure. As both the temperature and pressure increased, μ decreased (Muñoz and Holroyd, 1986). As the pressure increased for n-Hexane, μ decreased; as both the temperature and pressure increased, μ decreased (Muñoz and Holroyd, 1986). For temperatures below 100 °C, the mobility of TMP increased as the pressure increased; it was the opposite for temperatures above 100 °C. From this experiment, they determined that there are three classifications of liquids in regard to pressure temperature relationships. The first classification occurs in the temperature range of 20-120 °C, and in this temperature range the mobility decreases with pressure (Muñoz *et al*., 1987). The liquids in the first classification have a low μ at room temperature and standard pressure (Muñoz *et al*., 1987). The second classification (for higher μ) is that "the mobility decreases slightly with pressure at any temperature but the degree of decrease is somewhat greater at higher temperatures," (p.4639, Muñoz *et al*., 1987). Liquids belonging to the second classification are similar to TMS. The third classification (for intermediate μ) states for room temperature, μ will increase with pressure (Muñoz *et al*., 1987). Once the temperature increases above room temperature, μ will decrease with pressure (Muñoz *et al*., 1987).

1.4   Conclusion

Electronic processes in gases and liquids have been analyzed since the second half of the 19th century, and the processes are continually being analyzed today. As time progressed, these theories have been adapted and modified as the experimental technologies have advanced. Due to the

constant modifications applied to these theories, the history behind the electronic processes are relatively complex. However, many of the original theories for electronic breakdown and electron emission are used along with the corrected theories.

Electron emission is a heavily researched electronic process in gases. However, these mechanisms were often researched separately or in pairs; some of this emission mechanisms are FE, TE, SCLE, and PE. Recently, the research has been focused on unifying multiple emission theories to model transition points. This unification provides a more comprehensive understanding of the conditions and factors required for the transitions between the different emission mechanisms; the current model unifies TE, FE, and SCLE in gases. However, there are still emission mechanisms that can be added to the unification model, such as PE. These electron emission mechanisms have yet to be unified in other phases such as liquids, vapors, or solids. If the unification model for gases could be adapted for liquids, vapors, or solids, it could be used to model electron emission for the transitions between the phases, which may be valuable for applications involving electric fields that undergo phase changes, such as combustion and plasma sterilization of liquids.

There are aspects of the electronic process research that are mentioned briefly but have profound effects on the results. Mobility and geometry are just two of the factors that affect the research in this field. Mobility μ depends on the material, temperature, structure, density, and electric field; however, it is often assumed to be constant when used in electron emission and breakdown analysis. This assumption might hinder the accuracy of these models, particularly over broad parameter ranges. However, due to the influence mobility has on the electron emission processes, it would be beneficial to have a comprehensive mobility study for specific solids, liquids, vapors, and gases to understand the transition points and the factors that most strongly influence the mobility. In fact, for solids, the space-charge limited current is often used to determine the mobility of the material rather than the mobility being know *a priori*. A comprehensive study of mobility could then be used to find a more accurate way to incorporate mobility into electron emission studies. The present thesis considers constant mobility for simplicity since such information is not yet readily available.

The applications for electronic processes are numerous. They can be used for radiation measurement, which includes dosimetry (Chu *et al*., 1980), X-rays (Schmidt, 1984), or LRGD (Lopes and Chepel, 2003). The electronic processes can also be used to form plasma which can be

used for food and water decontamination (Foster, 2017; Xu *et al*., 2017). Geological and seismic applications use electronic processes to map the ocean floor (Caulfield, 1962; Olson and Sutton, 1993), analyze bore holes for drilling (Olson and Sutton, 1993; Rechtien *et al*., 1993; Vogel, 1952), or oil exploration (Caulfield, 1962; Jones and Kunhardt, 1995b; Olson and Sutton, 1993); the electronic process most important to this field is arcing. One of the bigger application fields is pulsed power (Garner *et al*., 2017; Jones and Kunhardt, 1995b; Schoenbach *et al*., 2008; Zahn *et al*., 1986); this includes looking at insulation and heat transfer agents for transmission lines and medical applications for treating cancer. Electrospray is important for space applications as thrusters (Gaskell, 1997; Krejci *et al*., 2017); it can also be used in combination with combustion. For gases, electron emission, especially PE, can be used to model the necessary processes related to lasers (Brau, 1998; Jensen *et al*., 2006a; Jensen *et al*., 2006b; O'Shea *et al*., 1993; O'Shea, 1998; O'Shea and Freund, 2001). The many applications for electronic processes show the importance of understanding the transitions between the electron emission and breakdown in both liquids and gases.

1.5   Problem statement and scope of thesis

This thesis extends this research into electron emission unification, referred to as "nexus" theory, in two directions. First, we will apply this theory to liquids to examine the transition from FE to SCLE and hypothesize about the implications should there be a phase change. Second, we will extend nexus theory to include PE, which becomes important with increasing interest in ultrafast laser phenomena at nanoscale and development of solar cells, with SCLE, TE, and FE.

Chapter 2 develops a unified theory for electron emission in liquids. This research addresses the possibility of using a unification model for electron emission in gases for liquid electron emission data. This unification model connects FN, CL, and MG using nexus theory to examine the transitions between the different electron emission mechanisms. The goal of this project is to determine the validity of using this model for liquids to provide an understanding of the transitions between the electron emission. The validity of the model is determined using an orthodoxy test and error analysis. For this research, the results include a typical current density versus voltage figures to demonstrate the correlation between the model and the data. The other figures demonstrate the usefulness of nexus theory when analyzing the transitions between emission mechanisms. This section was published as a refereed journal article (S. A. Lang, A. M. Darr, and

A. L. Garner, "Theoretical analysis of the transition from field emission to space-charge-limited emission in liquids and gases," J. Appl. Phys. **128**, 185104 (2020).).

Chapter 3 addresses the missing photoemission in the unification model for electron emission mechanisms. The goal of this project is to include the PE into the emission model using the nondimensionalized asymptotic limits for the MFD equation. Using these asymptotic limits, we can find a sixth order nexus point between RLD, FN, CL, MG, OL, and MFD. These nexus relationships can be used to develop nexus plots or transition plots to understand at what conditions each emission mechanism dominates. For this research we expect to build the nexus plots step by step to ensure a thorough understanding of the meaning of the plots. The common current density versus voltage plots will also be developed to look the relationship between the mechanisms and the effects of certain parameters such as wavelength and laser intensity. The section is a manuscript under development.

2. THEORETICAL ANALYSIS OF THE TRANSITION FROM FIELD EMISSION TO SPACE-CHARGE-LIMITED EMISSION IN LIQUIDS AND GASES

2.1 Introduction

While electron emission is well characterized in gases from vacuum to atmospheric pressure (Akimov and Schamel, 2002; Bhattacharjee *et al*., 2008; Bhattacharjee and Chowdhury, 2009; Darr *et al*., 2019a; Dynako *et al*., 2019; Feng and Verboncoeur, 2006; Ingold, 1969a; Ingold, 1969b; Lau *et al*., 1994; Luginsland *et al*., 1996 and its contribution to gas breakdown at microscale gaps and atmospheric pressure has increased in relevance with continuing reduction in electronic devices (Brayfield et al., 2019; Fu *et al*., 2020; Garner *et al*., 2020b; Go and Venkattraman, 2014), fewer studies have characterized these phenomena in liquids (Bragg *et al*., 1954; Halpern and Gomer, 1965; Halpern and Gomer, 1969a; Halpern and Gomer, 1969b; McClintock, 1969; Schmidt, 1984; Sharbaugh *et al*., 1978). Broadly speaking, characterizing electron processes in dielectric liquids has broad implications in multiple areas, including radiation physics/chemistry, field induced polymerization, nuclear radiation detection, medical imaging, insulator physics, composite insulation, high power capacitors, pulsed power systems, and electrostatics generators (Schmidt, 1984). The characterization of electron processes in liquids includes understanding electron emission (field emission in particular) as one of the initial phases in the development of electronic breakdown (Auger *et al*., 2016; Phan *et al*., 2020; Qian *et al*., 2005); the electron emission at the cathode initiates the release of electrons that leads to breakdown (Auger *et al*., 2016; Phan *et al*., 2020).

Phenomenologically, characterizing electron emission in liquids is important for understanding breakdown, or plasma formation, in liquids. Electron emission in liquids is potentially relevant in multiple applications, such as electric pulse applications in medicine and sterilization (Garner *et al*., 2017) , plasma treatments of liquids for food and water decontamination (Foster, 2017; Xu *et al*., 2017), combustion (Bankston *et al*., 1988; Krejci *et al*., 2017), and field emission electric propulsion for flexible propulsion of satellites (Marcuccio *et al*., 1998;

Levchenko *et al*., 2020). While many of these applications have grown in importance over the past two decades, many of the pertinent investigations in electron emission in liquids occurred over thirty years ago, motivating the present study to revisit the mechanistic behavior of this phenomenon.

Many electron emission studies consider vacuum, where one achieves field emission in a diode by raising the voltage to a sufficient level to ultimately strip electrons from the cathode, as predicted by the Fowler-Nordheim (FN) equation (Fowler and Nordheim, 1928; Murphy and Good, 1956; Lau *et al*., 1994). Raising the current introduces more electrons into the gap. Eventually, the negative charge buildup in gap becomes sufficiently strong to prevent further electron emission, making the diode space-charge limited (SCL). At vacuum, SCL current is predicted by the Child-Langmuir (CL) law (Child, 1911; Langmuir, 1913; Lau *et al*., 1994). At non-vacuum pressures, such as when vacuum devices may have leaks that raise the pressure, or when one is operating at atmospheric pressure for electronics devices or microplasma applications for combustion or medicine (Schoenbach and Becker, 2016), collisions may cause emission to become SCL by the Mott-Gurney (MG) law, which is a function of the electron mobility μ in the gap (Darr *et al*., 2019a; Mott and Gurney, 1940). For gap distances exceeding the electron mean free path, which is on the order of several hundred nm at atmospheric pressure (Dynako *et al*., 2019; Meng *et al*., 2019), one must account for collisions when determining the SCL current. Multiple studies have considered emission mechanisms from FN to CL (Bhattacharjee and Chowdhury, 2009; Feng and Verboncoeur, 2006; Lau *et al*., 1994; Luginsland *et al*., 1996), CL to MG (Benilov, 2008; Ingold, 1969a; Ingold, 1969b) and, more recently, FN to MG to CL (Darr *et al*., 2019a; Dynako *et al*., 2019) by solving exact solutions for the electron trajectories within the gap and taking appropriate asymptotic limits for the applied voltage and electron mobility. The full theory linking FN, CL, and MG derived a nexus, defined where the asymptotic solutions for FN, CL, and MG matched at 791 Torr for a 250 μm nitrogen diode (Darr *et al*., 2019). The theory also recovered the CL law at high μ (i.e vacuum), the MG law at low μ (i.e. high pressure), and the FN law at low voltage V independent of μ. The resulting equations were valid for any planar diode where the emitted electrons will interact with particles.

This leads to the consideration of the applicability of the theoretical approach from Refs. (Darr *et al*., 2019a) and (Dynako *et al*., 2019) to a diode containing liquid defined by an electron mobility μ. Bragg, et al. described phenomena concerning electron transport, inhomogeneous

electric field, SCL emission, and breakdown in a liquid, which resemble the description above for a gas with collisions (Bragg *et al*., 1954). Halpern and Gomer carried out the first measurements of field emission in liquid H_2, D_2, He, benzene, O_2, and Ar, demonstrating FN-scaling at lower currents and SCL emission at higher currents (Halpern and Gomer, 1965; Halpern and Gomer, 1969a), similar to the theoretical (Darr *et al*., 2019a; Dynako *et al*., 2019; Feng and Verboncoeur, 2006; Lau *et al*., 1994; Luginsland *et al*., 1996) and experimental observations (Bhattacharjee and Chowdhury, 2009) for gases. These studies showed that electron emission in liquid He and Ar transitioned to SCL emission, abruptly leading to electron avalanching with concomitant gas-bubble formation at the tip. This gas-bubble formation, which is also important in water purification (Foster, 2017), was a pre-breakdown phenomenon. Dotoku *et al*. measured FE in n-Hexane, trimethylpentane (TMP), and tetramethylsilane (TMS) (Dotoku *et al*., 1978). They observed a transition from FE to SCLE for these nonpolar liquids and that SCLE in liquids was more dominant than SCLE in vacuum due to the charge carrier velocity in liquids (Dotoku *et al*., 1978). We will focus our study on these nonpolar liquids to demonstrate the utility of our approach; such a process may ultimately be extended to other liquids (Halpern and Gomer, 1965; Halpern and Gomer, 1969a).

Properly modeling electron emission requires adequately accounting for other factors that may influence the relationship between current and voltage. Two critical factors when accounting for collisions in either a gas or liquid are the electron mobility (which is a function of molecular structure, temperature, pressure, electron density, and electric field) and emission area (Allen, 1976; Dotoku *et al*., 1978; McClintock, 1973; Schmidt, 1977). Thus, both the electron mobility μ and notional emission area S_n vary with experimental conditions and may be difficult to determine *a priori*. For this research, the dependence of μ on the liquid's molecular structure has the most relevance. As the molecular structure of the liquid becomes more spherical, the electron mobility generally increases (Allen, 1976; Schmidt, 1977). Of the three liquids in this experiment, n-hexane has the least spherical structure (it is a straight chain alkane), and, therefore, the lowest mobility μ (Allen, 1976 Schmidt, 1977). TMP, which is an isomer of oxane, and TMS, which has a tetrahedral shape, are more spherical than n-hexane. For this analysis, we fix μ based on values from the literature and use S_n as the notional emission area, which can be corrected to the formal emission area S_f using a correction factor λ_c, which we address later (Forbes, 2012; Forbes, 2013; Forbes *et*

al., 2015). The different shapes of the molecules may also play a role in the significantly different S_n that we note later between n-hexane and the other liquids.

This paper addresses the applicability of the theory from unifying SCLE and FE for gases to liquids (Darr *et al*., 2019; Dynako *et al*., 2019). After demonstrating the utility of this theory to both liquids and gases, we conjecture about the potential utility across the range of phases from liquid to gas, which undergo a change in electron mobility during the phase change. This provides the ability to characterize electrical emission as the phase of the material under electric field exposure changes, which may be valuable for combustion applications using liquid fuel. Section 2.2 summarizes the theory and the modifications required for adapting the theory from Refs. (Darr *et al*., 2019a) and (Dynako *et al*., 2019) to apply it to experimental data. Section 2.3 applies the theory to experimental data and extrapolates the application across phases from liquid to gas. We summarize the results and make concluding remarks in Section 2.4.

2.2   Model Derivation

2.2.1   Basic Electron Emission Theory

We consider electron emission in a liquid with mobility μ to behave similarly to a gas with mobility μ, which we have studied previously by solving for the trajectory of a single electron emitted from the cathode at $x = 0$, $t = 0$ with a current density J as it travels to the anode at $x = d$ (for the diode under consideration, the geometry may simplified to planar by considering it as two plates separated by a distance d) (Darr *et al*., 2019; Dynako *et al*., 2019). The cathode is grounded with potential $\Phi(0) = 0$ and the anode is biased at $\Phi(d) = V$ (Barbour *et al*., 1953). Similarly, we use the following initial conditions at $t = 0$: $E(0) = E_s$, $x(0) = 0$, $v(0) = 0$, and $a(0) = eE_s/m$, where E is electric field, E_s is the electric field at the cathode, x is electron position across the gap, v is electron velocity in the *x*-direction, a is electron acceleration, e is electron charge, and m is electron mass. For gases, we considered fixed μ in the analysis and then translated from μ to pressure P by using semi-empirical relationships in the literature (Darr *et al*., 2019; Dynako *et al*., 2019); liquid studies generally consider μ directly, so we use relevant references for those values. Theories for electron emission in liquids have considered both fixed μ and $\mu(E)$. For this study, we fixed μ since the range of E considered in the experiments is relatively narrow such that we do not anticipate significant variation in μ. Moreover, upon demonstrating the applicability of this model

51

for liquids, we can further apply this approach to examine electron emission as the phase transitions from liquid to gas (or to a dense gas state) as long as we account for the variation in μ, which has been done for several materials (Huang and Freeman, 1978; Jacobsen *et al.*, 1986; Jacobsen *et al.*, 1989; Wada and Freeman, 1979).

The general process for modeling electron emission in liquids resembles that for gases. Coupling electron continuity, given by $J = env$, where J is the current density, n is electron number density, and v is electron velocity, with Poisson's equation, given by $d^2\Phi/dx^2 = \rho/\varepsilon_0$, where ρ is electron charge density and ε_0 is the permittivity of free space, yields

$$\frac{d^2\Phi}{dx^2} = \frac{J}{\varepsilon_0 v}. \tag{2.1}$$

We consider the current density in terms of the Fowler-Nordheim (FN) equation for field emission current, given by

$$J_{FN} = E_s^2 A_{FN} \exp(-B_{FN}/E_S), \tag{2.2}$$

where A_{FN} and B_{FN} are the FN constants, which are functions of the electrode work function ϕ and field enhancement factor β. The dependence of A_{FN} and B_{FN} on ϕ and β is implicitly included in the form given in (2.2); other variations of J_{FN} include this dependence explicitly (Brayfield et al., 2019). The equation for electron motion through the liquid is

$$m\frac{dv}{dt} = e\frac{d\Phi}{dx} - \frac{ev}{\mu}, \tag{2.3}$$

where the first term on the right-hand side represents the electric force on the electron and the second term represents the friction due to electron collisions with particles within the liquid (Darr *et al.*, 2019a).

2.2.2   Application of theory to experimental data

Applying this approach to experimental data for liquid emission requires converting (2.1), (2.2), and (2.3) into a form that predicts the measured parameters. Specifically, experiments typically apply a bias voltage V and measure current I, rather than current density J. Converting from J to I (or vice versa) requires appropriately accounting for the appropriate emission area S such that $I = JS$, which is difficult to predict *a priori*. The experimental geometry is a pin-to-plate geometry with a sharp tip tungsten (W) emitter Dotoku *et al.* (1978) simplified the pin-to-plate geometry to a concentric spherical geometry containing emitters with radius r_t and solid angle $\alpha\pi$.

Alternatively, the sharp-tip emitter geometry may be modeled as a parallel plate geometry by appropriately modifying β, which modifies A_{FN} and B_{FN} (Barbour *et al*., 1953; Lau *et al*., 1994). It is important to note that SCL current (SCLC) depends strongly on diode geometry. Langmuir and Blodgett derived mathematical equations for SCLC in vacuum for concentric spheres and cylinders that depended on a series expansion that tends to diverge when the radii of the two spheres/cylinder diverge (Langmuir and Blodgett, 1923; Langmuir and Blodgett, 1924). Darr and Garner recently derived a condition for SCLC in vacuum that is true for any geometry where the coordinate system has a defined gradient and Laplacian using variational calculus (Darr and Garner, 2019). They used this approach to derive an exact, closed form solutions for SCLC for concentric cylinders and spheres from first principles (Darr and Garner, 2019). Applying variational calculus to a pin-to-plate geometry yields the SCLC for the tip J_{SCL}^{tip} as (Harsha and Garner, 2020)

$$\frac{J_{SCL}^{tip}}{J_{CL}} = \frac{\beta(1+\beta)}{\left(\ln(\sqrt{1+\beta}+\sqrt{\beta})\right)^2}, \tag{2.4}$$

where

$$\beta = \sqrt{d/r_t} \tag{2.5}$$

and J_{CL} is the SCLC in vacuum, given by

$$J_{CL} = \frac{4\sqrt{2}}{9}\varepsilon_0\sqrt{\frac{e}{m}}\frac{V^{3/2}}{d^2}, \tag{2.6}$$

where ε_0 is the permittivity of free space. For the experimental geometry (Dotoku *et al*., 1978), d = 2 mm and r_t = 0.5 mm, which yields β = 2. Substituting this into (2.4) yields J_{SCL}^{tip}/J_{CL} = 4.57. This suggests that using the parallel plate assumption will cause less than order of magnitude underestimation in the space-charge limit, which should be sufficient for our goal of estimating conditions for the transitions in electron emission mechanisms.

In addition to the influence of diode geometry on emission area, one must also take care to define the appropriate area S in the analysis. In this case, following the notation of Forbes et al (Forbes, 2012; Forbes, 2013; Forbes *et al*., 2015), we consider two areas: the notional emission area S_n and the formal emission area S_f. In this definition, $S_n = i_e/J_C$, where i_e is the emission current and J_C is the characteristic local emission current density J_C (Forbes *et al*., 2015). Using S_n, we can recast (2.2) as

$$I = JS_n = A_{FN}E_s^2 S_n \exp(-B_{FN}/E_s) \tag{2.7}$$

where A_{FN} and B_{FN} are the FN constants that can be determined using a linear best fit for the experimental data. To determine these constants, we rewrite (2.7) in the absence of space charge as, where

$$\ln\left(\frac{I}{V^2}\right) = \ln(A'_{FN}) - \frac{B'_{FN}}{V},$$
(2.8)

where we set $E_s = V/d$, $A'_{FN} = A_{FN}S_n/d^2$, and $B'_{FN} = B_{FN}d$. We point out that the relationship between A'_{FN} and A_{FN} is not an arbitrary fitting constant but instead comes from the mathematical manipulation of the fundamental equations to obtain a form amenable to plotting on a FN plot. We will specifically outline how we obtain S_n from the experimental data.

We next plot the experimental data on a FN plot of $\ln(I/V^2)$ as a function of $1/V$. When electron emission is driven by field emission, the data will behave linearly as a function of $1/V$ in the resulting FN plot, before deviating as the contribution of space charge increases. Fitting the linear regime of the data to (2.8) yields A'_{FN} and B'_{FN}. Using A'_{FN} and B'_{FN}, we can determine the formal emission area, S_f which is the emission current, i_e divided by the characteristic kernel emission current density, J_{kC} (Forbes *et al.*, 2015). To calculate S_f, we use the second FN constant, $b = 6.83 \times 10^9 \text{ V} \cdot \text{eV}^{-3/2}\text{m}^{-1}$, the work function ϕ, the gap distance d, and B'_{FN} to calculate β using (Forbes, 2013; Forbes *et al.*, 2015)

$$\beta = \frac{b\phi^{3/2}d}{B'_{FN}}.$$
(2.9)

Now, using β, the first FN constant $a = 1.54 \times 10^{-6} \text{ A} \cdot \text{eV} \cdot \text{V}^{-2}$, and A'_{FN}, we can calculate S_f by (Forbes, 2012; Forbes, 2013; Forbes *et al.*, 2015)

$$S_f = \frac{A'_{FN}\phi d^2}{a\beta}.$$
(2.10)

This formal emission area S_f is related to the notional emission area S_n, which we use for the full emission theory in this paper for translating between A'_{FN} and A_{FN}, through the characteristic local preexponential correction factor λ_C (Forbes *et al.*, 2015), given by

$$\lambda_C = S_f/S_n,$$
(2.11)

which typically varies between 0.001 and 10 for vacuum conditions (Forbes, 2012). Because these experiments examined liquids rather than gases at vacuum conditions, it is highly likely that λ_C will not fall within that range. We determine λ_C by solving for the notional emission area S_n necessary to fit the regime where space charge begins to contribute to emission using the full

theory derived earlier for gases and whose application for liquids we shall detail below; we shall use S_n to convert A'_{FN} to A_{FN} for linking the emission theories. Because typical values of λ_C (and, later, the orthodoxy test) are considered for vacuum conditions, phenomena that may arise due to the liquid media, such as collisions, are not fully considered. Thus, the deviation of λ_C from these typical vacuum values is reasonable and will require future study with more detailed experiments for different liquids and diode geometries. Determining A_{FN} requires first obtaining S_n, which is important for converting I to J for both the field emission regime and the regime where space charge begins to dominate, by minimizing the relative error of the exact theory described below to the full data, including the portion where space charge contributes.

2.2.3 Nondimensionalization of theory

To facilitate analysis and eliminate parameters, we transform (2.1), (2.2), and (2.3) to nondimensional equations by defining (Darr *et al.*, 2019a; Dynako *et al.*, 2019)

$$\phi = \phi_0 \bar{\phi}; J = J_0 \bar{J}\,; x = x_0 \bar{x}; t = t_0 \bar{t}; \mu =, \mu_0 \bar{\mu}; E = E_0 \bar{E}; v = v_0 \bar{v}, \tag{2.12}$$

where

$$E_0 = B_{FN} \left[\frac{\text{V}}{\text{m}}\right]; \; J_0 = A_{FN} B_{FN}^2 \left[\frac{\text{A}}{\text{V}^2}\right]; \; x_0 = \frac{e\epsilon_0^2}{m B_{FN} A_{FN}^2} \; [\text{m}] \tag{2.13}$$

$$t_0 = \frac{\epsilon_0}{A_{FN} B_{FN}} \; [\text{s}]; \; \mu_0 = \frac{e\epsilon_0}{m A_{FN} B_{FN}} \left[\frac{\text{m}^2}{\text{Vs}}\right]; \; \phi_0 = \frac{e\epsilon_0^2}{m A_{FN}^2} \; [\text{eV}]; \; v_0 = \frac{x_0}{t_0} \left[\frac{\text{m}}{\text{s}}\right],$$

with the units for each term in the corresponding square brackets. Note that these are the same scaling parameters from Ref. (Darr *et al.*, 2019a); the only difference is that we determine A_{FN} and B_{FN} after fitting S_n by minimizing relative error between the exact solution (cf. (2.14)-(2.16)) and the experimental data.

Recasting (2.1), (2.2), and (2.3) in nondimensional terms gives electron velocity and position as functions of time as

$$\bar{v}(\bar{t}) = \bar{\mu}\left[(\bar{\mu}\bar{J} - \bar{E})\left(e^{-\bar{t}/\bar{\mu}} - 1\right) + \bar{J}\bar{t}\right], \tag{2.14}$$

and

$$\bar{x}(\bar{t}) = \bar{\mu}\left[(\bar{\mu}\bar{J} - \bar{E})\left(-\bar{\mu}e^{-\bar{t}/\bar{\mu}} - \bar{t} + \bar{\mu}\right) + \bar{J}\bar{t}^2/2\right], \tag{2.15}$$

respectively. Solving for the critical current density $\bar{J}(\bar{V})$ at the transit time $\bar{T}$ such that $\bar{x}(\bar{T}) = \bar{d}$ and $\bar{\phi}(\bar{T}) = \bar{V}$ for fixed $\bar{\mu}$ and $\bar{d}$ by integrating the nondimensionalized version of (2.3) with respect to $\bar{x}$ and changing variables to $\bar{t}$ gives

$$\bar{V} = \frac{\bar{v}(\bar{t})^2}{2}\Big|_0^{\bar{T}} + \int_0^{\bar{T}} d\bar{t}\,\frac{\bar{v}(\bar{t})^2}{\bar{\mu}}. \tag{16}$$

We numerically solve for $\bar{J}$ and $\bar{V}$ parametrically in terms of $\bar{E}$ by substituting the nondimensionalized version of (2.2), given by $\bar{J} = \bar{E}^2 e^{-1/\bar{E}}$, into (2.15) and evaluating at $\bar{t} = \bar{T}$. We then compute $\bar{V}$ by substituting $\bar{T}$, the nondimensionalized version of (2.2), and (2.14) into (2.16) with $\bar{\mu}$ and $\bar{d}$ fixed. This gives the exact solution for $\bar{J}(\bar{V})$, which is universal because the nondimensionalization removed the material constants. In the asymptotic limit of $\bar{\mu} \ll 1$, (2.14) - (2.16) asymptotically approach

$$\bar{J}_{MG} = 9\bar{\mu}\bar{V}^2/(8\bar{d}^3), \tag{2.17}$$

which is the Mott-Gurney limit for SCLE with collisions, and is relevant for liquids, solids, and gases with collisions (Benilov, 2008; Bragg *et al.*, 1954; Darr *et al.*, 2019a; Dynako *et al.*, 2019; Mott and Gurney, 1940). In the low current limit when space charge becomes negligible, $\bar{J} \ll \bar{\mu}\bar{E}^2/(2\bar{d})$, leading to

$$\bar{J}_{FN} = (\bar{V}^2/\bar{d}^2)e^{-\bar{d}/\bar{V}}, \tag{2.18}$$

which is simply a universal form of the FN current density from (2.2). Thus, these limits are independent of phase – they are the same for liquids, gases, and solids. We may also derive an asymptotic solution for the CL law for SCLE in vacuum ($\bar{\mu} \gg 1$), given by

$$\bar{J}_{CL} = (4\sqrt{2}/9)\bar{V}^{3/2}/\bar{d}^2. \tag{2.19}$$

The CL limit is not physically relevant for the liquids under examination here since one generally transitions from FN to MG before transitioning to CL unless $\bar{\mu}$ is sufficiently high or the gap distance is sufficiently small to move the behavior beyond the nexus where the asymptotic solutions for FN, MG, and CL match (Darr *et al.*, 2019a; Dynako *et al.*, 2019). However, as the phase changes to dense vapor and to gas, this limit may become relevant under certain conditions, as explored in Section 2.3.

2.3 Analysis

2.3.1 Determination of fitting parameters

Figure 2.1 reports the experimental data for measured current as a function of emitted voltage for n-Hexane, TMP, and TMS in both dimensional form and nondimensional form, which we shall address shortly.

Plotting the experimental data (Dotoku *et al.*, 1978) from Fig. 2.1 on a FN plot based on (2.18) yields the modified FN constants A'_{FN} and B'_{FN} from the best fit lines shown in Fig. 2.2 for n-Hexane, TMP, and TMS. While B_{FN} comes directly from B'_{FN}, A_{FN} can only be fully determined from A'_{FN} after fitting for S_n. Equation (2.18) will only fit data that is linear on the FN-plot, meaning that the gap lacks appreciable space charge; otherwise, the full solution of (2.14)-(2.16) must be used, as demonstrated shortly and used to fit for S_n. Table 2.1 reports A_{FN} and B_{FN} for each liquid from these linear best fits. Table 2.2 shows that λ_C is within the range typical for vacuum conditions for vacuum, but approximately two orders below the typical range for TMP and TMS. Because the data in this analysis is collected from liquids, we assume that the use of S_n is valid even though the values for λ_C do not fit in the typical range since various phenomena in liquids may influence the fit and require further study.
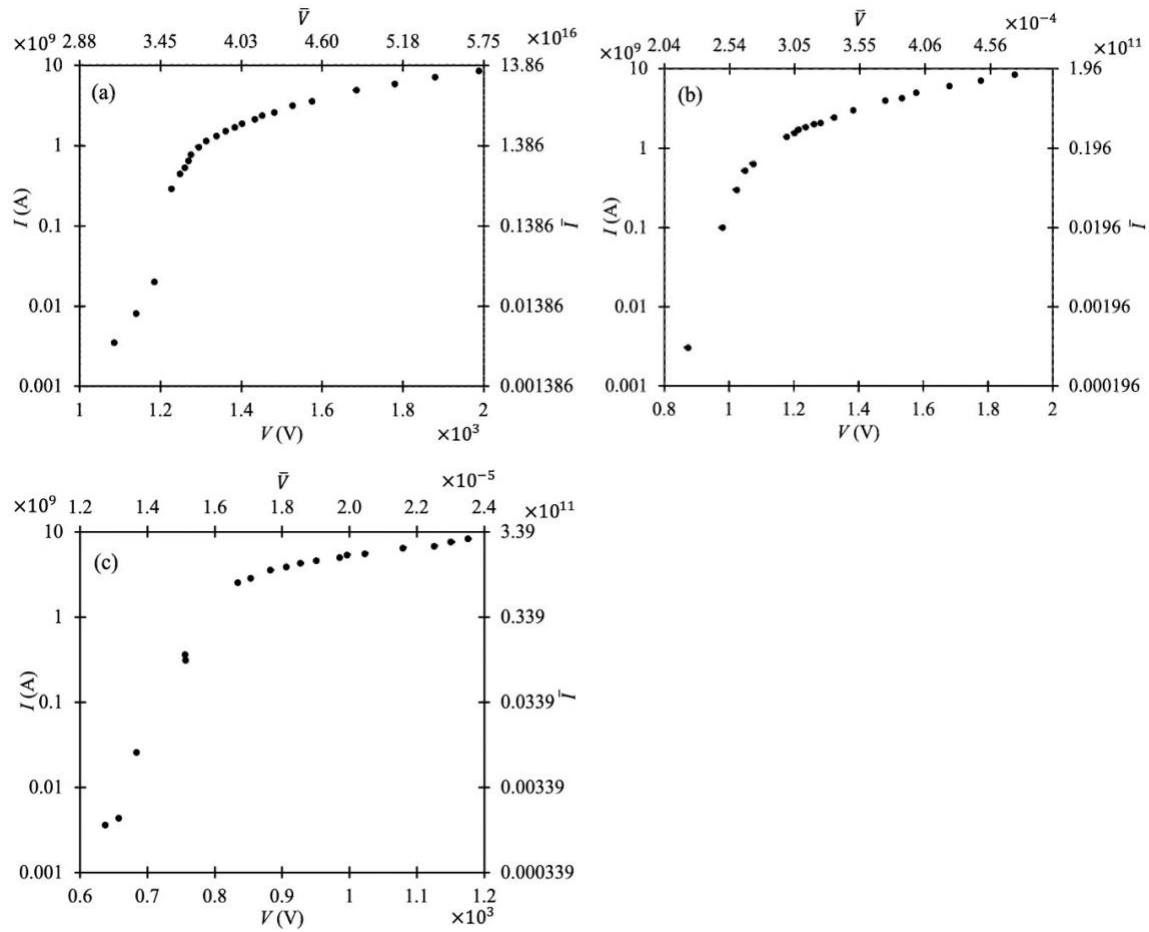
Figure 2.1. Experimental data (Dotoku et al., 1978) for emitted current as a function applied voltage for (a) n-Hexane, (b) TMP, and (c) TMS with the measurements in dimensional units on the primary axes and nondimensionalized using (2.13) and the values from Tables 2.1 and 2.3 on the secondary axes.
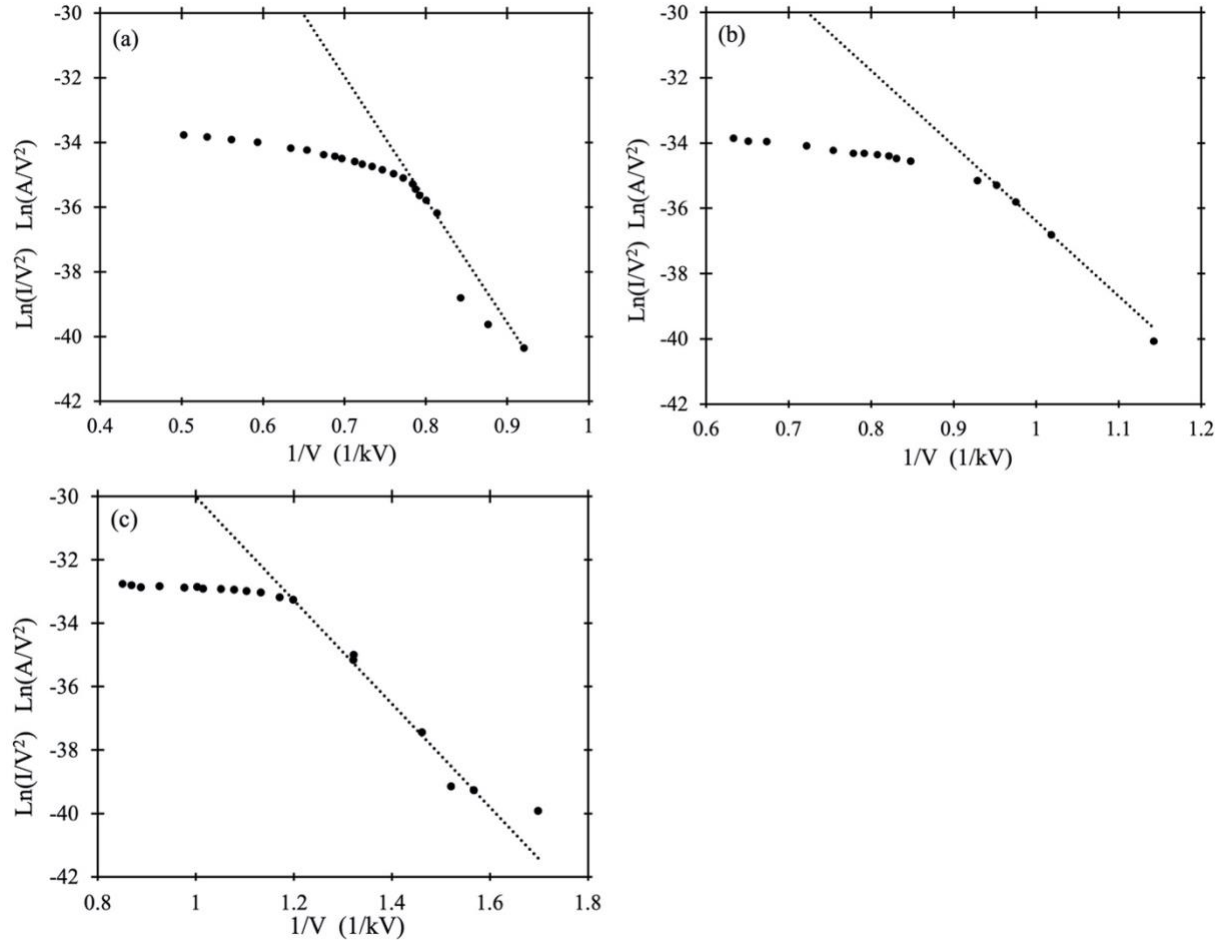
Figure 2.2. Experimental data (from Fig. 5 of Ref. (Dotoku *et al*., 1978) filled circles) on a Fowler-Nordheim (FN) plot of $\ln(I/V^2)$ as a function of $1/V$ and the best-fit lines (dotted lines) using (2.14) to determine the modified FN coefficients A'_{FN} and B'_{FN} for (a) n-Hexane, (b) TMS, and (c) TMP.

One way to assess the physical and mathematical validity of fitting current-voltage data to the FN law is to assess the degree to which the data satisfies the orthodox emission hypothesis (Forbes, 2012; Forbes, 2013; Forbes *et al*., 2015). Emission orthodoxy must satisfy the following assumptions (Forbes, 2013): (1) The voltage drop between the emitting region and the surrounding counter-electrode are uniform across the emitted surface and may be defined by the measured voltage V_M; (2) The measured current I_m equals the device current I_d; (3) I_d may be defined by an FN-type equation; (4) the local ϕ of the emitter is constant. Forbes developed a simple quantitative test to assess whether data satisfied emission orthodoxy by calculating the range of scaled barrier field f, given by (Forbes, 2013)

$$f = \frac{X}{X_R} = \frac{F}{F_R}, \tag{2.20}$$

where X is the universal variable (V in this case), X_R corresponds to the value of X when the barrier height is zero, F is the barrier field, and F_R is barrier field that reduces the barrier height to zero. Assessing emission orthodoxy requires determining the extracted range f^{extr}, given by

$$f^{extr} = \frac{-s_t \eta}{S^{fit} \cdot (X^{-1})^{expt}}, \tag{2.21}$$

where $(X^{-1})^{expt}$ is the data from the horizontal axis of the experimental FN plot, S^{fit} is the slope of the linear best fit on the FN plot, s_t is the slope correction factor that accounts for the Schottky-Nordheim (SN) barrier, and η is

$$\eta(\phi) \equiv \frac{b\phi^{3/2}}{F_R} = bc^2\phi^{-1/2} \tag{2.22}$$

where b is a FN constant, and c is the Schottky constant (Forbes, 2013). We then compare f^{extr} to the relevant orthodoxy limits. When $f_{low} \leq f^{extr} \leq f_{up}$, the orthodoxy assumption is "apparently reasonable"; when $f^{extr} < f_{lb}$ or $f^{extr} > f_{ub}$, the orthodoxy assumption is considered "clearly unreasonable." When f^{extr} falls in between the "apparently reasonable" and "clearly unreasonable," it is considered to be in the region the requires "further investigation" (Forbes, 2013). In vacuum, typical bounds for a tungsten emitter with $\phi = 4.5$ eV are $f_{lb} = 0.10$, $f_{ub} = 0.75$, $f_{low} = 0.15$, and $f_{up} = 0.45$.

We performed an orthodoxy test for each set of liquid data using the FN plot linear best fit, which is summarized in Table 2.6. Two experimental x values (1/V) from the FE regime and the resulting y values from the linear best fit were added to the spreadsheet provided in Ref. (Forbes, 2013) to calculate the values for f^{extr}_{lower} and f^{extr}_{upper}. Table 2.7 summarizes the calculated values for f^{extr}_{lower} and f^{extr}_{upper}. For these calculations, the correction factors regarding the slope were zero. For n-hexane, f^{extr}_{lower} and f^{extr}_{upper} do not fit in either the "apparently reasonable" or "clearly unreasonable" ranges, indicating that n-hexane requires "further investigation." For both TMP and TMS, f^{extr}_{lower} and f^{extr}_{upper} fall in the "clearly reasonable" range. The general orthodoxy test results suggest that orthodox emission should be reasonable accurate for two of the three liquids. However, further studies with more data points would be beneficial to account for the sensitivity of the orthodoxy test to the model fit; more data points could provide more accurate fits which in turn will yield more accurate results from the orthodoxy test.

The distinction between the two liquids that satisfy the orthodoxy requirements and the one that does not may play a role in explaining the dramatic difference in emission area that we will note later in this paper. This difference may also arise due to the chemical structure of the liquids influencing electrical properties, most notably electron mobility and electron emission. In any event, these results indicate the importance of performing additional studies on the electrical behavior of these liquids.

To determine S_n, we minimize the sum of the relative error of the exact solution of (2.13)-(2.16) to each experimental data point, given by

$$\sigma_r = \sum_{i=1}^{N} \frac{|y_i - \hat{y}_i|}{|y_i|},\qquad (2.23)$$

where y_i is the ith of N data points and $\hat{y}_i$ is the value calculated using the exact theory. Table 2.1 summarizes the resulting best fit S_n for each liquid, Table 2.3 summarizes the scaling parameters defined in (2.12)-(2.13) based on the results in Table 2.1, Table 2.4 gives the minimum σ_r for each liquid, and Table 2.5 gives the nondimensionalized μ and d. We note that S_n is much lower for n-hexane than either TMP or TMS, which are closer in magnitude. Although the exact reason for this difference is unclear, we speculate that the difference between the molecular shapes (n-hexane is a chain; TMP and TMS are more spherical) plays a role in this, as it also does in the difference in μ between these liquids.

Figure 2.3 shows the final nondimensionalized current density $\bar{J}$ as a function of $\bar{V}$. As observed for gases (Darr *et al*., 2019a; Dynako *et al*., 2019), the exact solution follows the FN law at lower $\bar{V}$ and transitions to the MG law with increasing $\bar{V}$. Under the experimental conditions considered here, the liquids generally remain in the FN regime and only begin to transition to the SCL regime, characterized by MG for liquids, rather than reaching the asymptotic MG solution. As anticipated, we do not observe a transition to CL, which may occur for vacuum.
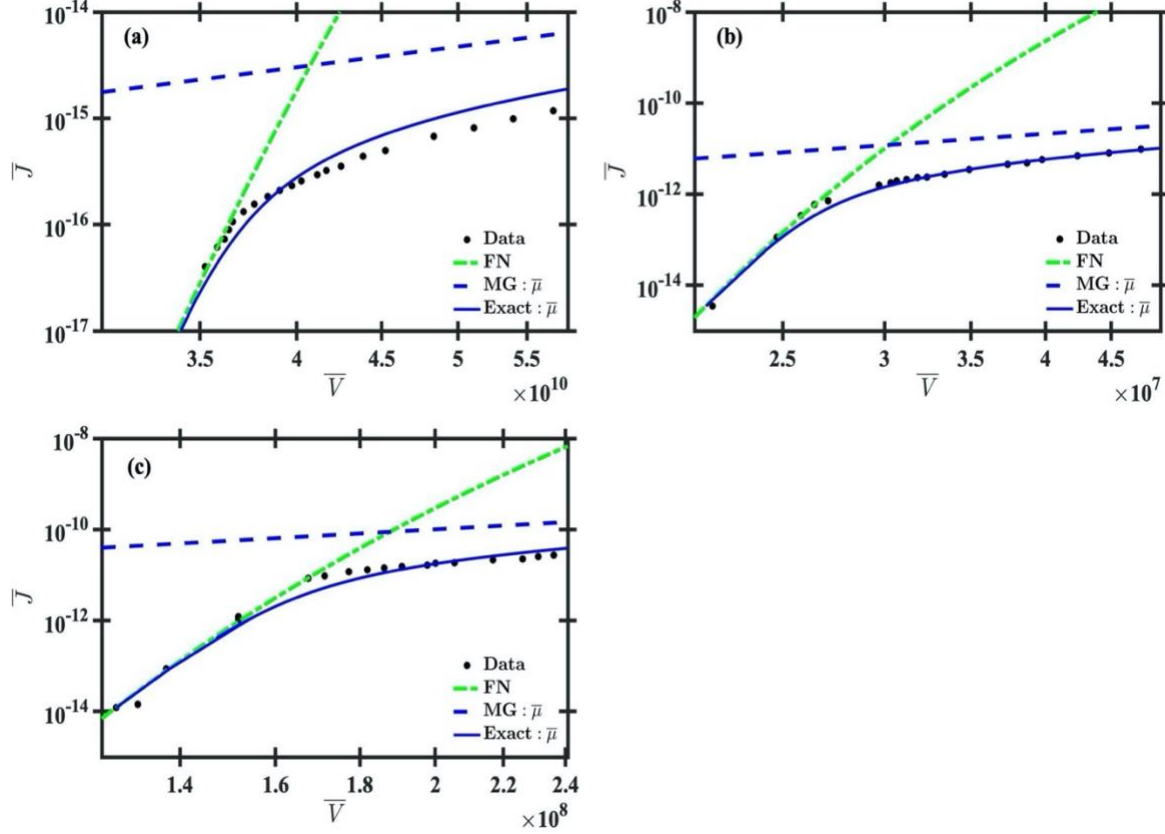
Figure 2.3. Nondimensional current density $\bar{J}$ as a function of nondimensional applied voltage $\bar{V}$ showing the experimental data (Dotoku *et al*., 1978), exact solution from (2.14)–(2.16), and asymptotic solutions of Fowler-Nordheim (FN) and Mott-Gurney (MG) from (2.18) and (2.17), respectively, for (a) n-Hexane, (b) TMP, and (c) TMS. The best fit exact solution agrees well with the experimental data over the full range of measurements for each liquid once in the field emission regime.

We correlate the actual data to the theoretical prediction by

$$R^2 = 1 - \frac{\sum(y_i - \hat{y}_i)^2}{\sum(y_i - \bar{y})^2},$$ (2.24)

where $\bar{y}$ is the mean of the actual experimental data. As examples, $R^2 = 0.5$ would indicate that the correlation between the data and the model is 50%, while $R^2 = 0.9$ would mean that 90% of the variation in data is predicted by the model. Table 2.4 summarizes R^2 for the full fits of each liquid, indicating strong correlation between the model and experimental data.

2.3.2 Sensitivity of Dominant Emission Mechanism to Parameter Selection

Given the applicability of this theory to liquids and gases, we next consider a broad range of μ that may encompass a phase change from liquid to vapor. Such a transition may be relevant in combustion, where the liquid may transition from liquid to vapor in the presence of an applied electric field and/or increased temperature.

As a preliminary assessment of the impact of phase transition on μ, we consider the behavior of n-Hexane, which we have analyzed as a liquid, and krypton, which has detailed measurements in both phases that are summarized in Tables 2.8 and 2.9 (Jacobsen *et al*., 1986; Jacobsen *et al*., 1989). Data for n-hexane vapor shows that μ can vary from ~10^{-3} $m^2V^{-1}s^{-1}$ to 1 $m^2V^{-1}s^{-1}$ for temperatures from ~2000 to 3000 °C, which is ~ two to five orders of magnitude higher than liquid n-hexane mobility (Huang and Freeman, 1978). Since we are dealing with universal curves, meaning that the results on these curves are independent of the specific material under study, we use the data for liquid and gas krypton as another example to demonstrate the variation in μ due to phase change. Table 2.8 shows that μ increases initially with increasing temperature for liquid krypton until it reaches a peak value and decreases. Table 2.8 also shows that μ is generally approximately two orders of magnitude higher for a dense gas than for a liquid; at high temperature, μ for a dense gas may be as much as four to five orders of magnitude larger, similar to the earlier described behavior of n-Hexane. Table 2.9 summarizes data for a dense krypton vapor, corresponding to the phase transition from liquid to gas. The mobility of the dense gas is generally three to five orders of magnitude higher than the dense vapor; μ for liquids may exceed the dense gas by ~50-100×. Although not definitive, other substances, most notably argon (Borghesani, 2001; Gushchin *et al*., 1982; Huang and Freeman, 1981) and nitrogen (Hirashima *et al*., 1981; Wada and Freeman, 1981), exhibit similar trends in μ. While these trends tend to change based on the structure and density of the substances (Allen, 1976; Schnyders *et al*., 1966; Wada and Freeman, 1979), this data suggests that a two order of magnitude increase and decrease in μ from the liquid condition is sufficient for a preliminary assessment of the impact of μ on emission mechanisms.

We thus selected the n-hexane data as the baseline for $\bar{\mu}$ and $\bar{d}$ for a liquid and fix $\bar{d} = 1.0931 \times 10^{12}$ increasing and decreasing $\bar{\mu}$ by two orders of magnitude to explore the range that may encompass phase change. Note that although we chose n-hexane as the baseline, carrying out this analysis using these dimensionless variables makes this assessment universal, or true for any

substance under appropriate conditions to yield the same dimensionless conditions. Figure 2.4 shows the exact solution and the asymptotes for FN, MG, and CL for $\bar{\mu} = 2.19 \times 10^{-2}, 2.19 \times 10^{0}$, and 2.19×10^{2} to capture this range of behavior. Our prior studies (Darr *et al.*, 2019; Dynako *et al.*, 2019) indicated that increasing $\bar{\mu}$ causes $\bar{J} \rightarrow \bar{J}_{CL}$ with increasing $\bar{V}$ while $\bar{J} \rightarrow \bar{J}_{MG}$ at lower $\bar{\mu}$. Figure 2.4 shows that increasing $\bar{\mu}$ to 2.19×10^{2} causes $\bar{J}$ to rapidly approach $\bar{J}_{CL}$, while both from $\bar{\mu} = 2.19 \times 10^{-2}$ and $\bar{\mu} = 2.19 \times 10^{0}$ approach $\bar{J}_{MG}$ at much higher $\bar{V}$ than plotted here. From a practical perspective, the experimental data for n-Hexane at $\bar{\mu} = 2.19 \times 10^{0}$ followed FN up to $\bar{V} \approx 10^{11}$ before beginning to approach MG. These results suggest that increasing $\bar{\mu}$ by two orders of magnitude, loosely corresponding to a transition to a gaseous state, is not sufficient to induce electron emission to transition to CL for the present design, particularly $\bar{d}$. However, it suggests that adjusting $\bar{d}$ may make it feasible for electron emission to transition from FN to MG to CL with a phase change.
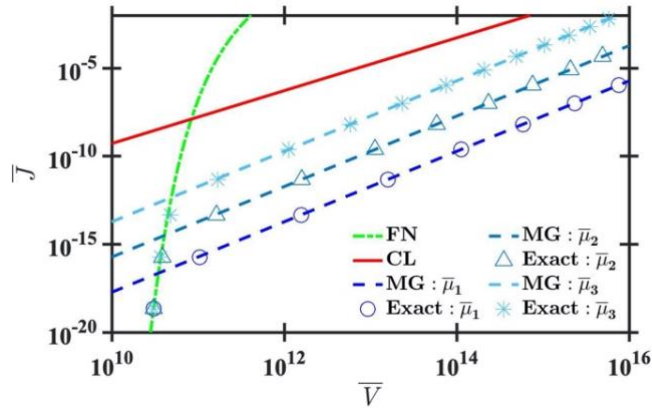
Figure 2.4. Universal curves for current density $\bar{J}$ as a function of $\bar{V}$ for various $\bar{\mu}$ with $\bar{\mu}_2 = 2.19 \times 10^{0}$ selected as the baseline based on the n-hexane measurements and asymptotic solutions for Fowler-Nordheim (FN), Mott-Gurney (MG), and Child-Langmuir (CL) from (2.18), (2.17), and (2.19), respectively. We consider $\bar{\mu}_1 = 2.19 \times 10^{-2}$, $\bar{\mu}_2 = 2.19 \times 10^{0}$, and $\bar{\mu}_3 = 2.19 \times 10^{2}$ to account for $\bar{\mu}$ that may correspond to a phase change from liquid to dense vapor or gas.

Based on our prior observations on the impact of gap distance on emission for gases (Darr *et al.*, 2019a; Dynako *et al.*, 2019), we anticipate that changing $\bar{d}$ should also influence the emission mechanism. Considering our baseline case for n-Hexane of $\bar{\mu} = 2.19 \times 10^{0}$ and $\bar{d} = 1.0931 \times 10^{12}$, we assess the impact of $\bar{d}$ on electron emission by decreasing and increasing $\bar{d}$ by an order of magnitude to 1.0931×10^{10} and 1.0931×10^{14}, respectively. Setting $\bar{d} = 1.0931 \times 10^{14}$ necessitates a very large $\bar{V}$ before space charge influences emission. Reducing

$\bar{d}$ to 1.0931×10^{10} leads to a rapid transition from FN to MG, as well as the potential to approach CL at a $\bar{V}$ that may potentially be feasible. These results, shown in Fig. 2.5, suggest that the influence of space charge to emission in liquids is very sensitive to gap distance. Although it seems unlikely that one would approach CL for a liquid before other effects of strong electric field may become dominant, these results suggest that reducing the gap size by an order of magnitude for n-hexane would clearly lead to emission becoming dominated by space charge through MG very quickly with increasing voltage. These results also indicate that liquids that may yield similar nondimensional parameters may achieve CL, although the likelihood of this occurring requires further study.
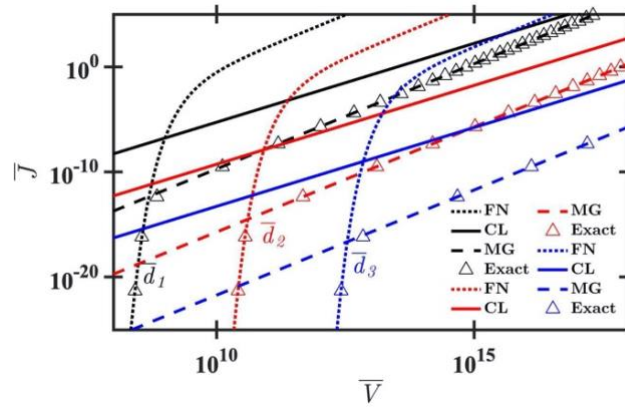
Figure 2.5. Universal curves for nondimensional current density $\bar{J}$ as a function of nondimensional applied voltage $\bar{V}$ showing asymptotic solutions for Fowler-Nordheim (FN), Mott-Gurney (MG), and Child-Langmuir (CL) asymptotic solutions from (2.18), (2.17), and (2.19), respectively, and the exact solutions for $\bar{d}_1 = 1.0931 \times 10^{10}$ (black), $\bar{d}_2 = 1.0931 \times 10^{12}$ (red), and $\bar{d}_3 = 1.0931 \times 10^{14}$ (blue). Decreasing $\bar{d}$ causes electron emission to more quickly transition from FN to MG. Reaching CL requires a much higher $\bar{V}$ than used experimentally, even for the smaller gap size. Increasing $\bar{d}$ necessitates a very large $\bar{V}$ to achieve MG, making it much more likely for electron emission to remain characterized by FN.

Now that we have examined the sensitivity of the predicted $\bar{J} - \bar{V}$ curves to variations in $\bar{\mu}$ and $\bar{d}$, we assess the nexus plots that arise when setting the asymptotic solutions from (2.17)-(2.19) for the FN, MG, and CL, respectively, equal. Although the CL asymptote was irrelevant for assessing the experimental liquid data studied in Figs. 2.1-2.3, it becomes relevant as we transition to the gas phase and sufficiently reduce $\bar{d}$ or increase $\bar{\mu}$ and/or $\bar{V}$. Figure 2.6a shows $\bar{V}$ as a function of $\bar{d}$ for $\bar{\mu} = 2.19 \times 10^0$. Figure 2.6b shows $\bar{V}$ as a function of $\bar{\mu}$ for $\bar{d} = 1.0931 \times 10^{12}$.

As for prior studies for gases (Darr *et al*., 2019a; Dynako *et al*., 2019), Fig. 2.6a shows that FN dominates for large $\bar{d}$ and low $\bar{V}$. Raising $\bar{V}$ increases the space charge in the gap and makes electron emission driven by MG. Eventually, increasing $\bar{V}$ gives the electrons enough energy to traverse the gap as if the liquid were not present, leading to a transition to CL, even at high $\bar{d}$. Realistically, we do not anticipate such behavior for most liquid conditions unless the gap is very small. For sufficiently small $\bar{d}$, the probability of collisions becomes so small that the gap effectively behaves as vacuum, causing emission to transition directly from FN to CL, as in vacuum (Darr *et al*., 2019a; Dynako *et al*., 2019; Lau *et al*., 1994). This condition arises when the MG, CL, and FN asymptotes all match and is defined uniquely by selecting $\bar{d}$, $\bar{\mu}$, or $\bar{V}$ according to

$$\bar{d} = \bar{V} \ln\left[\left(9\sqrt{\bar{V}}\right)/\left(4\sqrt{2}\right)\right]. \tag{2.25}$$

in terms of gap distance and

$$\bar{\mu} = \bar{d}\left(\frac{16\sqrt{2}}{81\sqrt{\bar{V}}} + \frac{4}{9}e^{-\bar{d}/\bar{V}}\right), \tag{2.26}$$

in terms of mobility. The mobility may be written solely in terms of voltage as

$$\bar{\mu} = \left(32\sqrt{2\bar{V}}/81\right)\ln\left[9\sqrt{\bar{V}}/\left(4\sqrt{2}\right)\right]. \tag{2.27}$$
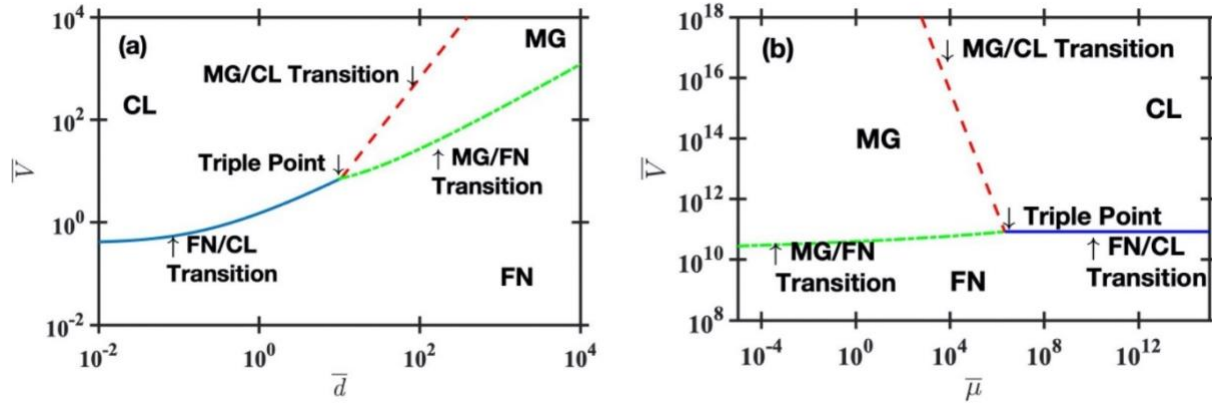
Figure 2.6. Nexus plot demonstrating the conditions for the transitions between the Fowler-Nordheim (FN), Mott-Gurney (MG), and Child-Langmuir (CL) asymptotic solutions from (2.18), (2.17), and (2.19), respectively, equal. (a) Nondimensionalized voltage $\bar{V}$ as a function of the emitter radius $\bar{d}$ for $\bar{\mu} = 2.19 \times 10^0$. A third order nexus, or triple point, occurs when the three asymptotes match based on (2.25). (b) Nondimensionalized voltage $\bar{V}$ as a function of electron mobility $\bar{\mu}$ for $\bar{d} = 1.0931 \times 10^{12}$. Again, a third order nexus, or triple point, occurs when the three asymptotes match based on (2.27).

Figure 2.6b shows the implications of changing electron mobility $\bar{\mu}$ for $\bar{d} = 1.0931 \times 10^{12}$. In this case, increasing $\bar{V}$ causes the transition from FN to CL at high $\bar{\mu}$ (corresponding to easier electron flow through the medium) and MG at low $\bar{\mu}$ (corresponding to more collisions between the electrons and the neutral atoms in the medium). For n-Hexane, the mobility corresponding to the third order nexus, or triple point, is approximately four orders of magnitude higher than the typical liquid value, meaning that one would need to be in a gaseous state to approach this value for n-Hexane at the $\bar{d}$ considered experimentally.

Figure 2.7 shows the third order nexus between FN, MG, and CL where all three asymptotic solutions match, which is uniquely defined by selecting $\bar{d}$, $\bar{\mu}$, or $\bar{V}$ from (2.25)-(2.27). For $\bar{\mu}$ above this nexus, one directly transitions from FN to CL with no intermediate CL regime. Based on the typical values shown here, this condition is most likely only feasible for a sufficiently high $\bar{\mu}$ in the gas phase. Similarly, for $\bar{d}$ below this value, electron emission will directly transition from FN to CL with no intermediate CL regime. As an example, for $\bar{d} = 1.0931 \times 10^{12}, \bar{\mu} \approx 10^7$, which is several orders of magnitude higher than $\bar{\mu}$ considered here, suggesting that we are far away from the point where vacuum effects from CL will be of consideration.
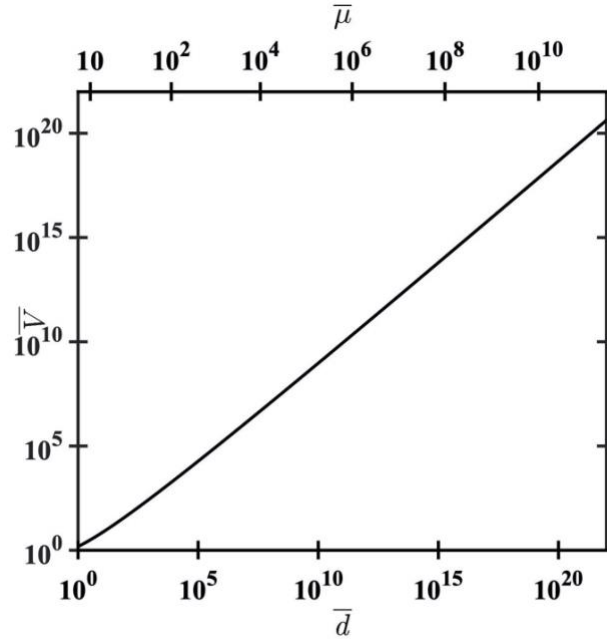
Figure 2.7. Nexus plot summarizing the conditions where the asymptotic solutions for Fowler-Nordheim (FN), Mott-Gurney (MG), and Child-Langmuir (CL), given by (2.18), (2.17), and (2.19), respectively, match. Selecting either $\bar{d}, \bar{\mu}$, or $\bar{V}$ uniquely defines the other two to define this condition from (2.25)-(2.27).

2.4 Conclusion

This study demonstrates the application of an electron emission model for gases generalized to incorporate collisions (Darr *et al*., 2019a) may be applied to experimental results for electron emission in liquids. Since the theory calculates J and the experiments measure I, determining the emission area S_n to convert between these quantities was paramount. While we fixed it here, the electron mobility may in general be a function of electric field and density, so future studies could attempt to more accurately account for this variation, particularly during phase changes.

Even accounting for those limitations, the theory based on electron motion through a gap filled with a material of mobility μ agreed well with liquid emission experimental results, indicating its applicability for both liquids and gases. Increasing and decreasing μ suggested the applicability of this theory for investigating electron emission during a phase change from liquid to gas, which could provide a generalized approach to assess electron emission for applications subject to localized phase changes, such as combustion and plasma treatment of liquids. Since temperature change is an important parameter in inducing the phase change from liquid to vapor, recent theoretical work unifying thermionic emission (TE) with FN, CL, and MG may provide further insight in electron emission mechanism transitions since the necessary temperatures may be sufficient for TE to contribute (Darr *et al*., 2020).

Finally, as mentioned above, one of the critical motivations for this study was ongoing research in applying high voltages to induce plasma formation in liquid. While this study has focused on electron emission physics, other mechanisms are also important, particularly when considering the application of intense, short duration (ns and lower) electric pulses. For instance, one study proposed that subnanosecond pulsed breakdown in liquids could arise because the electrostrictive forces near the cathode create nanopores that could initiate the plasma (Schneider *et al*., 2012). A subsequent study applied the Zeldovich-Fisher theory to determine cavitation-induced pre-breakdown nanopore formation (Schneider and Pekker, 2013). A recent multiphysics simulation of plasma initiation in liquids exposed to nanosecond electric pulses showed that a negative pressure region formed near the high voltage electrode that surpassed the cavitation threshold with electrostrictive ponderomotive forces having a greater effect on cavitation than polarization and electrostatic forces (Aghdam and Farouk, 2020). Future theoretical studies could incorporate the implications of electrostriction, cavitation, temperature effects on phase transition,

and emission (including thermionic and space-charge contribution) to guide device and pulse parameters for plasma discharge generation.

2.5 Data Availability

The data that supports the findings of this study are available within the article.

2.6 Acknowledgements

2.7 Tables

Table 2.1. Electron mobility, solid-angle from fitting nondimensional experimental data, modified Fowler-Nordheim constants by fitting the data using a modified Fowler-Nordheim curve in Fig. 2.2 for the liquids under consideration.

Liquid	μ [m^{2}V^{-1}s^{-1}] (Dotoku *et al.*, 1978)	A'_{FN}[AV^{-2}]	B'_{FN}[V]	A_{FN} [AV^{-2}]	B_{FN} [V/m]
n-Hexane	9×10^{-6}	4.97×10^{-3}	3.81×10^{4}	1.99×10^{-2}	1.905×10^{7}
TMP	5.3×10^{-4}	1.62×10^{-6}	2.31×10^{4}	5.89×10^{-4}	1.155×10^{7}
TMS	9×10^{-3}	1.11×10^{-6}	1.63×10^{4}	1.7×10^{-3}	8.15×10^{6}

Table 2.2. β, notional emission area, S_n, and the formal emission area, S_f, used to find λ_C.

Liquid	β	S_n [m^2]	S_f [m^2]	λ_C
n-Hexane	3.42×10^{3}	1.00×10^{-6}	4.95×10^{-9}	4.95×10^{-3}
TMP	5.65×10^{3}	1.10×10^{-8}	5.94×10^{-13}	5.40×10^{-5}
TMS	8.00×10^{3}	2.67×10^{-9}	2.02×10^{-13}	7.58×10^{-5}

Table 2.3. Scaling parameters defined by (2.13) for three different liquids

Constant [dimensions]	n-Hexane	TMP	TMS
$\phi_0 [V]$	3.49×10^{-8}	3.97×10^{-5}	4.98×10^{-6}
$J_0 [A/m^2]$	7.21×10^{12}	7.86×10^{10}	1.1×10^{11}
$x_0 [m]$	1.83×10^{-15}	3.44×10^{-12}	6.11×10^{-13}
$t_0 [s]$	2.34×10^{-17}	1.3×10^{-15}	6.53×10^{-16}
$\mu_0 [m^2 V^{-1} s^{-1}]$	4.11×10^{-6}	2.29×10^{-4}	1.15×10^{-4}
$E_0 [V/m]$	1.905×10^7	1.155×10^7	8.15×10^6
$v_0 [m/s]$	7.83×10^1	2.64×10^3	9.36×10^2

Table 2.4. Total relative error σ_r comparing the experimental measured data to the exact theoretical solution for the best fit line and R^2 for assessing the correlation of the exact theoretical solution to the experimental data.

Liquid	σ_r	R^2
n-Hexane	0.0306	0.87
TMP	0.0107	0.995
TMS	0.0338	0.928

Table 2.5. Nondimensionalized gap distance $\bar{d}$ and mobility $\bar{\mu}$ for each liquid.

Liquid	$\bar{d}$	$\bar{\mu}$
n-Hexane	1.0931×10^{12}	2.19×10^0
TMP	5.8197×10^8	2.3169×10^0
TMS	3.2723×10^9	7.836×10^1

Table 2.6. Slope and intercept of best-fit lines from the Fowler-Nordheim plots

Liquid	Slope	Intercept
n-Hexane	-3.81×10^4	-5.3
TMP	-2.31×10^4	-13.3
TMS	-1.63×10^4	-13.7

Table 2.7. Experimentally extracted values from the orthodoxy test

Liquid	f_{lower}^{extr}	f_{upper}^{extr}
n-Hexane	0.126	0.146
TMP	0.165	0.198
TMS	0.172	0.224

Table 2.8. Electron mobility for krypton across multiple phases (Allen, 1976; Wada and Freeman, 1979).

	Temperature [K]	Mobility [$m^2V^{-1}s^{-1}$]	Dielectric Constant	Phase
μ_1	113	0.37		solid
μ_2	117	0.18		liquid
μ_3	121.3	0.198	1.678	
μ_4	145.3	0.251	1.612	
μ_5	170.1	0.463	1.535	
μ_6	185.4	0.253	1.473	
μ_7	191.6	0.13	1.444	
μ_8	200.1	0.0357	1.394	
μ_9	205.8	0.00047	1.34	
μ_{10}	300	26.4		Low density gas

Table 2.9. Electron mobility for krypton saturated vapor (Jacobsen et al., 1986).

	Temperature [K]	Mobility [$m^2V^{-1}s^{-1}$]	Dielectric Constant	Phase
μ_{11}	151.5	0.0198	1.012	vapor
μ_{12}	156	0.0156	1.015	vapor
μ_{13}	162	0.0111	1.019	vapor
μ_{14}	165.9	0.0101	1.023	vapor
μ_{15}	175.8	0.0055	1.058	vapor
μ_{16}	190	0.0025	1.058	vapor
μ_{17}	206.3	0.00048	1.131	vapor

3. INCORPORATING PHOTOEMISSION INTO THE UNIFICATION MODEL OF FIELD EMISSION, THERMIONIC EMISSION, AND SPACE-CHARGE-LIMITED EMISSION

3.1 Introduction

Because of the profound effect electron emission has on numerous industries and applications, the characterization of electron emission in gases has been heavily research and developed for conditions ranging from vacuum to atmospheric (Akimov and Schamel, 2002; Bhattacharjee *et al.*, 2008; Bhattacharjee and Chowdhury, 2009; Darr *et al.*, 2019a; Dynako *et al.*, 2019; Feng and Verboncoeur, 2006; Ingold, 1969a; Ingold, 1969b; Lau *et al.*, 1994; Luginsland *et al.*, 1996). Electron emission has important implications in vacuum electronics (Brayfield et al., 2019; Brodie and Schwoebel, 1994; Fu *et al.*, 2020; Garner *et al.*, 2020b; Go and Venkattraman, 2014; Jensen, 2018; Johnson and Oskam, 1971; Zhang *et al.*, 2017), lasers (Brau, 1998; Jensen *et al.*, 2006a; Jensen *et al.*, 2006b; O'Shea and Freund, 2001; O'Shea, 1998; O'Shea *et al.*, 1993), and particle accelerators (Birdsall and Bridges, 1966; Dowell *et al.*, 1993; Fraser and Sheffield, 1987; Humphries, 1990; Michelato, 1997; Reiser, 1994); these are only a few of the numerous fields that are affected by electron emission. For these applications, understanding the transitions between the different mechanisms and the regions where each mechanism dominates is important for designing products that need to function at certain operating conditions such as pressure or temperature. Due to the influence of the electron emission mechanisms, there are numerous studies analyzing and characterizing the different theories that model field emission (FE), space-charge limited (SCL) emission, thermionic or thermal emission (TE), secondary emission, and photoemission (PE).

Many research studies focus on characterizing one emission mechanism or the connection to other electronic processes and emission mechanisms. Research studies often focus on the connection between electron emission and electronic breakdown because of the potential implications electronic breakdown has for plasma (Foster, 2017; Xu *et al.*, 2017) and pulsed power fields (Garner *et al.*, 2017; Schoenbach *et al.*, 2008; Zahn *et al.*, 1986). Electron emission is considered one of the initial phases of electronic breakdown (Loveless and Garner, 2016; Loveless *et al.*, 2019; Venkattraman and Alexeenko, 2012); FE is considered one of the primary electron emission mechanisms that initiates breakdown at the cathode (Auger *et al.*, 2016; Phan *et al.*, 2020;

Qian *et al*., 2005). These studies regarding the connection between breakdown and electron emission focus on the initiation of breakdown through electron emission and how it transitions to Townsend breakdown (TB) and Paschen's Law (PL) (Loveless and Garner, 2017b; Loveless and Garner, 2016; Loveless and Garner, 2017a; Loveless and Garner, 2017c; Loveless *et al*., 2019; Paschen, 1889). Although FE is considered one of the primary electron emission mechanisms that contributes to breakdown, some studies focus on the transition from TE to breakdown (Haase and Go, 2016; Lee *et al*., 2017a; Lee *et al*., 2017b; Venkattraman, 2014) and others focus on the effects of SCL (Go and Pohlman, 2010).

Extensive research has been conducted for each individual electron emission mechanism resulting in numerous equations and models used for these emission mechanisms; these equations and models describe the regions and conditions for which each emission mechanism dominates. FE occurs when electrons are released from the cathode due to an increase in voltage, and this is often modeled by Fowler-Nordheim (FN) equation (Fowler and Nordheim, 1928; Lau *et al*., 1994; Murphy and Good, 1956). FE transitions to SCL when the charge buildup in the gap is strong enough to prevent electron emission; this is predicted by Child-Langmuir at vacuum (Child, 1911; Langmuir, 1913; Lau *et al*., 1994). When the conditions are not vacuum, collisions may cause the transition to SCL which is modeled by the Mott-Gurney (MG) law which is dependent on the electron mobility (Darr *et al*., 2019a; Murphy and Good, 1956). As the temperature increases at the surface of the cathode electrons are released, which is TE (Jensen, 2017); this is often modeled using the Richardson-Laue-Dushmann (RLD) equation (Dushman, 1923; Dushman, 1930; Richardson and Burndy, 1916; Richardson and Young, 1925), which describes a T^2 dependence for the current density. To account for effects of adding a series resistor, Ohm's law (OL) can be included (Dynako *et al*., 2019). PE is another heavily researched electron emission mechanism which is usually researched with TE. PE occurs due to incident light hitting the surface which causes electrons to be released (Jensen, 2017); this emission is often modeled using the modified Fowler-Dubridge (MFD) equation (DuBridge, 1932; DuBridge and Roehr, 1932; DuBridge, 1933; Fowler, 1931; Jensen, 2017; Jensen, 2018). These are only a few of the equations and models used to describe emission mechanisms; research has continued to build upon and improve the initial models for these emission mechanisms.

Within the past thirty years, interest in unifying these different electron emission mechanisms has become more prominent. Much of this unification began with connecting two

emission mechanisms at a time such as connecting FE to SCLE (Chen *et al.*, 2009; Feng and Verboncoeur, 2006; Forbes, 2008; Lau *et al.*, 1994; Rokhlenko *et al.*, 2010) or FE to TE (Benilov and Benilova, 2013; Chen *et al.*, 2009; Crowell, 1969; He *et al.*, 2008; Jensen and Cahay, 2006; Jensen *et al.*, 2019; Segev *et al.*, 2013). Other studies have connected TE to SCLE (Jensen *et al.*, 2019; Liu *et al.*, 2011; Wang *et al.*, 2006) or TE to PE (Segev *et al.*, 2013). More recently the focus of the research has expanded into connecting more than two emission mechanisms starting with connecting FE, TE, and PE (Jensen *et al.*, 2002; Jensen, 2007; Jensen *et al.*, 2019). Another study connected FE, SCLE, and SCLE with collisions using nexus theory (Darr *et al.*, 2019a). One of the most recent studies connected FN, CL, MG, TE, and even included OL (Darr *et al.*, 2020); this research connected almost all of the primary emission mechanisms except for PE. The goal of this research will be to extend the model the connects FN, CL, TE, MG, and OL to include PE for gases.

PE has been extensively researched and modeled individually and connected with other emission mechanisms; however, the majority of these connections have been between only two mechanisms. One model that connects a few of the emission mechanisms is the general thermal field (GTF) equation; this equation models the transition between FE and TE using a general analytic model (Jensen *et al.*, 2002; Jensen and Cahay, 2006; Jensen, 2007; Jensen *et al.*, 2019). The GTF equation was adjusted to account for PE; this became the general thermal-field photo (GTFP) equation (Jensen, 2007). The GTFP equation describes the general currents for FE, TE, and PE and the conditions at which the current density can be modeled by FN for (FE), RLD for (TE), and MFD (for PE) (Jensen, 2018). Darr used the GTF and RLD equations to connect TE with the nexus theory previously used to connect other semi-empirical models, FN, RLD, GTF, and MG, and full analytic models, CL and OL, to look at the transitions between the different mechanisms (Darr *et al.*, 2020). He used the asymptotic nexus theory to determine at which parameters the various theories could be used to model the current density. However, Darr did not include PE in this emission model. Using the semi-empirical MFD equation and GTFP equation, we will attempt to incorporate PE into the current nexus model.

Section 3.2 reviews the model derivation for this paper which includes reviewing basic electron emission theory and the nondimensionalization of the parameters; the basic electron emission theory is centered around reviewing the PE and how it connects to the other mechanisms. The nondimensionalization is centered around making the theory universal and determining the

asymptotic relationships. Section 3.3 analyzes the model at different conditions to determine at which points the theories are most dominate. Section 3.4 concludes the paper.

3.2 Theory

3.2.1 Basic electron emission theory, GTF

The basis of this research begins with Jensen's work from the early 2000s (Jensen, 2007); we follow the same steps with a slight deviation. Similar to the previous studies regarding the unification of electron emission mechanisms (Darr *et al.*, 2019; Darr *et al.*, 2020), we make similar assumptions regarding the coefficients. However, we are not including electron mobility, external series resistance, or a friction term for the initial derivation of the model. In this paper, Φ is the work function, S is the emission area, and the Fowler-Nordheim (FN) constants are $A_{FN} = e^3/(16\pi^2\hbar\Phi)$ and $B_{FN} = (4\sqrt{2m\Phi^3})/(3\hbar e)$ (Jensen *et al.*, 2007) . The initial derivation begins with Poisson's equation,

$$\frac{d^2\phi}{dx^2} = \frac{\rho}{\varepsilon_0},$$ (3.1)

and the energy balance equation,

$$\frac{1}{2}mv^2 = e\phi + \frac{1}{2}mv_i^2.$$ (3.2)

In these equations, ρ is the charge density, ε_0 permittivity of free space, m is the electron mass, v_i is the initial electron velocity, and e is the elementary electron charge which is often symbolized as q for research regarding PE; we will be using e to be consistent with the previous unification research. The velocity is assumed to be the average velocity from the Maxwell-Boltzmann distribution. The continuity equation is another equation used to derive this model,

$$J = \rho v,$$ (3.3)

where J is the current density. The current density will be initially defined using the GTF equation,

$$J_{GTF}(F,T) = A_{RLD}T^2 N(n,s).$$ (3.4)

In the GTF equation, A_{RLD} is equal to $(emk_b^2)/(2\pi^2\hbar^3)$ which includes Boltzmann's constant, k_b and the reduced Planck's constant, $\hbar$ (Jensen, 2017). In this equation, $n \equiv \beta_T/\beta_F$ which is the slope factor ratio and $\beta_T = 1/(k_bT)$ (Jensen, 2007); β_F , s , and $N(n,s)$ provide the most complications for this unification research. The GTF equation defines the transitions between FE and TE. To adjust the model to incorporate PE, the conditions need to be adjusted to model PE as

well. The next section focuses on incorporating PE into the current model and the complications that follow.

3.2.2 Modeling photoemission

Before adding PE to the model, we need to address the individual model for PE. In general, the Fowler-DuBridge (FD) equation is used to model PE; since this equation was first developed, there have been a few adjustments and corrections (DuBridge, 1932; DuBridge and Roehr, 1932; DuBridge, 1933; Fowler, 1931; Jensen *et al*., 2008; Jensen, 2017; Jensen, 2018). This corrected model is known as the modified FD (MFD) (Jensen *et al*., 2008), and this is the equation that will be important to this research. The MFD equation,

$$J_{MFD}(F,T) = \left(\frac{e}{\hbar\omega}\right)[1 - R(\theta)]F_\lambda I_\lambda P_{MFD}(\hbar\omega,T), \tag{3.5}$$

accounts for the scattering, F_λ, the reflectivity with incident angle θ, $R(\theta)$, illumination (laser) intensity, I_λ, and the emission probability, $P_{MFD}(\hbar\omega,T)$ (Jensen *et al*., 2008; Jensen, 2017; Jensen, 2018); this equation is typically evaluated with photon energy, $\hbar\omega$. The photon energy is determined by reduced Planck's constant, $\hbar$, and the angular frequency, ω, defined by

$$\omega = 2\pi c/\lambda, \tag{3.6}$$

where c is the speed of light and λ is the laser wavelength (Jensen, 2017); as the laser properties change, the photon energy will change. Because of this change, there are benefits to looking at different materials for this analysis. The part of equation (3.5) that is different from the original FD equation is the modified emission probability, $P_{MFD}(\hbar\omega,T)$,

$$P_{MFD}(\hbar\omega,T) = \frac{(\hbar\omega - \phi)^2 + 2\beta_T^{-2}\zeta(2)(1+n^2)}{2\hbar\omega(2\mu_F - \hbar\omega)}. \tag{3.7}$$

This probability depends on the number of electrons with energy above the barrier and the total number of incident electrons on the barrier (Jensen, 2017). $P_{MFD}(\hbar\omega,T)$ accounts for the Schottky barrier by replacing the work function with $\varphi = \Phi - \sqrt{4QF}$ where Q is approximately 0.36 *eV nm*, and F is a force (Jensen *et al*., 2007; Jensen, 2018). In (3.7), n and β_T are previously defined and $\zeta(2)$ is the Riemann zeta function which is equal to $\pi^2/6$ (Jensen *et al*., 2007). The term in brackets in the denominator of (3.7) ensures that the denominator is not zero, but it still can be compared to φ (Jensen *et al*., 2007).

The other terms in (3.5) can influence the current density as well. However, I_λ is the most influential out of $[1 - R(\theta)]$ and F_λ. The laser intensity, I_λ, is dependent on time, which is often described by a Gaussian distribution

$$I_\lambda(t) = I_i \exp(-[(t)/\Delta t]^2) \tag{3.8}$$

where I_i is the initial laser intensity in units of Wm^{-2} (Jensen *et al.*, 2003; Jensen *et al.*, 2005; Jensen *et al.*, 2006a); because this solution does not depend on time for this research, we assume that $I_\lambda(0) = I_i$. For this initial laser intensity, which we will denote as I_i, we are going to choose a few different values to see the effect on the fit (Jensen *et al.*, 2003; Jensen *et al.*, 2005; Jensen *et al.*, 2006a). Now similar to the laser intensity, reflectivity, $R(\theta)$, also has a dependence; however, this dependence is on the incident angle, θ, and the laser wavelength, λ (Forati and Sievenpiper, 2018). Similar to $R(\theta)$, the scattering factor, F_λ, depends on variables such as the incident angle; however, this is calculated using a different analytical approach (Forati and Sievenpiper, 2018). Due to the complexity of $R(\theta)$ and F_λ, they will be treated as constants for this analysis. To test the effects of I_i, $R(\theta)$, and F_λ on the current density, we will run code for different variations of these values. To simplify the equation for analysis we defined the constant I_{eff} to account for the effective laser properties,

$$I_{eff} = I_i[1 - R(\theta)]F_\lambda, \tag{3.9}$$

which has units of Wm^{-2}. The quantum efficiency, QE, for the MFD is

$$QE_{MFD}(\hbar\omega, T) = [1 - R(\theta)]F_\lambda P_{MFD}(\hbar\omega, T). \tag{3.10}$$

$QE_{MFD}(\hbar\omega, T)$ is often used to simplify the current density equations, and it is proportional to $(\hbar\omega - \Phi)^2$ (Jensen, 2018). The basics of the MFD equation can be incorporated into the GTF equation to model PE in connection with TE and FE.

3.2.3   Incorporating photoemission

Now the FD equation can be generalized, just as FN and RLD were, to be included in the general thermal-field photoemission (GTFP) equation. The GTFP is just defined as the total electron emission which is the current density from PE added to the current density from GTF,

$$J_{GTFP}(F, T) = J_p(F, T) + J_{GTF}(F, T), \tag{3.11}$$

where $J_p(F, T)$ is the generalized PE equation (Jensen *et al.*, 2008; Jensen, 2018),

$$J_p(F, T) = \frac{e}{\hbar\omega} QE_{MFD}(\hbar\omega, T)I_i. \tag{3.12}$$

Now the equation for general PE is

$$J_p(F,T) = \frac{e}{\hbar\omega} I_{eff} P_{MFD}(\hbar\omega, T) \tag{3.13}$$

where $e/\hbar\omega$ which has units of C/J.

The challenge for the evaluation of (3.11) is determining the conditions at which PE occurs. In (3.4), $N(n,s)$ is used to account for the different regions where FE and TE occur, and

$$N(n,s) = n \int_{-\infty}^{\infty} \frac{\ln\left[1 + e^{n(x-s)}\right]}{1 + e^x} dx \tag{3.14}$$

where *n* and *s*, defined above, are the factors that determine the region of emission. The extension to PE for the GTFP equation occurs when $N(n,s)$ goes to $N(n,-s)$ (Jensen *et al.*, 2008; Jensen, 2012; Jensen *et al.*, 2014; Jensen, 2018; Jensen, 2019; Jensen *et al.*, 2019). $N(n,-s)$ is

$$N(n,-s,u) = n \int_{-\infty}^{u} \frac{\ln\left[1 + e^{n(x+s)}\right]}{1 + e^x} dx, \tag{3.15}$$

where $u = \beta_F(E_m)(\mu_F + \varphi - \hbar\omega)$, $s = \beta_F(E_m)(\hbar\omega - \varphi)$, and $ns = \beta_T(\hbar\omega - \varphi)$ for PE (Jensen, 2007); for this particular equation, $E_m = \mu_F + \varphi$ as long as the emission is below the barrier energy (Jensen, 2007; Jensen *et al.*, 2014). Jensen redefined the GTFP as

$$J_{GTFP}(F,T) \equiv A_{RLD} T^2 N(n,s) \tag{3.16}$$

where

$$N(n,s) \approx \frac{1}{2} n^2 s^2 + \zeta(2)(n^2 + 1) - N(n,-s). \tag{3.17}$$

For this analysis, we use (3.11) to analyze the model.

Although we have the equations necessary for the model fit, we need to determine the conditions for the PE regions to develop the asymptotic fit. When transitioning to PE, the energy incorporates $\hbar\omega$ (Jensen, 2007; Jensen *et al.*, 2014; Jensen, 2018). The emission regimes are specified using β_T, β_F, n and s. When n goes to infinity ($n \to \infty$), the field current density goes to FN ($J_F \to J_{FN}$), and when n goes to zero ($n \to 0$), the thermal current density goes to FN ($J_T \to J_{RLD}$) (Jensen *et al.*, 2008; Jensen, 2018; Jensen *et al.*, 2019). Finally, when n^2 goes to zero ($n^2 \to 0$), the current density goes to FD ($J_P \to J_{FD}$) (Jensen *et al.*, 2008; Jensen, 2018; Jensen *et al.*, 2019); this means that β_T is large. So, when $n^2 \to 0$, the second half of (3.11) will go to zero leaving J_P.

3.3　Model derivation

3.3.1　Nondimensionalization

To nondimensionalize the solutions, we define (Darr *et al.*, 2020)

$$\phi = \phi_0\bar{\phi}; J = J_0\bar{J}\,; x = x_0\bar{x}; t = t_0\bar{t}; \mu =, \mu_0\bar{\mu}; E = E_0\bar{E}; v = v_0\bar{v}; F = F_0\bar{F}; \tag{3.18}$$

$$T = T_0\bar{T}; R = R_0\bar{R}; I_i = I_0\bar{I}_i; \hbar\omega = \hbar\omega_0\overline{\hbar\omega},$$

where

$$E_0 = B_{FN}\left[\frac{V}{m}\right]; J_0 = A_{FN}E_0^2\left[\frac{A}{V^2}\right]; x_0 = \frac{eE_0t_0^2}{m}\ [m]; T_0 = \frac{\Phi}{k_B}[K]; F_0 = eE_0\left[\frac{eV}{m}\right]; v_0 = \frac{x_0}{t_0}\left[\frac{m}{s}\right] \tag{3.19}$$

$$t_0 = \frac{\epsilon_0E_0}{J_0}\ [s]; \mu_0 = \frac{e\epsilon_0}{mA_{FN}B_{FN}}\left[\frac{m^2}{Vs}\right]; \phi_0 = E_0x_0\ [V]; R_0 = \frac{\phi_0}{J_0S}\ [\Omega]\ ;$$

$$I_0 = \frac{m\omega\Phi^2}{\hbar^2}\left[\frac{W}{m^2}\right]; \hbar\omega_0 = eE_0x_0[J]\ .$$

These scaling factors (3.19) are the same as defined by Darr *et al.* (2020) with the addition of I_0, which account for the laser properties, and $\hbar\omega_0$, which accounts for the photon energy, in the PE equations. In general, the PE equations used in this analysis are very material dependent. Note that the scaling factor μ_0 is for the electron mobility μ, and not the Fermi energy level μ_F. Also, for these scaling factors, ϕ, is the potential.

To nondimensionalize the FD and MFD equations, the original equations are divided by the scaling constant J_0. The resulting nondimensionalized equations are

$$\bar{J}_{FD} = \frac{9}{2}\pi^2\bar{I}_{eff}P_{FD}(\hbar\omega) \tag{3.20}$$

for FD and

$$\bar{J}_{MFD} = \frac{9}{4}\pi^2\bar{I}_{eff}P_{MFD}(\hbar\omega) \tag{3.21}$$

for MFD. Now the terms $P_{FD}(\hbar\omega)$ and $P_{MFD}(\hbar\omega)$ are unitless terms. $\bar{I}_{eff}$ is the term that defines the nondimensionalized laser properties. Equations (3.20) and (3.21) are used to find the asymptotic limits in the following sections. Now using these scaling factors and the background information, we can proceed to the main analysis sections of this research.

3.3.2　Asymptotic nexus and resulting limits

The asymptotic limits for FN and RLD from (Darr *et al.*, 2020) are

$$\bar{J}_{FN} = \bar{E}^2 e^{-1/\bar{E}} = \left(\frac{\bar{V}}{\bar{D}}\right)^2 e^{-\bar{D}/\bar{V}}, \tag{3.22}$$

and

$$\bar{J}_{RLD} = \frac{9}{4}\bar{T}^2 e^{-1/\bar{T}} \tag{3.23}$$

which were determined using the limits of the $\bar{J}_{GTF}$ equation. Darr *et al.* (2020) also defined

$$\bar{J}_{CL} = \frac{4\sqrt{2}\bar{V}^{\frac{3}{2}}}{9\bar{D}^2}, \tag{3.24}$$

and a generalized CL (GCL) equations (Darr *et al.*, 2020),

$$\bar{J}_{GCL} = \bar{J}_{CL}\left[(\bar{v}_i^2/(2\bar{V}))^{1/2} + (1 + \bar{v}_i^2/(2\bar{V}))^{1/2}\right]^3 \approx \bar{J}_{CL}\left(1 + 3(\bar{v}_i^2/(2\bar{V}))^{1/2}\right). \tag{3.25}$$

For this analysis, the GCL equation is used for most of the figure results. The last two asymptotic limits that Darr *et al.* defined were the MG equation,

$$\bar{J}_{MG} = \frac{9\bar{\mu}\bar{V}^2}{8\bar{D}^3}, \tag{3.26}$$

and the OL equation,

$$\bar{J}_{OL} = \frac{\bar{V}}{\bar{R}}, \tag{3.27}$$

where $\bar{R}$ is the nondimensionalized resistance (Darr *et al.*, 2020). These asymptotic equations (3.22)-(3.27) were found using initial conditions for T, E, and v_i. After determining these limits, Darr *et al.* found the second order nexus points by setting the limits equal to each other (Darr *et al.*, 2020); these second order nexus points can then be equated to determine a higher order nexus point. The third order nexus point between RLD-FN-CL is

$$\frac{1}{\bar{T}_N} = \frac{1}{\bar{E}_N} = \frac{\bar{D}_N}{\bar{V}_N} = \ln\left(\frac{9\sqrt{\bar{V}_N}}{4\sqrt{2}}\right) \tag{3.28}$$

where $1/\bar{T}_N = 1/\bar{E}_N$ is the nexus for RLD and FN, $\bar{D}_N/\bar{V}_N = \ln\left(9\sqrt{\bar{V}_N}/4\sqrt{2}\right)$ is the nexus for FN and CL. Note that for this analysis $E = V/D$ which is the voltage divided by the gap distance; this is primary used when modeling CL or parallel plates. The addition of MG and OL results in the fifth order nexus

$$\frac{1}{\bar{T}_N} = \frac{1}{\bar{E}_N} = \frac{\bar{D}_N}{\bar{V}_N} = \ln\left(\frac{9\sqrt{\bar{V}_N}}{4\sqrt{2}}\right) = \frac{81\bar{\mu}_N}{32\sqrt{2\bar{V}_N}} = \exp\left(-\frac{\bar{D}_N}{2\bar{V}_N}\right)\sqrt{\frac{\bar{R}_N}{\bar{V}_N}}, \tag{3.29}$$

where the last two terms account for MG and OL. The goal is to determine the asymptotic limits for FD and MFD and add the terms to the nexus equation (3.29).

To determine the asymptotic limits for FD and MFD, we evaluate them at the zero temperature and zero field. Because these equations are heavily reliant on the material properties, there will be some unitless constants in these asymptotic limits. Beginning with FD, we have

$$J_{FD}(F,T) = \left(\frac{q}{\hbar\omega}\right)I_{eff} \tag{3.30}$$

for $F = 0$ and $T = 0$ which can be nondimensionalized to get

$$\bar{J}_{FD} = \frac{9}{2}\pi^2\bar{I}_{eff}. \tag{3.31}$$

The asymptotic limit for the MFD equation is more complicated due to the number of unitless material constants in the equations. When $F = 0$ and $T = 0$, $J_{MFD}(F,T)$ reduces to

$$J_{MFD}(F,T) = \left(\frac{q}{\hbar\omega}\right)I_{eff}\frac{(\hbar\omega - \Phi)^2}{2\hbar\omega(2\mu_F - \hbar\omega)} \tag{3.32}$$

which can be nondimensionalized to get

$$\bar{J}_{MFD} = \frac{9}{4}\pi^2\bar{I}_{eff}\left[\frac{(\hbar\omega - \Phi)^2}{\hbar\omega(2\mu_F - \hbar\omega)}\right] \tag{3.33}$$

where the term in brackets is a unitless constant determined by the cathode material properties; this unitless constant will be denoted as χ. The equation can now be written as

$$\bar{J}_{MFD} = \frac{9}{4}\pi^2\bar{I}_{eff}[\chi] \tag{3.34}$$

Using the FD asymptotic limit (3.31) and the MFD asymptotic limit (3.34), we can determine an approximate nexus point. To accomplish this, we can set the equations equal to (3.22). From equating (3.31) to (3.22), we get

$$\frac{\bar{D}_N}{\bar{V}_N} = \frac{1}{3\pi}\sqrt{\frac{2}{\bar{I}_{eff}}}\exp\left(-\frac{\bar{D}_N}{2\bar{V}_N}\right) \tag{3.35}$$

which is the transition between FN and FD. The transition between FN (3.22) and MFD (3.34) is

$$\frac{\bar{D}_N}{\bar{V}_N} = \frac{2}{3\pi}\sqrt{\frac{1}{\bar{I}_{eff}\chi}}\exp\left(-\frac{\bar{D}_N}{2\bar{V}_N}\right). \tag{3.36}$$

Using equations (3.34) and (3.36), we can write the nexus point to include PE modeled by MFD,

$$\frac{1}{\bar{T}_N} = \frac{1}{\bar{E}_N} = \frac{\bar{D}_N}{\bar{V}_N} = \ln\left(\frac{9\sqrt{\bar{V}_N}}{4\sqrt{2}}\right) = \frac{81\bar{\mu}_N}{32\sqrt{2\bar{V}_N}} = \exp\left(-\frac{\bar{D}_N}{2\bar{V}_N}\right)\sqrt{\frac{\bar{R}_N}{\bar{V}_N}} = \frac{2}{3\pi}\sqrt{\frac{1}{\bar{I}_{eff}\chi}}\exp\left(-\frac{\bar{D}_N}{2\bar{V}_N}\right). (3.37)$$

Using these nexus relationships, we can model the transitions between the different electron emission mechanisms. However, these transition plots or phase plots depend on the parameters being analyzed. One should note that (3.37) requires information regarding the cathode and initial laser properties. For this research analysis, these properties will be considered to be constant, but future studies could incorporate the dependence of these properties.

3.4 Results

The cathode material properties are the fermi energy level, μ_F and the work function, Φ; many studies chose copper (Cu), tungsten (W), or gold (Au), but for this initial study we chose Cu. Table 3.1 lists the common values for μ_F and Φ for Cu, W, and Au.

Table 3.1. Cathode properties (Jensen *et al.*, 2003; Jensen *et al.*, 2007)

Liquid	Cu	W	Au
μ_F [eV]	7	18.08	5.51
Φ [eV]	4.5	4.6	4.69

Due to the addition of PE, we need to account for the laser properties, including I_i, F_λ, $R(\theta)$, and λ, where I_i and λ depend on the type of laser being used. We are using properties associated with Mega Watt Free Electron Lasers (MW FEL) which can have I_i ranging from $1\ MWcm^{-2}$ to $160\ MWcm^{-2}$ and λ ranging from 266 *nm* to above 1064 *nm* (Jensen *et al.*, 2008; Moody *et al.*, 2007); longer wavelengths are ideal for lasers because it leads to a higher QE (Jensen *et al.*, 2006). These properties depend on the type of experiment being conducted. F_λ and $R(\theta)$ are held constant for this research due to the complexity of the constants; the values for scattering range from around 0.01 to 1, and the values for the reflectivity range from around 0 to 0.99. For the general analysis, we will assume a Cu cathode with a laser intensity of 32 $MWcm^{-2}$ (Jensen *et al.*, 2005), a laser wavelength of 266 *nm*, and a scattering and reflectivity of 0.5. However, we will examine what happens if we were to vary the intensity, the wavelength, the scattering, and the reflectivity.

Figures 3.1(a)-3.1(d) show the transitions between the different emission mechanisms for

nondimensional current density as a function of voltage $\bar{J} = \bar{J}(\bar{V})$ for a Cu cathode with a fixed gap distance $D = 1\ nm$ and $\lambda = 266\ nm$, $I_i = 3.2 \times 10^{11}\ Wm^{-2}$, and $F_\lambda = R(\theta) = 0.5$ as the initial laser properties. Each of the figures differ with a fixed temperature to demonstrate the affect the temperature has on the different mechanisms where the nexus temperature is $T_N = 2750\ K$ ($\bar{T}_N = 0.0527$); the temperatures are as follows for figure 3.1, (a) 82.5 K ($0.03\bar{T}_N$), (b) 2062.5 K ($0.75\bar{T}_N$), (c) 2750 K ($\bar{T}_N$), and (d) 4125 K ($1.5\bar{T}_N$). These figures include the transitions between GTFP, MFD, FN, GCL, and RLD. Each of these temperatures provides information about potential operating temperatures for experiments and electronic devices. With the lower temperature, (a) 82.5 K ($0.03\bar{T}_N$), RLD does not interact with the other asymptotic limits. As the temperature increases RLD has a closer transition with the other asymptotic limits; RLD transitions between GCL, GTFP, and FN at a higher current density. While MFD, RLD, GTFP, and FN connect at a nexus point. This is expected due to the conditions under which GCL occurs.

Figure 3.1. Dimensionless current density $\bar{J}$ as a function of the nondimensional voltage $\bar{V}$ for the full solution (GTFP) and asymptotic limits for GCL (blue), FN (black), RLD (green), and MFD (magenta) for different variations of the nexus temperature (a) 82.5 K ($0.03\bar{T}_N$), (b) 2062.5 K ($0.75\bar{T}_N$), (c) 2750 K ($\bar{T}_N$), and (d) 4125 K ($1.5\bar{T}_N$) for a nexus temperature of $T_N = 2750\ K$ ($\bar{T}_N = 0.0527$). The third order nexus between MFD, FN, and RLD can be seen at the nondimensionalized temperature. These plots are for a Cu cathode with $D = 1\ nm$, $\hbar\omega = 4.66\ eV$, $F_\lambda = R(\theta) = 0.5$, $\lambda = 266\ nm$, and $I_i = 3.2 \times 10^{11}\ Wm^{-2}$.

Figure 3.2.continued.
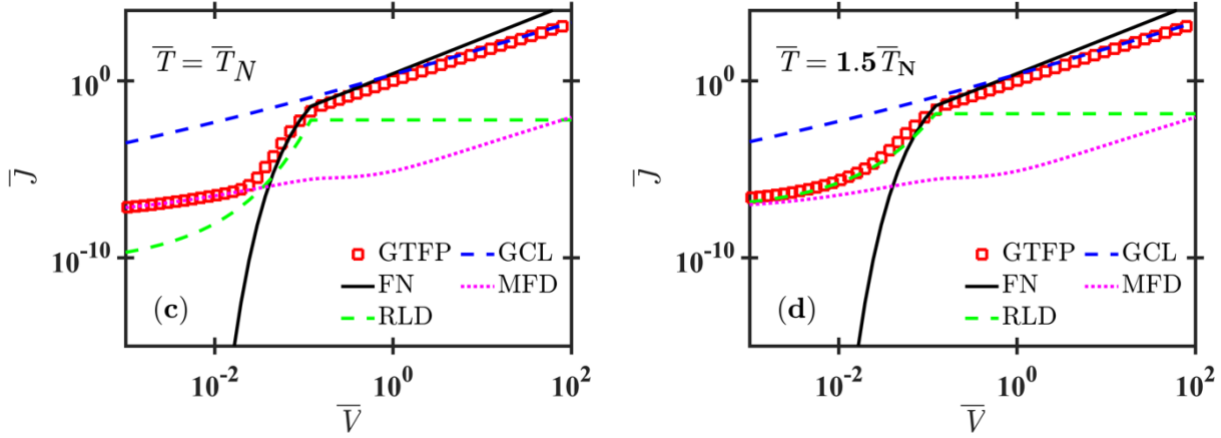
In general, the operating temperature for the original FD model is around 300 *K*, room temperature, with a field around 10 $eV/\mu m$ and a wavelength of 266 *nm* (Jensen, 2017); this operating temperature would be best reflected in between 3.1(a) and 3.1(b). For this specific temperature, there does not appear to be a transition point between MFD and RLD; this is most likely because of the temperature dependence of RLD. As the temperature increases, this transition between MFD and RLD is more apparent.

Because W is often used as a cathode material, we constructed the same plots in figure 3.1 using W properties instead of Cu values and could not discern a difference. I chose not to include these figures due to lack of space and difference from the plots in figure 3.1.

The wavelength determines the photon energy that is a fundamental parameter for PE; as the wavelength increases the QE increases and the photon energy decreases. To demonstrate the effects of the laser wavelength and changing temperature, we changed the wavelength from 266 *nm* to 1064 *nm* and plotted the nondimensional current density as a function of voltage $\bar{J} = \bar{J}(\bar{V})$ for a Cu cathode with a fixed gap distance $D = 1\ nm$ and $I_i = 3.2 \times 10^{11}\ Wm^{-2}$ and $F_\lambda = R(\theta) = 0.5$ as the initial laser properties; these are the same properties as figure 3.1 with exception of λ. Figure 3.2 demonstrates the effects of increasing the λ while increasing the temperature. Adjusting λ, changes the overall shape of the GTFP equation left of the FN equation. Instead of a steady increase from the PE region of the GTFP (left), there is a slight decrease before it begins to follow the FN equation. This results in a slightly higher nexus point than with a wavelength of 266 *nm*.
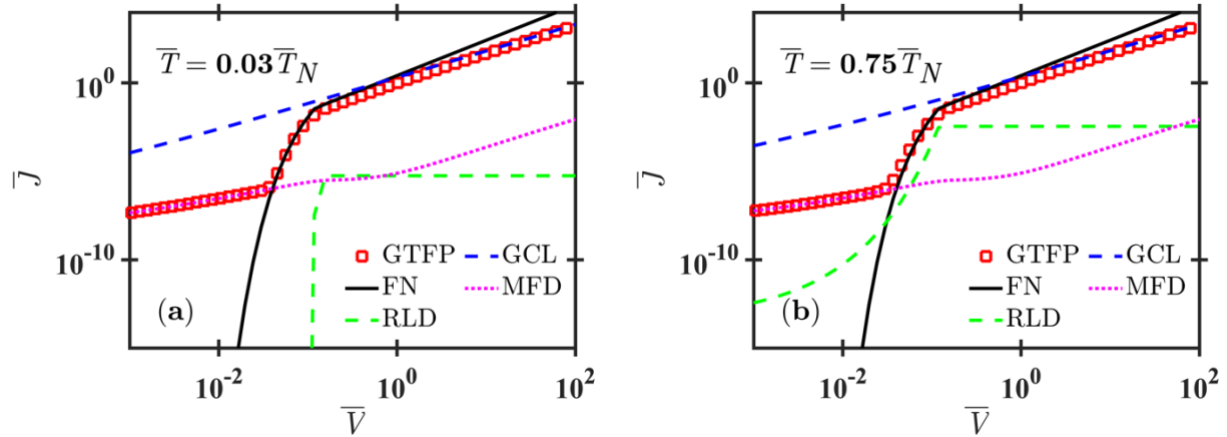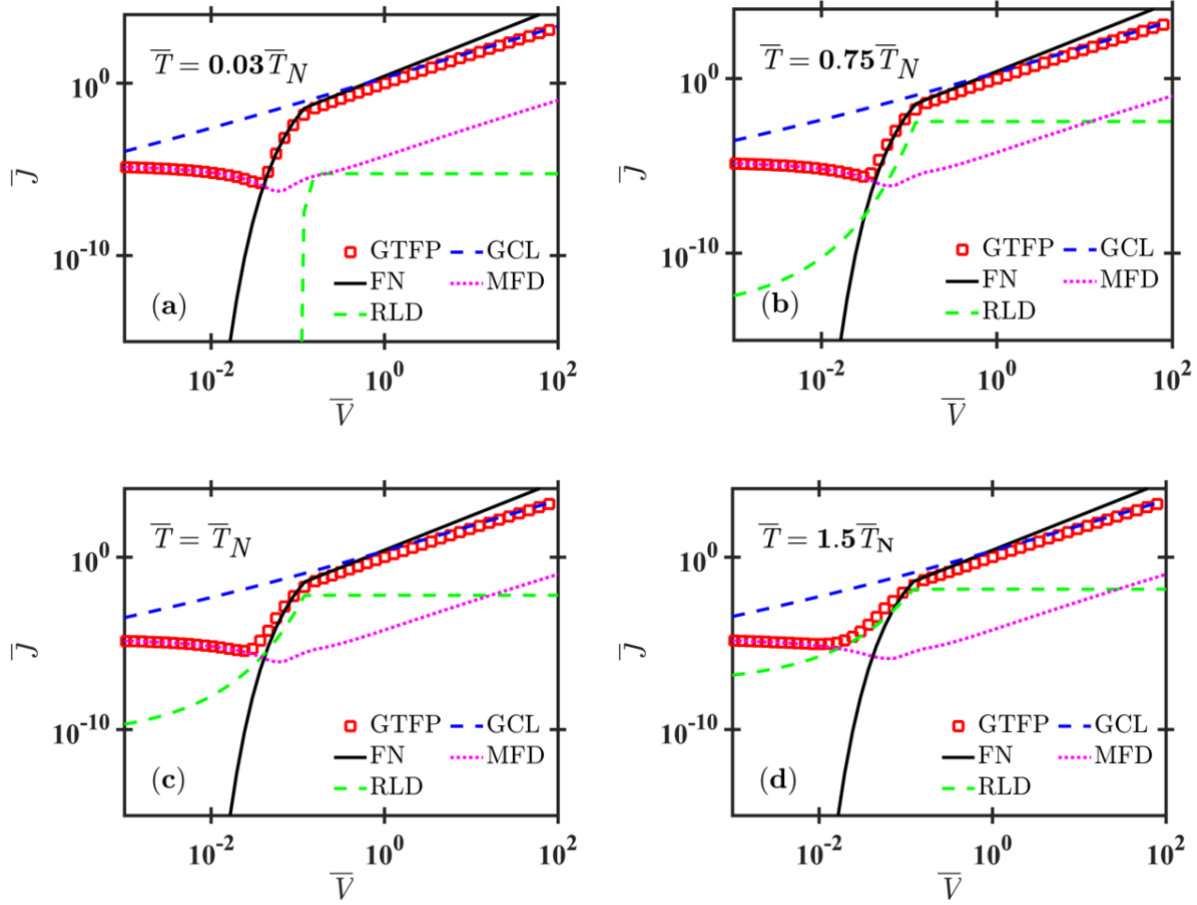
Figure 3.3. Dimensionless current density $\bar{J}$ as a function of the nondimensional voltage $\bar{V}$ for the full solution (GTFP) and asymptotic limits for GCL (blue), FN (black), RLD (green), and MFD (magenta) for different variations of the temperature (a) 82.5 K ($0.03\bar{T}_N$), (b) 2062.5 K ($0.75\bar{T}_N$), (c) 2750 K ($\bar{T}_N$), and (d) 4125 K ($1.5\bar{T}_N$) for a nexus temperature of $T_N = 2750\ K$ ($\bar{T}_N = 0.0527$). The third order nexus between MFD, FN, and RLD can be seen at the nondimensionalized temperature. These plots are for a Cu cathode with $D = 1\ nm$, $\hbar\omega = 1.17\ eV$, $F_\lambda = R(\theta) = 0.5$, $\lambda = 1064\ nm$, and $I_i = 3.2 \times 10^{11}\ Wm^{-2}$.

The wavelengths for lasers vary depending on the class of laser. To show the effects of varying λ for a constant nexus temperature of 2750 K, we plotted seven different wavelengths which are listed in table 3.2. We nondimensionalized the wavelength using $x_0 = 1.8 \times 10^{-9}\ m$ which is the same scaling constant used to nondimensionalize the gap distance.

Table 3.2. Laser wavelength

	$\lambda\,[nm]$	$\bar{\lambda}$
1	90	50
2	266	148
3	375	208
4	405	225
5	532	295
6	655	363
7	808	448
8	1064	590

The major differences for the wavelengths appear to be how the GTFP and MFD behave at lower voltages and where they interact with the FN equation. For the smallest wavelength, the GTFP and MFD appear to have linear behavior for lower voltages until the intersection with FN; this intersection point occurs at a higher current density than the other wavelength figures. As the wavelength increases, the GTFP and MFD lines appear to decrease before intersecting with FN, and then they increase after the intersection.
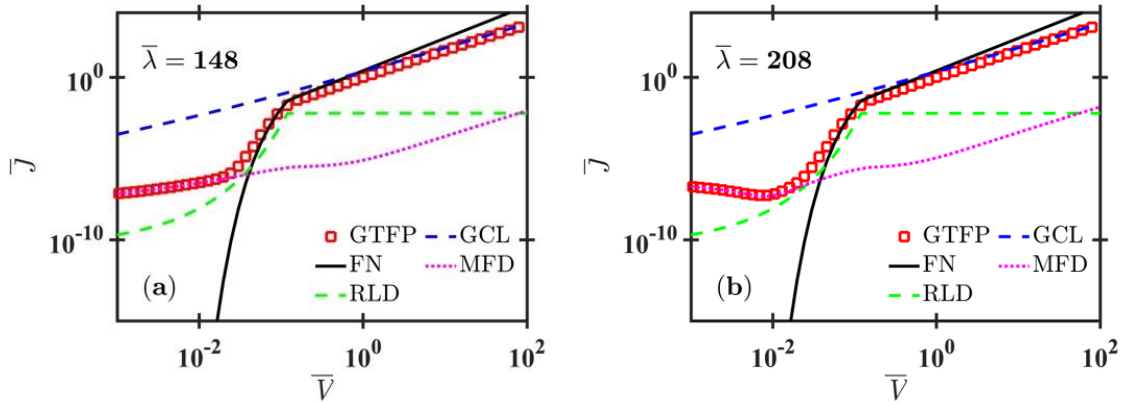
Figure 3.4. Dimensionless current density $\bar{J}$ as a function of the nondimensional voltage $\bar{V}$ for the full solution (GTFP) and asymptotic limits for GCL (blue), FN (black), RLD (green), and MFD (magenta) for different variations of the nondimensionalized wavelength, $\bar{\lambda}$, (a) 148, (b) 208, (c) 225, (d) 295, (e) 363, (f) 448, and (g) 590 for a temperature of 2750 K ($\bar{T}_N$). These plots are for a Cu cathode with $D = 1\,nm$, $F_\lambda = R(\theta) = 0.5$, and $I_i = 3.2 \times 10^{11}\,Wm^{-2}$.

Figure 3.5. continued.
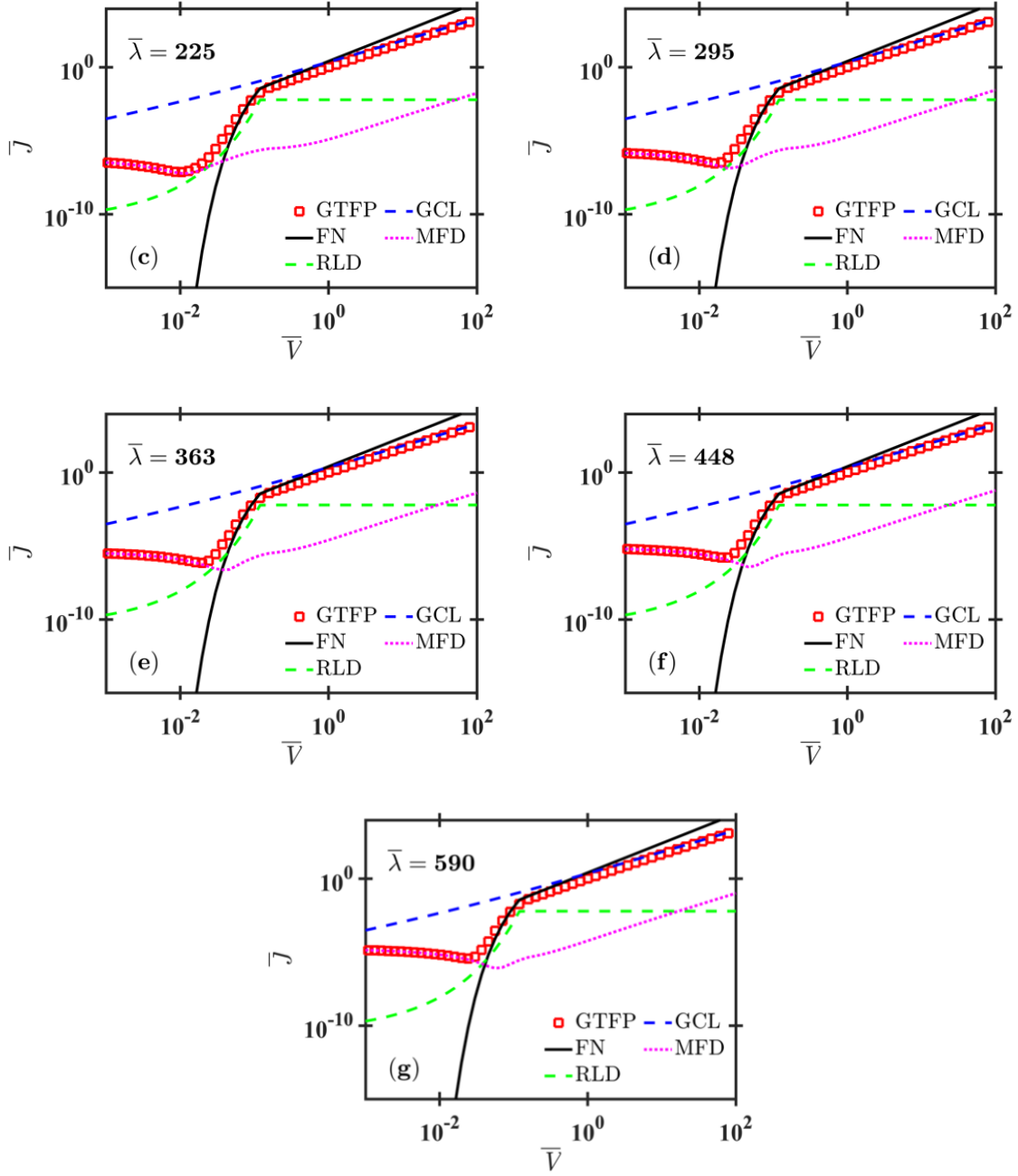
As with the λ, the I_i affects how the MFD transitions between the other emission mechanisms. The laser variations in table 3.3 range from 10^3 to $10^{15}\ Wm^{-2}$.

Table 3.3. Laser Intensity, I_i, variations

Variation	$I_i\ [Wm^{-2}]$
1	3.2×10^3
2	3.2×10^7
3	3.2×10^{11}
4	3.2×10^{15}

To demonstrate the effects of I_i, we plotted the GTFP equation as a function of $\bar{V}$ for various magnitudes of I_i, included in table 3.3, at the nexus temperature, $\bar{T}_N = 0.0527$ for a Cu cathode with scattering and reflectivity equal to 0.5 and $\lambda = 266\ nm$. Figure 3.4(a) demonstrates the effects varying I_i has on the GTFP equation. As I_i increases, the GTFP equation begins to look similar to the GCL equation. Figure 3.4(b) shows that as I_i increases the ratio of GTFP and GCL approaches a value closer to 1; GCL and GTFP for $I_i = 3.2 \times 10^{15}\ Wm^{-2}$ has the closest value to one.
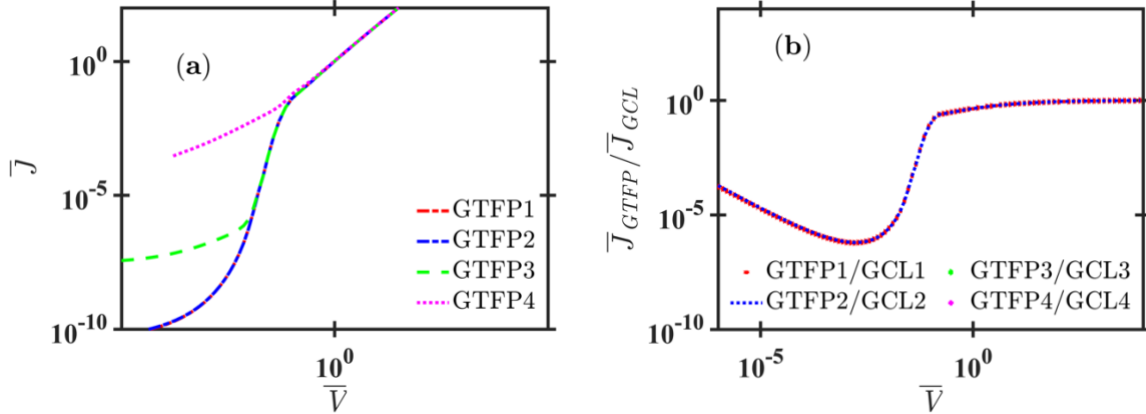
Figure 3.6. These two figures demonstrate the effects of the laser intensity, I_i, on the nondimensionalized current density, $\bar{J}$ as a function of nondimensionalized voltage, $\bar{V}$. (a) As the laser intensity increases in magnitude, the current density approaches the asymptotic limit of GCL. (b) With increasing I_i, $\bar{J}_{GTFP}/\bar{J}_{GCL} \rightarrow 1$. The magnitudes of I_i are included in Table 3.3. These are plotted for a Cu cathode with $D = 1\ nm$, $F_\lambda = R(\theta) = 0.5$, and a nexus temperature of 2750 K ($\bar{T}_N = 0.0527$).

F_λ and $R(\theta)$ are not expected to have as great an impact of the laser intensity due to the differences in magnitude. To determine the impact of these two factors, we plotted different F_λ and $R(\theta)$ variations between 0 and 1 included in table 3.4; this is figure 3.5.

Table 3.4. Laser scattering, F_λ, and reflectivity, $R(\theta)$, variations

Variation	F_λ	$R(\theta)$
1	0.2	0.1
2	0.4	0.3
3	0.6	0.5
4	0.8	0.7
5	0.9	0.9

For figure 3.5, we plotted the nondimensional current density as a function of voltage $\bar{J} = \bar{J}(\bar{V})$ for a Cu cathode with $D = 1\ nm$, $\lambda = 266\ nm$, and $I_i = 3.2 \times 10^{11}\ Wm^{-2}$ for a nexus temperature of $2750\ K$ ($\bar{T}_N = 0.0527$). Figure 3.5(a) is the scattering, F_λ, case for a constant $R(\theta)$ of 0.5. Figure 3.5(b) is the reflectivity, $R(\theta)$, case for a constant F_λ of 0.5. From these figures we can see that the change in F_λ or $R(\theta)$ does not alter the GTFP equations drastically.
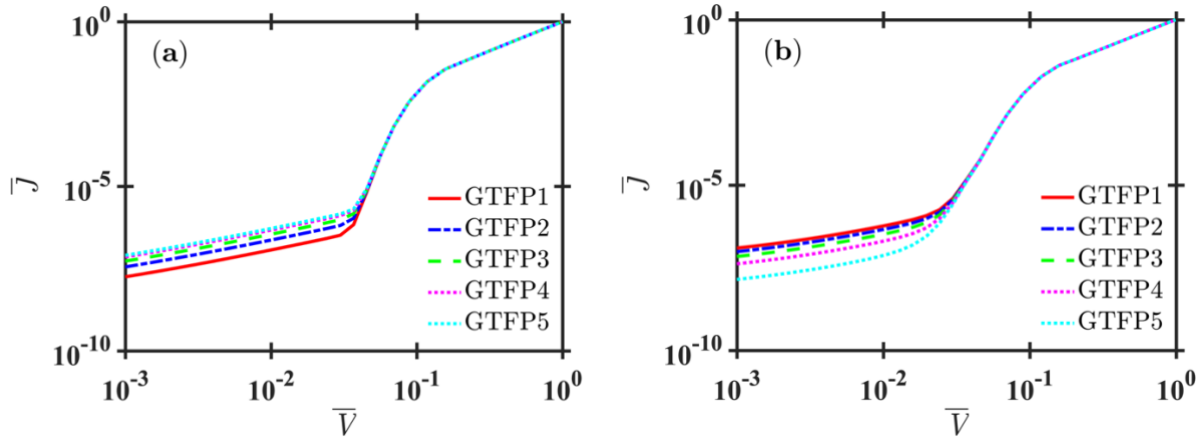
Figure 3.7. These plots show the effects of increasing the magnitude of (a) the F_λ and (b) the $R(\theta)$ for the five variations listed in Table 3.4. These plots are for a Cu cathode with $D = 1\ nm$, $I_i = 3.2 \times 10^{11}\ Wm^{-2}$, and a nexus temperature of $2750\ K$ ($\bar{T}_N = 0.0527$) .

These results determine that the laser intensity has a greater effect on the model fit than the scattering and reflectivity values. Therefore, further studies regarding the laser intensity and the effects on emission mechanism would be beneficial to understanding the transitions between these regions.

Phase plots are used to demonstrate the potential transitions between the different emission mechanisms using voltage and other parameters of interest. By plotting these figures, we are able to determine at which point a certain emission mechanism may dominate at certain conditions. For

this research, the phase plots show the different variations between $\overline{D}, \bar{\mu}, \overline{T}$, and $\overline{\hbar\omega}$. Each of these phase plots require all of the variables to be held constant except for the variable of interest. The variables of interest for this analysis are resistance $\overline{R}$, gap distance $\overline{D}$, mobility $\bar{\mu}$, temperature $\overline{T}$, effective laser constant $\overline{I}_{eff}$, and photon energy $\overline{\hbar\omega}$. For each of these phase plots, a solid black line represents a second order nexus between two emission mechanisms. More nexus relationships can be added to each plot which leads to plots with multiple regions. These multiple nexus phase plots are quite complicated and difficult to interpret. To demonstrate the construction of these phase plots, we will begin with second order nexus plots and add one new nexus for every new plot, as outlined in Figures 3.6-3.12.

To demonstrate the construction of these phase plots, we begin with figures 3.6(a)-(f) and 3.7(a)-(d) by plotting nondimensionalized voltage $\overline{V}$ as a function of nondimensionalized gap distance, $\overline{D}$, for a Cu cathode with a temperature of 5.222 K ($\overline{T} = 1 \times 10^{-4}$), a mobility of 0.0279 $m^2V^{-1}s^{-1}$ ($\bar{\mu} = 4 \times 10^2$), a resistance of 8.07×10⁻⁷ Ω ($\overline{R} = 1 \times 10^7$), an effective laser property of 3.02×10¹⁵ Wm^{-2} ($\overline{I}_{eff} = 1 \times 10^{-2}$), a wavelength of 266 nm ($\bar{\lambda} = 147$), and a photon energy of 4.66 eV ($\overline{\hbar\omega} = 0.0397$). Figures 3.6(a)-(f) show different second order nexuses between (a) OL and CL, (b) CL and MG, (c) MG and MFD, (d) FN and RLD, (e) MFD and FN, and (f) OL and MG. After building the second order nexus plots, we created figure 3.7(a)-(d); with each subplot, we add another nexus relationship, which is the red line, until we get a phase plot with nexus relationships with CL, OL, FN, MG, and MFD. For figure 3.7(a), we began with the second order nexus between OL and CL and added the second order nexus between CL and MG. Figure 3.7(b) incorporates the OL-CL and CL-MG nexuses with the addition of the nexus between MG and MFD. The MFD and FN nexus is included in figure 3.7(c) with the OL-CL, CL-MG, and MG-MFD nexuses. The final subplot, figure 3.7(d), includes the nexus between FN and RLD along with the OL-CL, CL-MG, MG-MFD, and FN-MFD nexuses. In figure 3.7(d), there is a possible nexus between CL, MG, MFD, and FN at an approximate nondimensionalized gap distance, $\overline{D}$, and voltage, $\overline{V}$, of 1.96×10^5 and 3.56×10^4, respectively; the dimensional values are $D = 3.54 \times 10^{-4}$ m and 4.19×10^6 V. At high $\overline{V}$ and low $\overline{D}$, OL transitions to CL as $\overline{D}$ increases, and as $\overline{D}$ continues to increase, CL transitions to MG which than transitions to MFD. Overall as the voltage and gap distance increase, the emission mechanism deviates from temperature dependence towards field emission and space-charge limited emission. Note that although certain mechanisms

dominate at certain conditions, it does not mean that the dominant emission mechanism is not the only one occurring at those conditions.

Figure 3.8. The phase plots for second order nexus points as a function of nondimensional voltage $\bar{V}$ and nondimensional gap distance $\bar{D}$ are (a) Ohm's Law (OL) and Child-Langmuir (CL), (b) CL and Mott-Gurney (MG), (c) MG and modified Fowler-DuBridge (MFD), (d) Fowler-Nordheim (FN) and Richardson-Laue-Dushman (RLD), (e) FN and MFD, and (f) OL and MG. Each of these plots represent a second order nexus with $T = 5.222\ K$ $(\bar{T} = 1 \times 10^{-4})$, $\mu = 0.0279\ m^2V^{-1}s^{-1}$ $(\bar{\mu} = 4 \times 10^2)$, $R = 8.07 \times 10^{-7}\ \Omega$ $(\bar{R} = 1 \times 10^7)$, $I_{eff} = 3.02 \times 10^{15}\ Wm^{-2}$ $(\bar{I}_{eff} = 1 \times 10^{-2})$, $\lambda = 266\ nm$ $(\bar{\lambda} = 147)$, and $\hbar\omega = 4.66\ eV$ $(\bar{\hbar\omega} = 0.0397)$.
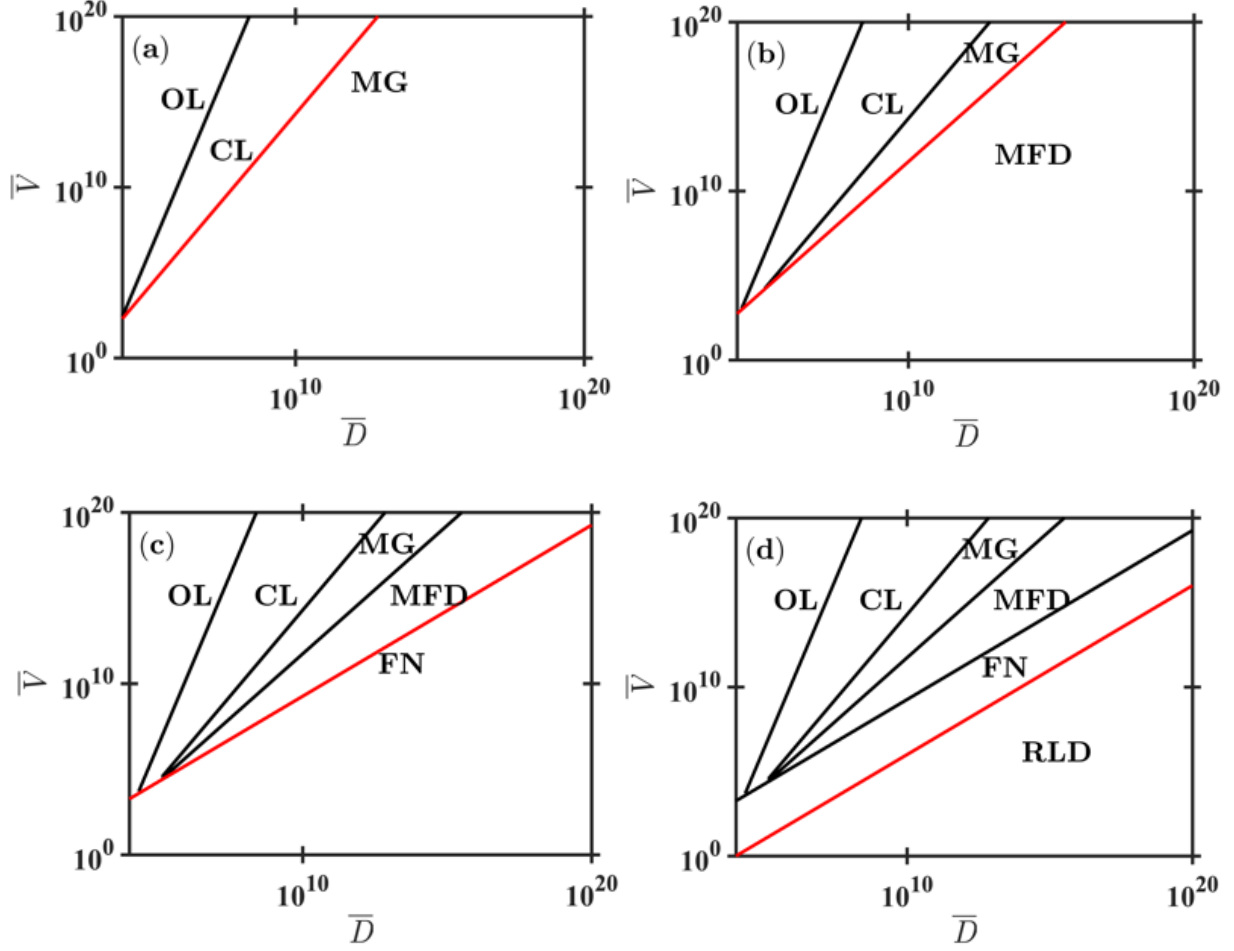
Figure 3.9. The phase plots for nexus points as a function of nondimensional voltage $\bar{V}$ and nondimensional gap distance $\bar{D}$ are (a) Ohm's law (OL)-Child-Langmuir (CL) and CL-Mott-Gurney (MG), (b) OL-CL, CL-MG, and MG-modified Fowler-DuBridge (MFD), (c) OL-CL, CL-MG, MG-MFD, and MFD-Fowler-Nordheim (FN), and (d) OL-CL, CL-MG, MG-MFD, MFD-FN, and FN-Richardson-Laue-Dushman (RLD). The properties for these plots are $T = 5.222\ K$ $(\bar{T} = 1 \times 10^{-4})$, $\mu = 0.0279\ m^2 V^{-1} s^{-1}$ $(\bar{\mu} = 4 \times 10^2)$, $R = 8.07 \times 10^{-7}\ \Omega$ $(\bar{R} = 1 \times 10^7)$, $I_{eff} = 3.02 \times 10^{15}\ Wm^{-2}$ $(\bar{I}_{eff} = 1 \times 10^{-2})$, $\lambda = 266\ nm$ $(\bar{\lambda} = 147)$, and $\hbar\omega = 4.66\ eV$ $(\overline{\hbar\omega} = 0.0397)$.

Figures 3.6 and 3.7 were developed for Cu; however, replacing the fermi energy level with 18.08 eV changes the figures to model W. This results in miniscule changes to the different regions. We can connect these plots to experiments using W diodes with surface coatings that lower the WF. When we change the fermi level, the changes of the regions are miniscule. We can connect these plots to experiments using W diodes with surface coatings. The mobility will change based depending on the temperature and the gas or liquid being used.

The next set of phase plots, figures 3.8(a)-(e) and 3.9(a)-(f), look at the relationship between $\bar{V}$ and $\bar{\mu}$ for a Cu cathode with a temperature of 522 K ($\bar{T} = 1 \times 10^{-2}$), a gap distance of 0.018 m ($\bar{D} = 1 \times 10^{7}$), a resistance of 8.07x10^{-8} Ω ($\bar{R} = 1 \times 10^{6}$), an effective laser property of 3.02x10^{12} Wm^{-2} ($\bar{I}_{eff} = 1 \times 10^{-5}$), a wavelength of 266 nm ($\bar{\lambda} = 147$), and a photon energy of 4.66 eV ($\overline{\hbar\omega} = 0.0397$). As with the previous phase plots, we first plot the second order nexuses in figure 3.8 between 3.8(a) MG and MFD, 3.8(b) MG and FN, 3.8(c) CL and MG, 3.8(d) MG and OL, and 3.8(e) FN and CL. Figure 3.9(a)-(f) connect the various second order nexuses. Figure 3.9(a) connects the second order nexuses between MG-MFD, FN-MFD, and FN-MG (red). Figure 3.9(b) adds the second order nexus between MG and CL (red) which causes the FN region to shrink; the nexus between MG and FN is now represented by the dotted green line. Figure 3.9(c) adds the nexus relation between FN and CL (red). Figure 3.9(d) introduces the nexus between OL and CL (red), and figure 3.9(e) adds the final nexus relation between MG and OL (red); for both 3.9(d) and 3.9(e), the nexus between FN and CL is represented by a blue dotted line to differentiate between the MFD-FN and FN-CL nexuses. The figure 3.9(f) does not introduce any additional nexuses; this figure magnifies the FN nexuses for the nondimensionalized mobility range of $10^{1} - 10^{6}$ and the nondimensionalized voltage range of $10^{4} - 10^{10}$. For high $\bar{V}$ and lower $\bar{\mu}$, MG dominates. CL initially dominates at high $\bar{V}$ and $\bar{\mu}$ before transitioning to OL. Understanding the transitions as a function of $\bar{\mu}$, could be important when looking into potential phases changes between vapors and liquids. This mobility is also related to the pressure; this relationship to pressure could be useful when looking into low temperature applications.
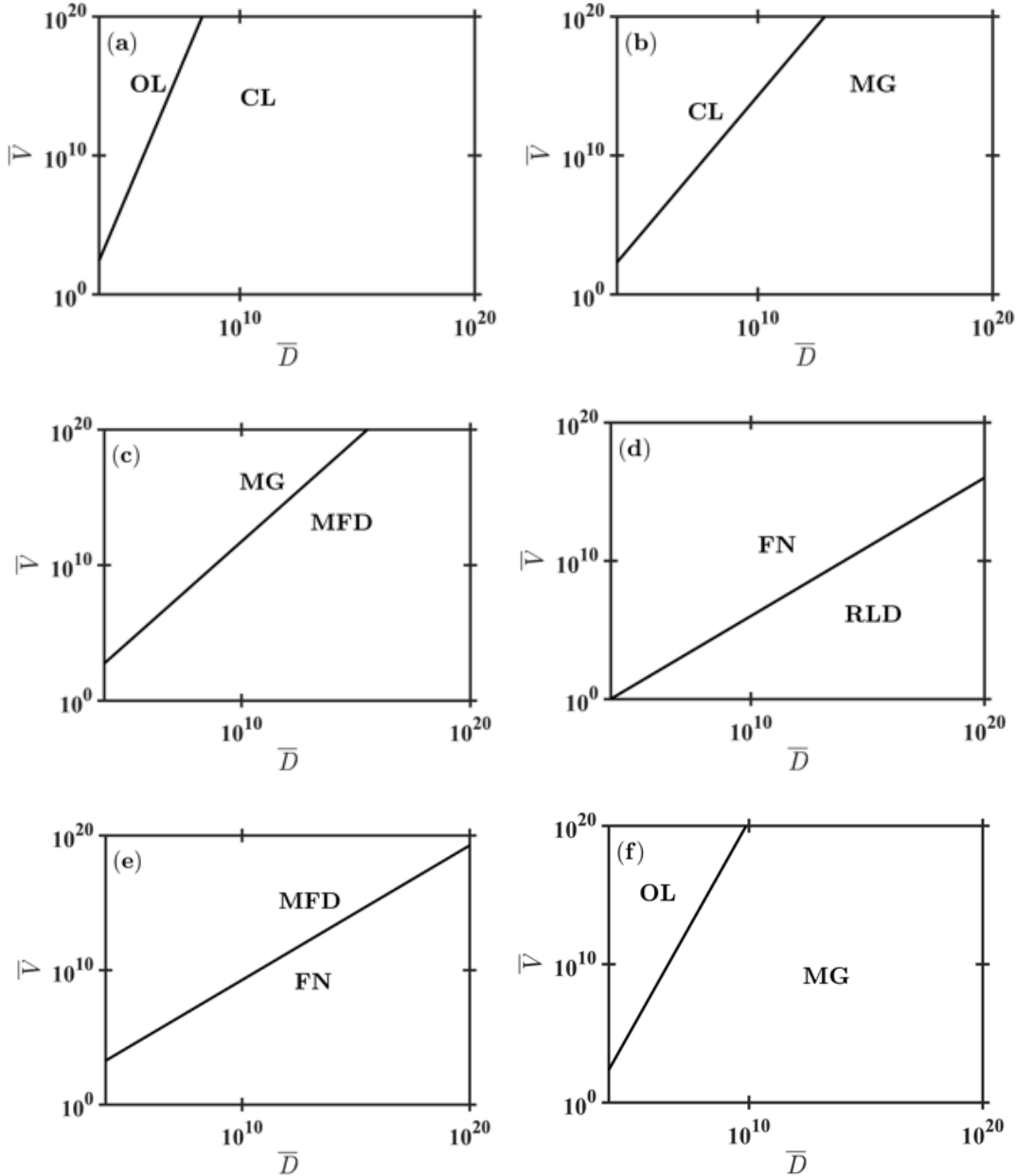
Figure 3.10. The phase plots for second order nexus points as a function of nondimensional voltage $\bar{V}$ and nondimensional mobility $\bar{\mu}$ are (a) Mott-Gurney (MG) and Modified-Fowler DuBridge (MFD), (b) Fowler Nordheim (FN) and MG, (c) Child-Langmuir (CL) and MG, (d) Ohm's Law (OL) and MG, and (e) FN-CL. The properties for these plots are $T = 522\ K$ ($\bar{T} = 1 \times 10^{-2}$), $D = 0.018\ m$ ($\bar{D} = 1 \times 10^{7}$), $R = 8.07 \times 10^{-8}\ \Omega$ ($\bar{R} = 1 \times 10^{6}$), $I_{eff} = 3.02 \times 10^{12}\ Wm^{-2}$ ($\bar{I}_{eff} = 1 \times 10^{-5}$), $\lambda = 266\ nm$ ($\bar{\lambda} = 147$), and $\hbar\omega = 4.66\ eV$ ($\bar{\hbar\omega} = 0.0397$).
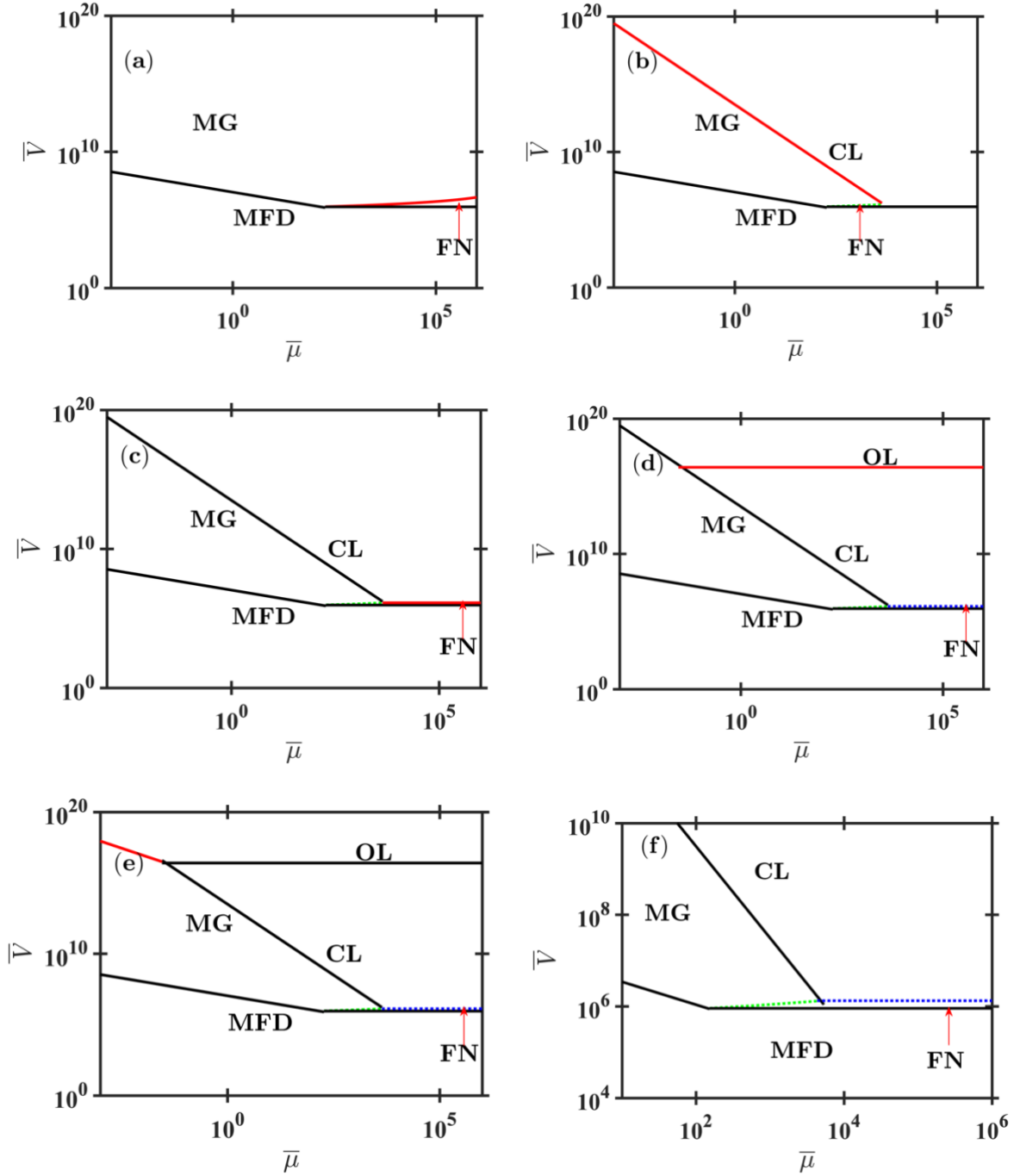
Figure 3.11. The phase plots for second order nexus points as a function of nondimensional voltage $\bar{V}$ and nondimensional mobility $\bar{\mu}$ are (a) Mott-Gurney (MG) and Modified-Fowler DuBridge (MFD), Fowler Nordheim (FN) and MG, FN-MFD (b) MG-MFD, FN-MG, FN-MFD, and Child-Langmuir (CL) and MG, (c) MG-MFD, FN-MG, FN-MFD, CL-MG, and FN-CL, (d) MG-MFD, FN-MG, FN-MFD, CL-MG, FN-CL, and Ohm's Law (OL) and CL, (e) MG-MFD, FN-MG, FN-MFD, CL-MG, FN-CL, OL-CL, and MG-OL, and (f) MG-MFD, FN-MG, FN-MFD, CL-MG, and FN-CL. For (b)-(f), the green dotted line is FN-MG. For (d)-(f), the blue dotted line is FN-CL. The properties for these plots are $T = 522\ K\ (\bar{T} = 1 \times 10^{-2})$, $D = 0.018\ m$ $(\bar{D} = 1 \times 10^7)$, $R = 8.07 \times 10^{-8}\ \Omega\ (\bar{R} = 1 \times 10^6)$, $I_{eff} = 3.02 \times 10^{12}\ Wm^{-2}\ (\bar{I}_{eff} = 1 \times 10^{-5})$, $\lambda = 266\ nm\ (\bar{\lambda} = 147)$, and $\hbar\omega = 4.66\ eV\ (\overline{\hbar\omega} = 0.0397)$.

The third phase plot, figures 3.10(a)-(e) and 3.11(a)-(d) shows the dependence of the emission mechanisms on nondimensionalized voltage, $\bar{V}$, and nondimensionalized photon energy, $\overline{\hbar\omega}$, for a Cu cathode with a temperature of 2611 K ($\bar{T} = 5 \times 10^{-2}$), a gap distance of 0.018 m ($\bar{D} = 1 \times 10^7$), a mobility of 4.88 $m^2V^{-1}s^{-1}$ ($\bar{\mu} = 7 \times 10^4$), a resistance of 8.07x10^{-5} Ω ($\bar{R} = 1 \times 10^9$), and an effective laser property of 3.02x10^{15} Wm^{-2} ($\bar{I}_{eff} = 1 \times 10^{-2}$). Figure 3.10(a)-(e) are the second order nexus plots for MFD and (a) FN, (b) RLD, (c) CL, (d) MG, and (e) OL. Now as with the nexus plots for the nondimensionalized voltage and gap distance, we slowly build the nexus plot by adding a new nexus with every subplot; this is figure 3.11(a)-(d). Each red line represents the nexus that has been added.
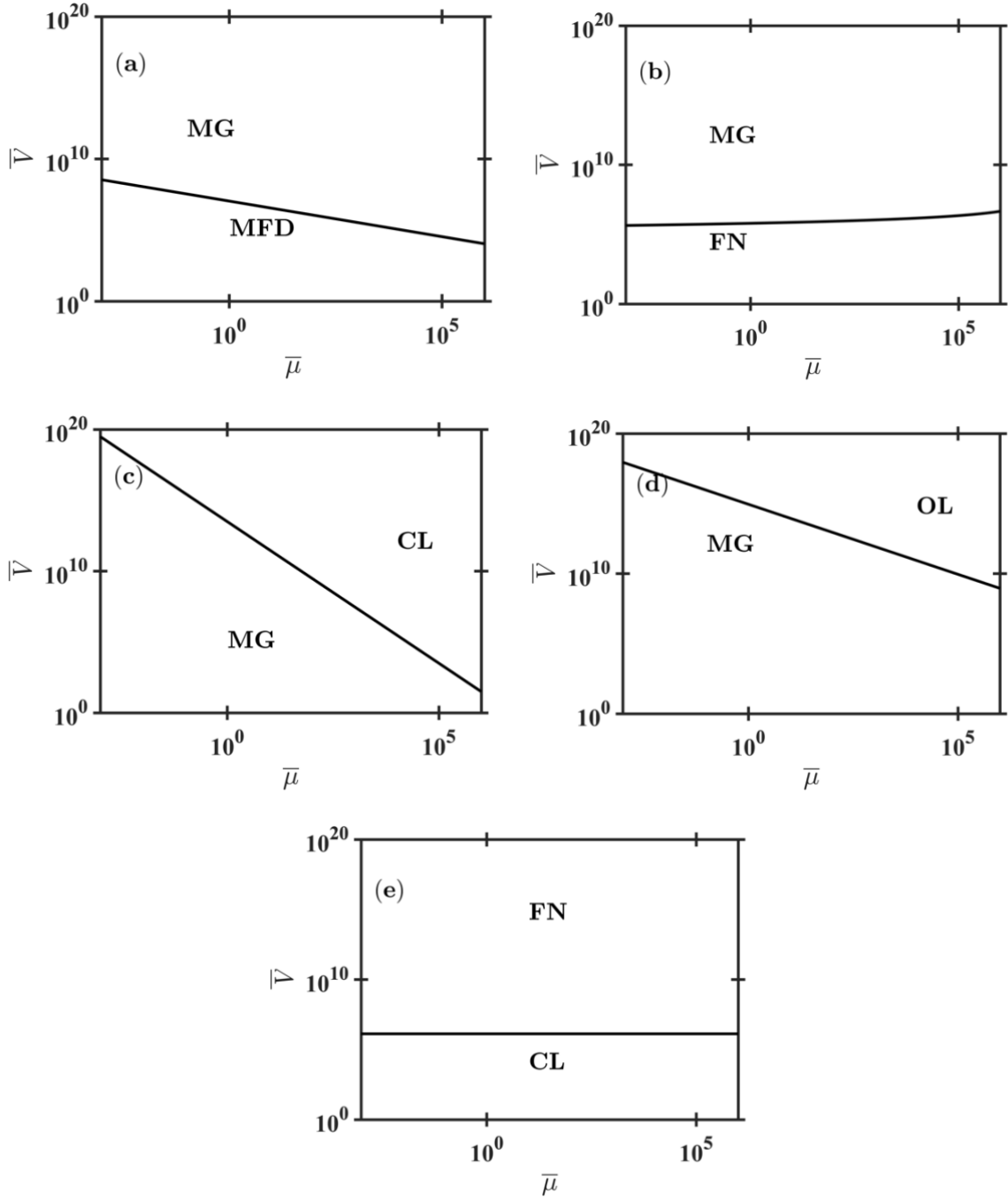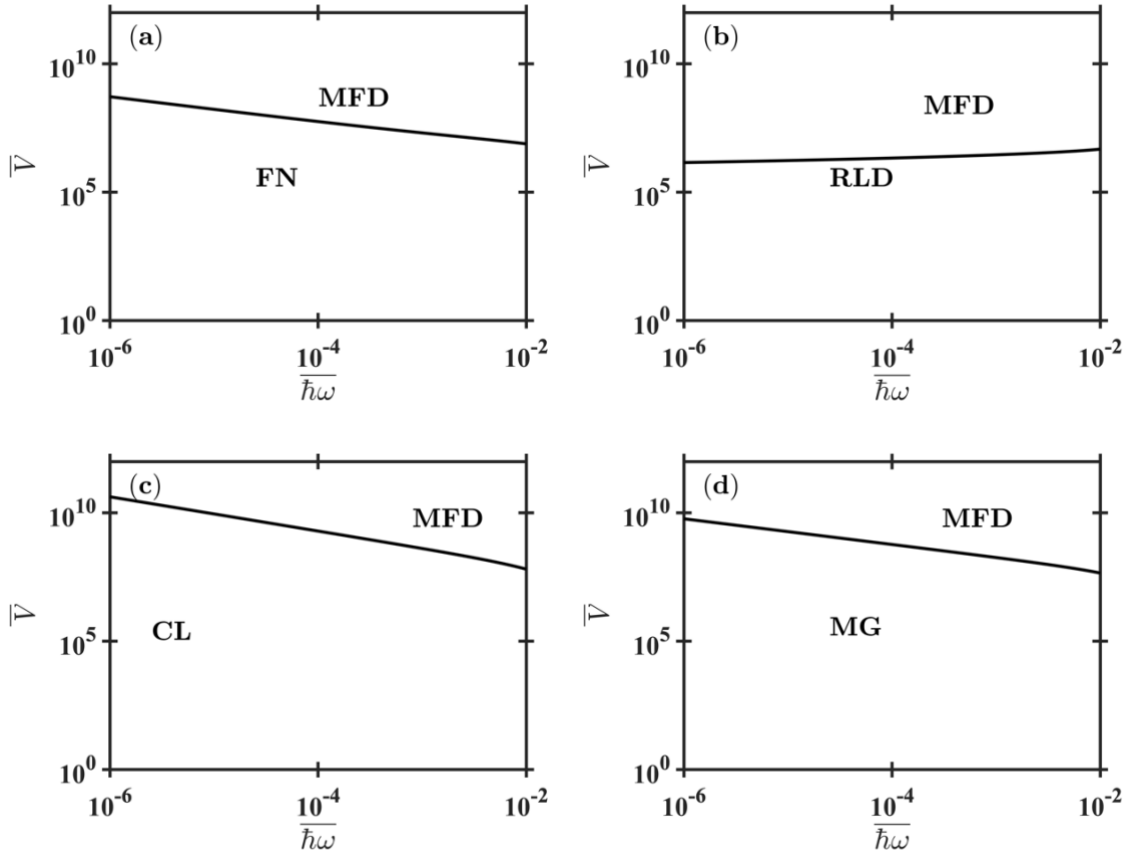

Figure 3.12. The phase plots for second order nexus points as a function of nondimensional voltage $\bar{V}$ and $\overline{\hbar\omega}$ are (a) Fowler-Nordheim (FN) and Modified Fowler-DuBridge (MFD), (b) Richardson-Luae-Dushmann (RLD) and MFD, (c) Child-Langmuir (CL) and MFD, (d) Mott-Gurney (MG) and MFD, and (e) Ohm's law (OL) and MFD. The properties for these plots are $T = 2611\ K$ ($\bar{T} = 5 \times 10^{-2}$), $D = 0.018\ m$ ($\bar{D} = 1 \times 10^7$), $\mu = 4.88\ m^2V^{-1}s^{-1}$ ($\bar{\mu} = 7 \times 10^4$), $R = 8.07 \times 10^{-5}\ \Omega$ ($\bar{R} = 1 \times 10^9$), and $I_{eff} = 3.02 \times 10^{15}\ Wm^{-2}$ ($\bar{I}_{eff} = 1 \times 10^{-2}$).

Figure 3.13. continued.
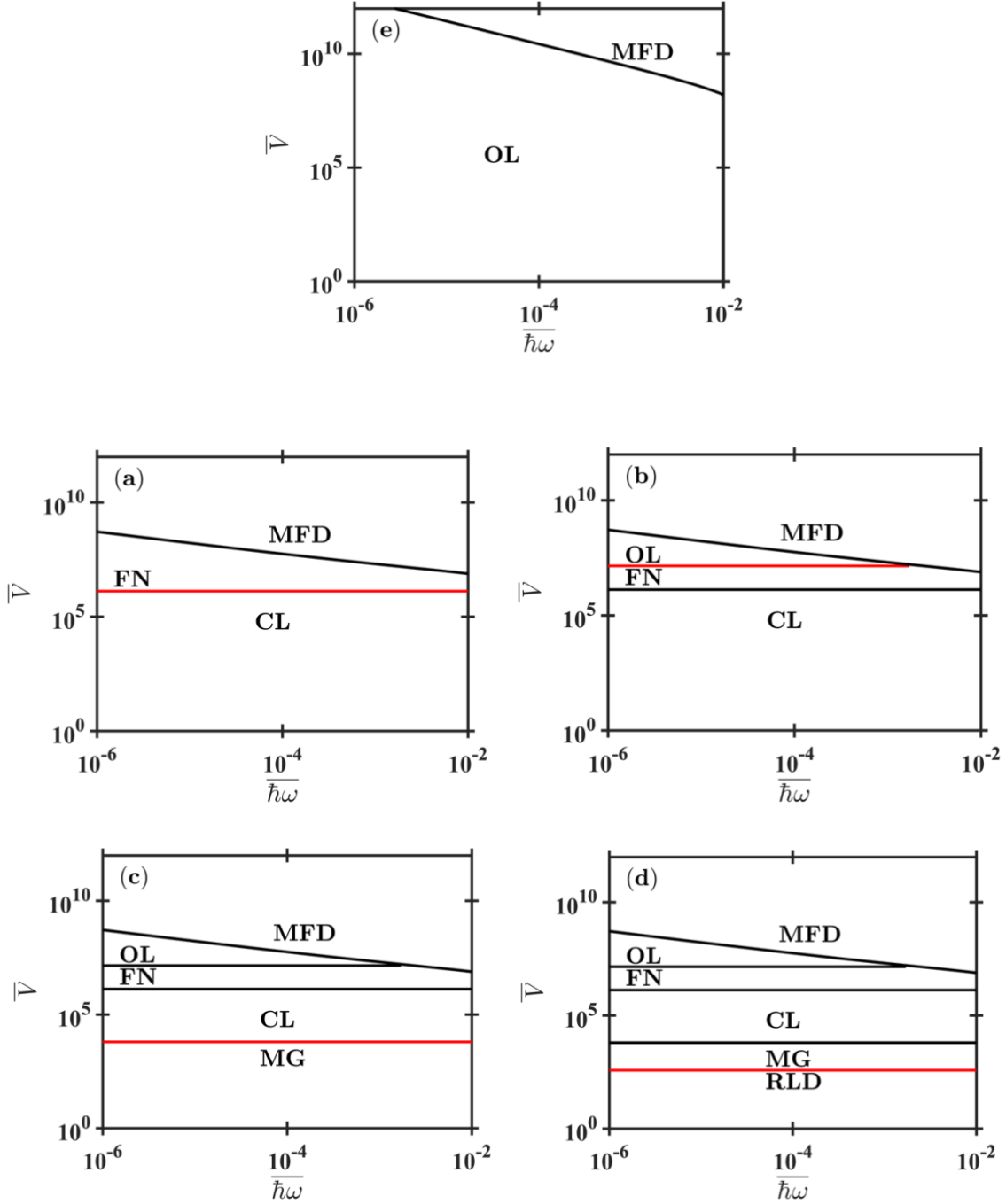
Figure 3.14. The phase plots are for nexus points as a function of nondimensional voltage $\bar{V}$ and $\overline{\hbar\omega}$ are (a) Fowler-Nordheim (FN)-modified Fowler-DuBridge (MFD) and Child-Langmuir (CL)-FN, (b) FN-MFD, FN-CL, and Ohm's law (OL)-FN, (c) FN-MFD, FN-CL, OL-FN, and CL-MG, and (d) FN-MFD, FN-CL, OL-FN, CL-MG, and Richardson-Laue-Dushman (RLD)-MG. The properties for these plots are $T = 2611\ K\ (\bar{T} = 5 \times 10^{-2})$, $D = 0.018\ m\ (\bar{D} = 1 \times 10^{7})$, $\mu = 4.88\ m^2 V^{-1} s^{-1}\ (\bar{\mu} = 7 \times 10^{4})$, $R = 8.07 \times 10^{-5}\ \Omega\ (\bar{R} = 1 \times 10^{9})$, and $I_{eff} = 3.02 \times 10^{15}\ Wm^{-2}\ (\bar{I}_{eff} = 1 \times 10^{-2})$.

Figure 3.12 plots $\bar{V}$ as a function of $\bar{T}$ for a Cu cathode with a gap distance of 0.018 m $(\bar{D} = 1 \times 10^7)$, a mobility of 0.0488 $m^2V^{-1}s^{-1}$ $(\bar{\mu} = 7 \times 10^2)$, a resistance of 8.07x10^{-4} Ω $(\bar{R} = 1 \times 10^{10})$, an effective laser property of 3.02×10^{12} Wm^{-2} $(\bar{I}_{eff} = 1 \times 10^{-5})$, a wavelength of 266 nm $(\bar{\lambda} = 147)$, and a photon energy of 4.66 eV $(\overline{\hbar\omega} = 0.0397)$. To convert to nondimensionalized temperature, the dimensional temperature is divided by $T_0 = 5.22 \times 10^4 K$. All of the emission mechanisms are connected on this plot creating a seventh order nexus plot. OL, CL, and MG do not rely on a temperature dependence which is why the nexus lines do not vary with temperature. With lower temperatures and voltages, FN dominates. As the voltage increases, FN transitions to MG which goes to CL and then to OL. Now when the temperature increases, FN transitions to MFD which then transitions to RLD. At high temperatures and voltages, RLD is expected to be the dominate emission mechanism because of the model's dependence on temperature.
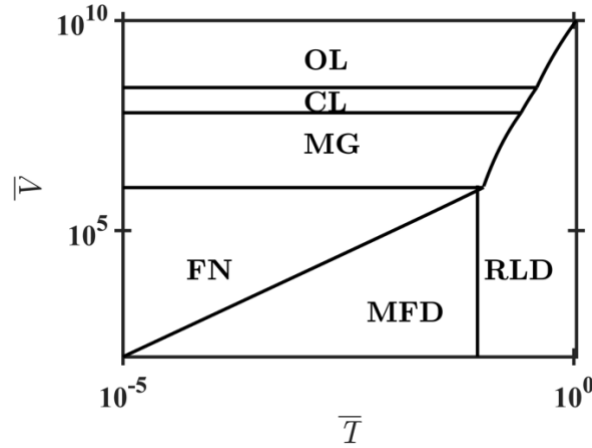
Figure 3.15. Phase plot for second order nexuses of Ohm's law (OL) and Child-Langmuir (CL), CL and Mott-Gurney (MG), MG and Fowler-Nordheim (FN), FN and Modified Fowler DuBridge (MFD), MFD and Richardson-Laue-Dushman (RLD), RLD and FN, RLD and MG, RLD and CL, and RLD and OL as a function of nondimensional voltage, $\bar{V}$, and temperature, $\bar{T}$. The constants for this plot are $\mu = 0.0488\ m^2V^{-1}s^{-1}$ $(\bar{\mu} = 7 \times 10^2)$, $D = 0.018\ m$ $(\bar{D} = 1 \times 10^7)$, $R = 8.07 \times 10^{-4}\ \Omega$ $(\bar{R} = 1 \times 10^{10})$, $I_{eff} = 3.02 \times 10^{12}\ Wm^{-2}$ $(\bar{I}_{eff} = 1 \times 10^{-5})$, $\lambda = 266\ nm$ $(\bar{\lambda} = 147)$, and $\hbar\omega = 4.66\ eV$ $(\overline{\hbar\omega} = 0.0397)$.

3.5   Conclusion

We incorporated photoemission (PE) into the most recent model connecting different electron emission mechanisms. This model is created using nexus theory which utilizes the asymptotic limits of fundamental equations to find a transition point between the various equations. The model we adapted to incorporate PE already included FN for FE, GCL and CL for SCLE, MG

for SCLE with collisions, RLD for TE, and OL. To add PE to this model, we used the GTFP equation and the MFD. The GTFP equation is the GTF equation with the addition of PE; it accounts for laser properties and electric field strength and temperature. The MFD equation is mainly impacted by laser properties such as laser intensity, I_i, and wavelength, λ; this dependence and impact can be modeled using the photon energy, $\hbar\omega$.

Using the initial conditions and nondimensionalized fundamental equations, we determined the asymptotic solutions for each emission mechanisms. We found a sixth order nexus between RLD, FN, CL, MG, OL, and MFD using nexus theory and the asymptotic equations. Using these asymptotic solutions and the full solution modeled by GTFP, we were able to model the typical $\bar{J}$ as a function of $\bar{V}$ for various temperatures and laser wavelengths. From this plot we determined an approximate nexus temperature between FN, GTFP, MFD, and RLD to be $\bar{T}_N = 0.527$ $(2.75 \times 10^3 \, K)$ for a wavelength of $266 \, nm$. For that nexus temperature, we plotted various values of λ to address the effect of λ; as λ increases, the nexus point between RLD, MFD, and FN increases.

To see the connection between the different asymptotic limits and important variables, we created numerous phase plots that evaluated the relationship between $\bar{V}$ and another variable. The first group of phase plots were for $\bar{V}$ and $\bar{D}$; it appears that MFD was the dominate emission mechanism between MG and FN. At high $\bar{V}$, the mechanisms transitioned from OL to CL to MG to MFD to FN as the gap distance increased. The transition between FN and RLD occurred at lower voltages. The next set of phase plots were functions of $\bar{V}$ and $\bar{\mu}$; MG dominated for high $\bar{V}$ and low $\bar{\mu}$, while MFD dominated for lower $\bar{V}$. Eventually MFD transitioned to FN at higher $\bar{\mu}$, and then FN transitioned to CL as the voltage increased. Then CL transitioned to OL at high voltages and mobilities. The third set of phase plots were functions of $\bar{V}$ and $\overline{\hbar\omega}$; these plots were incorporated because of the addition of PE. PE is heavily dependent on the photon energy which depends on the laser properties. For a higher $\bar{V}$, MFD dominates. From this phase plot, we see that as the voltage increases, the emission mechanisms transition from RLD to MG to CL to FN to OL and finally to MFD. The final phase plot examined the relationship between $\bar{V}$ and $\bar{T}$. Now for this phase plot, RLD dominated at higher $\bar{T}$ which was expected.

We briefly examined the impact of the laser properties. We determined that the laser wavelength λ and intensity I_i have the greatest impact on the emission model through graphing variations in these parameters. As the laser intensity and wavelengths increase, the nexus point

increases. When the laser intensity increases, the GTFP equation approaches the behavior of the GCL equation, and when the wavelength increases, the nexus point increases. For this analysis, we assume I_i, $R(\theta)$, and F_λ are constant properties; we chose to hold these variables constant to simplify the analysis. However, F_λ and $R(\theta)$ can be calculated using complex equations from the moments-based approach, and the laser intensity if often described using a Gaussian distribution that is time dependent.

To expand this research other variable dependences and cathode materials could be examined; these cathodes could include cesiated or treated materials such as cesiated tungsten. Changing the cathode material will not have a major effect on the outcome of the model, but it could provide a more relatable analysis to laser experiments. The laser research can be extended to included various types of lasers with nonconstant definitions for various laser properties. Further experimental data would provide a more accurate analysis of this emission model. Understanding the transition to PE, provides information for designing vacuum electronics, laser experiments, and particle accelerators.

4. CONCLUSION

4.1 Liquids

4.1.1 Process and Results

The initial goal of analyzing electron emission in liquids was to determine if a model derived using nexus theory for gases could be applied to liquids. To determine the applicability of this model to liquids, we used data from a relevant experiment (Dotoku *et al*., 1978) to test the gaseous model. The experimental data provided some challenges for the analysis such as a small number of data points; however, we were able to address each challenge. Through trial and error, we determined that the factors that affected the model the most were the emission area and the mobility of the liquid.

For the emission model to work, the current needs to be converted to current density which requires knowledge of the emission area. The notional emission area S_n is used to convert the current to current density for the data to be used in the emission model. Using a linear best fit, we determined A'_{FN} and B'_{FN}. Utilizing the notional emission area S_n and the gap distance d we determined the constants A_{FN} and B_{FN} which are necessary for the nondimensionalization of the data for the model. The notional emission area is related to the formal emission area using the characteristic local preexponential correction factor λ_C (Forbes *et al*., 2015). The values for this correction factor were not within the expected range (Forbes, 2012), which we attributed to the data being collected for liquids and not under the usual vacuum conditions.

After nondimensionalizing the data, we performed an orthodoxy test to determine the accuracy of the model and whether it could be used. The values for the orthodoxy test fall within the acceptable range for TMP and TMS; for n-Hexane, the values fall in the range that requires further investigation. For most of the model analysis, the fits are different for n-Hexane in comparison to TMS and TMP which have very similar results. This may be due to the molecular shape which would require further experimental data and studies to determine. However, because the orthodoxy test is mainly based on previous experiments and gas models, we conjecture that this was a decent representation considering our data was acquired for liquids.

After determining the quality of fit of the model, we tested the sensitivity of the model by changing the conditions such as gap distance d and the mobility, μ. For d and μ, we plotted three

values to address the sensitivity of the model to in regard to these parameters. For the gap distance, we plotted three different values that were two orders of magnitude different with the middle value being the actual nondimensionalized gap distance. A smaller gap distance resulted in a faster transition to the space charge regime, and a larger gap distance resulted in a FE dominated regime. Following the test regarding the gap distance sensitivity, we conducted a sensitivity test regarding the mobility which lead to some interesting conclusions regarding the transitions between phases. We researched different liquids, vapors, and gases to see how the mobility changed between the stages. From the initial research, we found the mobility changes, on average, two orders of magnitude when it changes state (Jacobsen *et al.*, 1986; Jacobsen *et al.*, 1989). From this, we plotted the transitions between the states. The initial results suggest that the model may be able to model electron emission phenomena during state transitions. Using representative values for electron mobility for a gas, we observed reasonably achievable device parameters for a third order nexus between CL, MG, and FN. However, these results and conclusions are only based on a few studies, so further studies with other liquids and other conditions are necessary to perform a more comprehensive study of the implications of these observations.

The final aspect of the study addressed the transition regions between the emission mechanisms and the nexus point. For the transition regions, the voltage was plotted as a function of mobility and gap distance. The transition plots indicate that CL would not be expected to occur unless the gap distance is extremely small or the mobility is very high (corresponding to low pressure). The nexus plot also shows that the CL regime is out of reach for the conditions given; this was expected since CL models emission for vacuum conditions. From this research we determined that the model used for gases could be used for liquids with a few adaptions. This research provides a beginning to the unification of electron emission in different phase change.

4.1.2   Future work

The numerous applications for electron emission in liquids provide multiple ways for extending this project. Some of the future work proposed in this section concerns experimental data, orthodoxy, additional emission mechanisms, mobility, and phase changes.

Future work regarding experimental data and orthodoxy could be combined. One of the most important factors when applying models to data is to have a reliable set of data. The data set used for this research is over 30 years old; we did not have access to the experimental setup to

determine how the data was collected. Understanding the independent and dependent variables are necessary for analysis. The major concern with most experimental data is whether the data set is large enough to complete a reliable analysis. Specifically, the data used for this thesis did not have many data points in the FE regime. Therefore, one of the next potential steps would be to conduct an experiment with fixed pressure and temperature using well-characterized liquids with a known geometry. Conducting a new experiment would provide more clear data and control of the experimental set up and liquids being analyzed. The more data points and experiments conducted means that the orthodoxy tests could be improved to look at the reliability of models for emission in liquids. Of particular interest is ongoing work examining electric breakdown of liquid helium for the Spallation Neutron Source (SNS) (Phan *et al*. 2020). Given the sensitivity of liquid helium to undergoing phase changes with slight changes in temperature, this could provide an interesting and relevant model system for applying the theory developed in this thesis.

The next step in the theoretical analysis would be to continue to connect the different emission mechanisms. The model used for this liquid study only included FN, MG, and CL, but the model we used has since been modified to include TE (Darr *et al*., 2020). Using the new model, we could attempt to model TE for liquids. However, to complete this process, we would most likely need a data set in which the temperature is controlled; this implies that we would need to conduct an experiment. Once we have the necessary data, we could adapt the model. If TE can be modeled, the research could be further adapted to account for other emission mechanisms such as photoemission (PE).

Another beneficial addition to the research would be to complete a comprehensive study regarding the mobility for different liquids, gases, solids, and vapors. This would begin with conducting experiments and theoretical calculations to calculate the mobilities for various liquids, gases, solids, and vapors at different conditions; the conditions that would need to be accounted for are the temperature, the density, the structure, the pressure, and the electric field. Once the experiment is completed the data could be used to model the transitions between the phases. First, it would be beneficial to see if the model works for solids, for which MG is well established. Once the solids have been analyzed, the transitions between liquids, solids, and gases may be analyzed together. Then simulations can be completed to analyze the accuracy and precision of the fit. This potential addition to the research could provide a detailed understanding of electron emission for the transitions between the phases.

4.2   Photoemission

4.2.1   Process and Results

The overall goal of this project was to add photoemission, modeled by MFD, to the present unified emission theory Darr *et al.* (2020) that uses nexus theory to connect different emission mechanisms to observe transitions between the mechanisms at various conditions. The current model includes FE, TE, and SCLE with and without collisions; each of these are modeled using fundamental equations such as FN for FE, RLD for TE, GCL and CL for SCLE, and MG for SCLE with collisions.

We first determined the full solution and the fundamental equation to use for the asymptotic limit analysis for nexus theory. The full solution $\bar{J}_{GTFP}(\bar{F}, \bar{T})$ extends $\bar{J}_{GTF}(\bar{F}, \bar{T})$ from Darr *et al.* (2020) by adding the generalized photoemission equation $\bar{J}_p(\bar{F}, \bar{T})$. PE occurs in every region for this equation, but the contribution is small enough that it can be considered negligible in certain scenarios. After determining $\bar{J}_{GTFP}(\bar{F}, \bar{T})$, we focused on the fundamental equation for PE, MFD. Now this equation is relatively straightforward, and it can be nondimensionalized using the same terms as in Darr *et al.*, 2020 with the exception of laser intensity. After the nondimensionalization was complete, we found the asymptotic limit for MFD at the initial conditions ($T = 0$ and $F = 0$). Using this asymptotic limit, we determined the nexus point between MFD and FN. Then using this connection, we exampled various higher order nexuses between RLD, FN, CL, MG, OL, and MFD.

As soon as this nexus was found, we determined the initial properties to use for the analysis and began to create plots for analysis. We began with the $\bar{J} = \bar{J}(\bar{V})$ plots, figure 3.1, for a Cu cathode with a fixed gap distance $D = 1\ nm$ and $I_i = 3.2 \times 10^{11}\ Wm^{-2}$, $\lambda = 266\ nm$, and $F_\lambda = R(\theta) = 0.5$ as the initial laser properties. These plots showed a transition point between GTFP, MFD, FN, and RLD at $\bar{T}_N = 0.527$. Incorporating PE allowed us to examine the impact that the laser properties and other material values had on the theory and transition between emission mechanisms. The first property we looked at was the cathode material which included changing the Fermi energy level and the work function; this did not result in any changes from figure 3.1 that could be seen. Figure 3.2 shows that increasing the wavelength minimally increased the nexus point. Figure 3.3 shows the effect that increasing the laser intensity has while figure 3.4 shows the minimal effect that changing the reflectivity and scattering have.

The most important figures for the analysis are the phase plots, which show the different nexuses between the fundamental equations and the regions where the emission mechanisms dominate at certain conditions. For this analysis, we began by looking at gap distance; these plots, figures 3.6 and 3.7, demonstrated that the temperature dependent mechanisms dominate at higher voltages and gap distances, while the temperature independent equations (CL, FN, MG, OL) dominate at higher voltages and small gap distances. Figures 3.8 and 3.9 show the dependence that the nexuses have on the mobility. As the mobility increases, MFD transitions to FN; as the voltage increases, MFD transitions to MG. Figures 3.10 and 3.11 demonstrated that MFD is dominant at lower voltages and photon energies. Figure 3.12 demonstrated the relationships between temperature and the emission mechanisms; RLD is dominant at higher temperatures.

4.2.2   Future work

For the PE project, there are numerous ways in which this project can be extended. The first task would be to continue the analysis of the current figures with different cathode materials and operating parameters. Modeling different scenarios for different materials could help with determining the appropriate material to use for certain experimental or industrial applications. For example, we could continue this research by looking at W and Au cathodes. Another direction could look at alloys for the cathode material. This could help determine which materials are more likely to follow certain emission mechanisms.

Another avenue of exploration involves examining laser properties. Through this research, we have already demonstrated that certain laser properties have more of an impact on emission than others. Instead of using generalized laser properties, as we used for this research, we could look into laser properties for specific laser types. This includes looking at the wavelengths and intensities. This could provide information on which laser would be better at initiating PE emission, and this could be looked at through experimental work.

In general, experimental exploration of these transitions between emission mechanisms appears to be the next step. Many of the papers regarding these transition points are theoretical. Obtaining more experimental data looking at the transitions between the emission mechanisms could help with refining this emission model even further.

4.3 Summary

This thesis unified emission mechanisms in different phases. The analysis began with an in-depth research review of the fundamental theories and experiments for electron emission, specifically common theoretical framework describing these mechanisms, including FN, CL, MG, MFD, and RLD. We further highlighted the steps involved in characterizing the transitions between these asymptotic solutions through "nexus theory" (Garner *et al.*, 2020b). to unify these different emission mechanisms. Much previous unification research involved linking two emission mechanisms, while more recent studies have focused on unifying multiple emission mechanisms.

The two sections in this chapter focus on two of the potential avenues of research related to nexus theory. This unification of emission mechanisms has the potential to not only work in gases, but in vapors and liquids. The model linking FN-MG-CL can be used to analyze liquid data and model emission in liquids. This initial step opens the door to using nexus theory to model the transitions between emission mechanisms in materials experiencing phase changes. Because the model connecting these emission mechanisms is developed using nexus theory, it is relatively simple to add additional mechanisms, as demonstrated in the third chapter. Using MFD and GTFP, we added PE to the current unification model to obtain various nexuses between RLD, FN, CL, MG, OL, and MFD. Now using this new model, we can further analysis the transitions between these emission mechanisms. Understanding the transitions between theses emission mechanisms can be beneficial when designing experiments and industrial applications. This research has the potential to be expanded in numerous ways, whether it be for medical, industrial, or geological applications.

REFERENCES

Aghdam, A. C. and Farouk, T., "Multiphysics simulation of the initial stage of plasma discharge formation in liquids," Plasma Sources Sci. Technol. **29**, 025011 (2020).

Akimov, P. V. and Schamel, H., "Space-charge-limited current in electron diodes under the influence of collisions," J. Appl. Phys. **92**, 1690 (2002).

Allen, A.O., *Drift Mobilities and Conduction Band Energies of Excess Electrons in Dielectric Liquids* (National Bureau of Standards, 1976).

Ang, L. K., Kwan, T. J. T., and Lau, Y. Y., "New scaling of Child-Langmuir law in the quantum regime," Phys. Rev. Lett. **91**, 208303 (2003).

Ang, L. K., Lau, Y. Y., and Kwan, T. J. T., "Simple derivation of quantum scaling in Child-Langmuir law." IEEE Trans. Plasma Sci. **32**, 410-412 (2004).

Ang, L. K., Koh, W. S., Lau, Y. Y., and Kwan, T. J. T., "Space-charge-limited flows in the quantum regime." Phys. Plasmas **13**, 056701 (2006).

Auger, M., Blatter, A., Ereditato, A., Göldi, D., Jano, S., Kreslo, I., Lüthi, M., von Rohr, C. R., Strauss, T., Weber, M. S., "On the electric breakdown in liquid argon at centimeter scale," J. Instrum., **11**, P03017 (2016).

Baker, E. B. and Boltz, H. A., "Thermionic emission into dielectric liquids," Phys. Rev. **51** (4), 275-282 (1937).

Bankston, C. P., Back, L. H., Kwack, E. Y., and Kelly, A. J., "Experimental investigation of electrostatic dispersion and combustion of diesel fuel jets," J. Eng. Gas Turb. Power **110**, 361-368 (1988).

Barbour, J. P., Dolan, W. W., Trolan, J. K., Martin, E. E., and Dyke, W. P., "Space-charge effects in field emission," Phys. Rev. **92**, 45 (1953).

Benilov, M. S., "The Child-Langmuir Law and analytical theory of collisionless to collision-dominated sheaths," Plasma Sources Sci. Technol. **18**, 014005 (2008).

Benilov, M. S. and Benilova. L. G., "Field to thermo-field to thermionic electron emission: a practical guide to evaluation and electron emission from arc cathodes," J. Appl. Phys. **114**, 063307 (2013).

Bhattacharjee, S., Vartak, A., and Mukherjee, V., "Experimental study of space-charge-limited flows in a nanogap," Appl. Phys. Lett. **92**, 191503 (2008).

Bhattacharjee, S. and Chowdhury, T., "Experimental investigation of transition from Fowler-Nordheim field emission to space-charge-limited flows in a nanogap," Appl. Phys. Lett. **95**, 061501 (2009).

Birdsall, C. K. and Bridges, W. B., *Electron Dynamics of Diode Regions* (Academic Press, New York, 1966).

Borghesani, A.F., "Electron mobility maximum in dense argon gas at low temperature," J. Electrost. **53**, 89 (2001).

Borghesani, A. F. and O'Malley, T. F., "Inhomogeneous gas model for electron mobility in high density neon gas," J. Chem. Phys. **118**, 2760 (2003).

Boyle, W. S. and Kisliuk P., "Departure from Paschen's law of breakdown in gases," Phys. Rev. **97**, 255-259 (1955).

Bragg, J.K., Sharbaugh, A.H., and Crowe, R.W., "Cathode Effects in Dielectric Breakdown of Liquids," J. Appl. Phys. **25**, 382 (1954).

Brau, C. A., "High-brightness electron beams-small free electron lasers," Nucl. Instr. and Meth. Phys. Res. A. 407, 1(1998).

Brayfield, R. S. II., Fairbanks, A. J., Loveless, A. M., Gao, S., Dhanabal, A., Li, W., Darr, C., Wu, W., and Garner, A. L., "The impact of cathode surface roughness and multiple breakdown events on microscale gas breakdown at atmospheric pressure," J. Appl. Phys. **125**, 203302 (2019).

Brodie, I. and Schwoebel, P. R., "Vacuum microelectronic devices," Proc. IEEE **82**, 1006 (1994).

Caulfield, D. D., "Predicting sonic pulse shapes of underwater spark discharges," Deep-Sea Res. **9**, 339-348 (1962).

Chen, P. Y., Cheng, T. C., Tsai, J. H., and Shao, Y. L., "Space charge effects in field emission nanodevices," Nanotechnol. **20**, 405202 (2009).

Child, C. D., "Discharge from hot CaO," Phys. Rev. (Ser. I) **32**, 492-511 (1911).

Chu, J. C. H., Grant, W. H., Almond, P. R., "A liquid ionization chamber for neutron dosimetry," Phys. Med. Biol. **25**, 1133 (1980).

Christophorou, L. G. and Siomos, K., in *Electron–Molecule Interactions and their Applications,* edited by Christophorou, L. G. (Academic Press, 1984).

Crowell, C. R., "Richardson constant and tunneling effective mass for thermionic and thermionic-field emission in Schottky barrier diodes," Solid-State Electron. **12**, 55 (1969).

Darr, A. M. and Garner, A. L., "A coordinate system invariant formulation for space-charge limited current in vacuum," Appl. Phys. Lett. **115**, 054101 (2019).

Darr, A.M., Loveless, A.M., and Garner, A.L., "Unification of field emission and space charge limited emission with collisions," Appl. Phys. Lett. **114**, 014103 (2019).

Darr, A. M., Darr, C. R., and Garner, A. L., "Theoretical assessment of transitions across thermionic, field, and space-charge limited emission," Phys. Rev. Research **2**, 033137 (2020).

Denat, A., "High field conduction and prebreakdown phenomena in dielectric liquids," IEEE Trans. Dielectr. Electr. Insul. **13**, 518 (2006).

Dotoku, K., Yamada, H., and Sakamoto, S., "Field emission into nonpolar organic liquids," J. Chem. Phys. **69** (3), 1121-1125 (1978).

Dowell, D. H., Davis, K. J., Friddell, K. D., Tyson, E. L., Lancaster, C. A., Milliman, L., Rodenburg, R.E., Aas, T., Bemes, M., Bethel, S. Z., Johnson, P. E., Murphy, K., Whelen, C., Busch, G. E., and Remelius, D. K., "First operation of a photocathode radio frequency gun injector at high duty factor," Appl. Phys. Lett. **63**, 2035 (1993).

DuBridge, L. A., "A further experimental test of Fowler's theory of photoelectric emission," Phys. Rev. **39**, 108 (1932).

DuBridge, L. A. and Roehr, W., "Thermionic and photoelectric work functions of molybdenum," Phys. Rev. 42, 52 (1932).

DuBridge, L. A., "Theory of the energy distribution of photoelectrons," Physical Rev. **43**, 727 (1933).

Dushman, S., "Electron emission from metals as a function of temperature," Phys. Rev. **21**, 623 (1923).

Dushman, S., "Thermionic Emission," Rev. Mod. Phys. **2**, 381 (1930).

D'yakonov, M. I. and Kachorovskii, V. Y., "Theory of streamer discharge in semiconductor," JETP **94,** 321 (1988).

Dynako, S. D., Darr, A. M., and Garner, A. L., "Incorporating resistance into the transition from field emission to space charge limited emission with collisions," IEEE J. Electron Dev. Soc. **7**, 650-654 (2019).

Feng, Y. and Verboncoeur, J. P., "Transition from Fowler-Nordheim field emission to space charge limited current density," Phys. Plasmas **13**, 073105 (2006).

Forati, E. and Sievenpiper, D., "Electron emission by long and short lasers: essentials for the design of plasmonic photocathodes," J. App. Phys. **124**, 083101 (2018).

Forbes, R. G., "Exact analysis of surface field reduction due to field-emitted vacuum space charge, in parallel-plane geometry, using simple dimensionless equations," J. Appl. Phys. **104**, 084303 (2008).

Forbes, R. G., "Extraction of emission parameters for large area field emitters using a technically complete Fowler–Nordheim-type equation," Nanotechnology **23**, 095706 (2012).

Forbes, R. G., "Development of a simple quantitative test for lack of field emission orthodoxy," Proc. R. Soc. A **469**, 20130271 (2013).

Forbes, R. G., Deane, J. H. B., Fischer, A., and Mousa, M. S., "Fowler-Nordheim plot analysis: a progress report," Jordan J. Phys. **8**, 125-147 (2015).

Forster, E. O., "Progress in the field of electric properties of dielectric liquids," IEEE Trans. Electr. Insul. **25** (1), 45-53 (1990).

Foster, J.E., "Plasma-based water purification: Challenges and prospects for the future," Phys. Plasmas **24**, 055501 (2017).

Fowler, R. H. and Nordheim, L., "Electron emission in intense electric fields," Proc. R. Soc. Lond. A, Math Phys. Sci. **119**, 173-181 (1928).

Fowler, R. H., "The analysis of photoelectric sensitivity curves for clean metals at various temperatures," Phys. Rev. **38**, 45 (1931).

Fraser, J. S. and Sheffield, R. L., "High-brightness injectors for RF-driven free-electron lasers," IEEE J. Quantum Electron. **23**, 1489 (1987).

Fu, Y., Zhang, P., Verboncoeur, J. P., and Wang, X., "Electrical breakdown from macro to micro/nano scales: a tutorial and a review of the state of the art," Plasma Res. Express **2**, 013001 (2020).

Garner, A. L., "Pulsed electric field inactivation of microorganisms: from fundamental biophysics to synergistic treatments," Appl. Microbiol. Biotechnol. **103**, 7917-7929 (2019).

Garner, A. L., Caiafa, A., Jiang, Y., Klopman, S., Morton, C., Torres, A. S., Loveless, A. M., and Neculaes, V. B., "Experimental validation of a compact, flexible pulsed power architecture for ex vivo platelet activation," PLoS ONE **12**, e0181214 (2017).

Garner, A. L., Loveless, A. M., Dahal, J. N., and Venkattraman, A., "A tutorial on theoretical and computational techniques for gas breakdown in microscale gaps," IEEE Trans. Plasma Sci. **48**, 808-824 (2020a).

Garner, A. L., Meng, G., Fu, Y., Loveless, A. M., Brayfield II, R. S., and Darr, A. M., "Transitions between electron emission and gas breakdown mechanisms across length and pressure scales," J. Appl. Phys. **128**, 210903 (2020b).

Gaskell, S. J., "Electrospray: principles and practice," J. MASS Spectrom. **32**, 677 (1997).

Go, D. B. and Pohlman, D. A. A., "Mathematical model of the modified Paschen's curve for breakdown in microscale gaps," J. Appl. Phys. **107**, 103303 (2010).

Go, D. B. and Venkattraman, A., "Microscale gas breakdown ion-enhanced field emission and the modified Paschen's curve," J. Phys. D **47**, 503001 (2014).

Gomer, R., "Field emission and field ionization in condensed phases," Acc. Chem. Res. **5**, 41 (1972).

Gomer, R., "Field emission, field ionization, and field desorption," Surf. Sci. **299-200**, 129-152 (1994).

Gushchin, E.M., Kruglov, A.A., and Obodovski, I.M., "Electron dynamics in condensed argon and xenon," Sov. Phys. JETP **55**, 650 (1982).

Haase, J. R. and Go, D. B., "Analysis of thermionic and thermofield emission in microscale gas discharges," J. Phys. D: Appl. Phys. **49**, 055206 (2016).

Halpern, B. and Gomer, R., "Field Emission in Liquids," J. Chem. Phys. **43**, 1069 (1965).

Halpern, B. and Gomer, R., "Field Emission in Liquids," J. Chem. Phys. **51**, 1031 (1969).

Halpern, B. and Gomer, R., "Field Ionization in Liquids," J. Chem. Phys. **51**, 1048 (1969).

Harsha, N. R. S. and Garner, A. L., "Analytical solution for space charge limited current emission from a sharp tip using variational methods," in Proc. IEEE International Vacuum Electronics Conference, Monterrey, CA, USA, October 2020, pp. 395-396.

He, S., Scharer, J., Booske, J., and Sengele, S., "One-dimensional combined field and thermionic emission model and comparison with experimental results," J. Vac. Sci. Technol. B **26**, 770 (2008).

Hirashima, Y., Kubo, M., and Murooka, Y., "Electron transport mechanisms in liquid nitrogen under high electric field," Electr. Eng. Jpn. **101**, 14 (1981).

Huang, S. S-S. and Freeman, G. R., "Density and temperature effects on electron mobilities in gaseous, critical and liquid n-hexane, cyclohexane, and cyclopentane," Can. J. Chem. **56**, 2388-2395 (1978).

Huang, S. S-S. and Freeman, G. R., "Electron transport in gaseous and liquid argon: effects of density and temperature," Phys. Rev. A **24**, 714 (1981).

Humphries, S., *Charged Particle Beams* (Wiley, New York, 1990).

Ingold, J. H., "Electron flow in gas diodes. I. transition from inertia-limited flow to mobility-limited flow," J. Appl. Phys. **40**, 55 (1969).

Ingold, J. H., "Electron flow in gas diodes. II. mobility-limited flow for collision frequency proportional to electron speed," J. Appl. Phys. **40**, 62 (1969).

Jacobsen, F.M., Gee, N., and Freeman, G.R., "Electron mobility in liquid krypton as a function of density, temperature, and electric field strength," Phys. Rev. A **34**, 2329 (1986).

Jacobsen, F.M., Gee, N., and Freeman, G.R., "Electron mobility in krypton dense gas as functions of electric field strength, temperature, and density," J. Chem. Phys. **91**, 6943 (1989).

Jaworek, A., "Electrospray droplet sources for thin film deposition," J. Mater. Sci. **42**, 266 (2007).

Jensen, K. L., "General formulation of the thermal, field and photoinduced electron emission," J. Appl. Phys. **102**, 024911 (2007).

Jensen, K. L., "A quantum dipole-modified work function for a simplified electron emission barrier," J. Appl. Phys. **111**, 054916 (2012).

Jensen, K. L., *Introduction to the physics of electron emission*, (John Wiley & Sons, Inc., Hoboken, NJ, 2017).

Jensen, K. L., "A tutorial on electron sources," IEEE Transactions on Plasma Science **46**, 1881-1889 (2018).

Jensen, K. L., "A reformulated general thermal-field emission equation," J. Appl. Phys. **126** 065302 (2019).

Jensen, K. L., O'Shea, P. G., and Feldman, D. W., "Generalized electron emission model for field, thermal, and photoemission," Appl. Phys. Lett. **81** 3867 (2002).

Jensen, K. L., Feldman, D. W., Virgo, M., and O'Shea, P. G., "Measurement and analysis of thermal photoemission from a dispenser cathode," Phys. Rev. **6**, 083501 (2003).

Jensen, K. L., Feldman, D. W., and O'Shea, P. G., "Time dependent models of field-assisted photoemission," J. Vac. Sci. and Tech. B **23**, 621 (2005).

Jensen, K. L., Feldman, D. W., Moody, N. A., and O'Shea, P. G., "A photoemission model for low work function coated metal surfaces and its experimental validation," J. Appl. Phys. **99**, 124905 (2006).

Jensen, K. L., O'Shea, P. G., Feldman, D. W., and Moody, N. A., "Theoretical model of the intrinsic emittance of a photocathode," Appl. Phys. Lett. **89**, 224103 (2006).

Jensen, K. L. and Cahay, M., "General thermal-field emission Equation", Appl. Phys. Lett. **88**, 154105 (2006).

Jensen, K. L., Moody, N. A., Feldman, D. W., Montgomery, E. J., and O'Shea, P. G., "Photoemission from metals and cesiated surfaces," J. Appl. Phys. **102**, 074902 (2007).

Jensen, K. L., Petillo, J. J., Montgomery, E. J., Pan, Z., Feldman, D. W., O'Shea, P. G., Moody, N. A., Cahay, M., Yater, J. E., and Shaw, J. L., "Application of a general electron emission equation to surface nonuniformity and current density variation," J. Vac. Sci. Tech. B. **26**, 831 (2008).

Jensen, K. L., Shiffler, D. A., Petillo, J. J., Pan, Z., and Luginsland, J. W., "Emittance, surface structure, and electron emission," Phys. Rev. **17**, 043402 (2014).

Jensen, K. L., McDonald, M., Chubenko, O., Harris, J. R., Shiffler, D. A., Moody, N. A., Petillo, J. J., and Jensen, A. J., "Thermal-field and photoemission from meso- and micro-scale features: Effects of screening and roughness on characterization and simulation," J. Appl. Phys. **125**, 234303 (2019).

Johnson, C. B. and Oskam, H. J., "Space-Charge-Limited Current in Gas Diodes," J. Appl. Phys. **42**, 5352 (1971).

Jones, H. M. and Kunhardt, E. E., "Development of pulsed dielectric breakdown in liquids," J. Phys. Appl. Phys. **28**, 178 (1995).

Jones, H. M. and Kunhardt, E. E., "Pulsed dielectric breakdown of pressurized water and salt solutions," J. Appl. Phys. **77**, 795 (1995).

Jones, H. M. and Kunhardt, E. E., "Pre-breakdown currents in water and aqueous solutions and their influence on pulsed dielectric breakdown," J. Appl. Phys. **78**, 3308 (1995).

Kahn, A., "Fermi level, work function and vacuum level," Mater. Horiz. **3**, 7 (2016).

Khatoon, S. A., Ansari, M. M., and Ashraf, S., "Effect of temperature-dependent work function and fermi energy on thermionic emission current density in graphene," AIP Conf. Proc. **1953**, 030239 (2018).

Kiejna, A. and Wojciechowski, K. F., "Work function of metals: relation between theory and experiment," Prog. Surf. Sci. **11**, 293 (1981).

Kirkpatrick, T. R. and Dorfman, J. R., "Electron mobility in gases at low temperatures: the quantum mechanical Lorentz gas, I," J. Stat. Phys. **30**, 67 (1983).

Kiziroglou, M. E., Li, X., Zhukov, A. A., de Groot, P. A. J., and de Groot, C. H., "Thermionic field emission at electrodeposited Ni–Si Schottky barriers," Solid-State Electron. **52**, 1032 (2008).

Krejci, D., Mier-Hicks, F., Thomas, R., Haag, T., and Lozano, P., "Emission characteristics of passively fed electrospray microthusters with propellant reservoirs," J. Spacecraft Rockets **54**, 447-458 (2017).

Kunhardt, E. E., "Electrical breakdown of gases: the prebreakdown stage," IEEE Trans. Plasma Sci. **8**, 130 (1980).

Lang, N. D. and Kohn, W., "Theory of metal surfaces: work function," Phys. Rev. B. **3**, 1215 (1971).

Langmuir, I. and Blodgett, K., "Currents limited by space charge between coaxial cylinders", Phys. Rev. **22**, 347-356 (1923).

Langmuir, I. and Blodgett, K., "Currents limited by space charge between concentric spheres", Phys. Rev. **24**, 49-59 (1924).

Langmuir, I., "The effect of space charge and residual gases on thermionic currents in high vacuum," Phys. Rev. **2**, 450-486 (1913).

Lau, Y. Y., Chernin, D., Colombant, D. G., and Ho, P. T., "Quantum extension of Child-Langmuir law," Phys. Rev. Lett. **66**, 1446-1449 (1991).

Lau, Y.Y., Liu, Y., and Parker, R. K., "Electron emission: from the Fowler-Nordheim relation to the Child-Langmuir law," Phys. Plasmas **1**, 2082 (1994).

Lee, M. U., Lee, J., Lee, J. K., and Yun, G. S., "Extended scaling and Paschen law for micro-sized radiofrequency plasma breakdown," Plasma Sources Sci. Technol. **26**, 034003 (2017).

Lee, M. U., Lee, J., Yun, G. S., and Lee, J. K., "Scalings and universality for high-frequency excited high-pressure argon microplasma," Eur. Phys. J. D **71**, 94 (2017).

Lemmer, K., "Propulsion for CubeSats," Acta Astronaut **134**, 231 (2017).

LePage, W. R. and DuBridge, L. A., "Electron emission into dielectric liquids," Phys. Rev. **58**, 61 (1940).

Lesaint, O., "Prebreakdown phenomena in liquids: propagation 'modes' and basic physical properties," J. Phys. Appl. Phys. **49**, 144001 (2016).

Levchenko, I., Xu, S., Mazouffre, S., Lev, D., Pedrini, D., Goebel, D., Garrigues, L., Taccogna, F., and Bazaka, K., "Perspectives, frontiers, and new horizons for plasma-based space electric propulsion," Phys. Plasmas **27**, 020601 (2020).

Lewis, T. J., "Basic electrical processes in dielectric liquids," IEEE Trans. Dielectr. Electr. Insul. **1** (4), 630-643 (1994).

Liu, W., Wang, Y., Wang, J., Wang, Y., and Vancil, B., "Emission characteristics of nanosized Scandia-doped dispenser cathodes in open electron-gun structures," IEEE Trans. Electron Devices **58**, 1241 (2011).

Lopes, M. I. and Chepel, V., "Liquid rare gas detectors: recent developments and applications," IEEE Trans. Dielectr. Electr. Insul. **10**, 994–1005 (2003).

Loscertales, I. G. and de la Mora, J. F., "Experiments on the kinetics of field evaporation of small ions from droplets," J. Chem. Phys. **103**, 5041 (1995).

Loveless, A. M. and Garner, A. L., "Scaling laws for gas breakdown for nanoscale to microscale gaps at atmospheric pressure," Appl. Phys. Lett. **108**, 234103 (2016).

Loveless, A. M. and Garner, A. L., "Scaling laws for AC gas breakdown and implications for universality," Phys. Plasmas **24**, 104501 (2017).

Loveless, A. M. and Garner, A. L., "A universal theory for gas breakdown from microscale to the classical Paschen law," Phys. Plasmas **24**, 113522 (2017).

Loveless, A. M. and Garner, A. L., "Generalization of microdischarge scaling laws for all gases at atmospheric pressure," IEEE Trans. Plasma Sci. **45**, 574 (2017).

Loveless, A. M., Meng, G., Ying, Q., Wu, F., Wang, K., Cheng, Y., and Garner, A. L., "The transition to Paschen's law for microscale gas breakdown at subatomic particles," Sci. Rep. **9**, 5669 (2019).

Luginsland, J. W., Valfells, A., and Lau, Y. Y., "Effects of a series resistor on electron emission from a field emitter," Appl. Phys. Lett. **69**, 2770 (1996).

Malayter, J. R. and Garner, A. L. "Theoretical assessment of surface waviness on work function," AIP Adv. **10**, 095110 (2020).

Marcuccio, S., Genovese, A., and Andrenucci, M., "Experimental performance of Field emission microthrusters," J. Propul. Power, **14**, 774-781 (1998).

Margulis, K., Chiou, A. S., Aasi, S. Z., Tibshirani, R. J., Tang, J. Y., and Zare, R. N., "Distinguishing malignant from benign microscopic skin lesions using desorption electrospray ionization mass spectrometry imaging," Proc. Natl. Acad. Sci. **115**, 6347 (2018).

McClintock, P. V. E., "Field emission in liquid helium," Phys. Lett. **29A**, 453-454 (1969).

McClintock, P.V.E., "Field emission and field ionization in liquid ^{3}He above 0.25 K," J. Low Temp. Phys. **11**, 15 (1973).

Meng, G., Ying, Q., Loveless, A. M., Wu, F., Wang, K., Fu, Y., Garner, A. L., and Cheng, Y., "Spatio-temporal dynamics of pulsed gas breakdown in microgaps," Phys. Plasmas **26**, 014506 (2019).

Michelato, P., "Photocathodes for RF photoinjectors," Nucl. Instrum. Methods Phys. Res. A **393**, 455 (1997).

Millikan, R. A. and Eyring, C. F., "Laws governing the pulling of electrons out of metals by intense electrical fields," Phys. Rev. **27**, 51 (1926).

Modinos, A., *Field, Thermionic, and Secondary Electron Emission Spectroscopy*, (Plenum, New York, 1984).

Mott, N. F. and Gurney, R. W., *Electronic Processes in Ionic Crystals*, (Clarendon Press, Oxford, 1940).

Murphy, E. L. and Good, R. H., "Thermionic emission, field emission, and the transition region," Phys. Rev. **102**, 1464 (1956).

Muñoz, R. C. and Holroyd, R. A., "The effect of temperature and pressure on excess electron mobility in n-hexane, 2,2,4-trimethylpentane, and tetramethylsilane," J. Chem. Phys. **84,** 5810 (1986).

Muñoz, R. C., Holroyd, R. A., Itoh, K., Nakagawa, K., Nishikawa, M., and Fueki, K., "Excess electron mobility in hydrocarbon liquids at high pressure," J. Phys. Chem. **91**, 4639 (1987).

Naugolnykh, K. A. and Roy, N. A., *Electrical Discharges in Water. A Hydrodynamic Description* (National Technical Information Service, 1974).

Neal, R. E., Rossmeisl, J. H., D'Alfonso, V., Robertson, J. L., Garcia, P. A., Elankumaran, S., and Davalos, R. V., "In vitro and numerical support for combinatorial irreversible electroporation and electrochemotherapy glioma treatment," Ann. Biomed. Eng. **42**, 475 (2014).

Olson, A. H. and Sutton, S. P., "The physical mechanisms leading to electrical breakdown in underwater arc sound sources," J. Acoust. Soc. Am. **94**, 2226–2231 (1993).

O'Shea, P. G., Bender, S. C., Byrd, D. A., Early, J. W., Feldman, D. W., Fortgang, C. M., Goldstein, J. C., Newnam, B. E., Sheffield, R. L., Warren, R. W., and Zaugg, T. J., "Ultraviolet free-electron laser driven by a high-brightness 45-MeV electron beam," Phys. Rev. Lett. **71**, 3661 (1993).

O'Shea, P. G., "Reverisble and irreversible emittance growth," Phys. Rev. E. **57**, 1081 (1998).

O'Shea, P. G. and Freund, H. P., "Free-electron lasers: status and applications," Science **292**, 5523 (2001).

Padovani, F. A. and Stratton, R., "Field and thermionic-field emission in Schottky barriers," Solid-State Electronics **9**, 695-707 (1966).

Paschen, F., "Über die zum Funkenübergang in luft, Wasserstoff und Kohlensäure bei verschiedenen Drucken erforderliche potentialdiffenrenz," Ann. Phys. **273**, 69 (1889).

Phan, N., Beaumont, B., Bouman, N., Clayton, S., Currie, S., Ito, T., Ramsey, J., Seidel, G., and Wei, W., "Understanding electrical breakdown in liquid helium with a statistical distribution-based study," in Fall Meeting of the APS Divison of Nuclear Physics Virtual (2020).

Qian, J., Joshi, R. P., Kolb, J., Schoenbach, K. H., Dickens, J., Neuber, A., Butcher, M., Cevallos, M., Krompholz, H., Schamiloglu, E., Gaudet, J., "Microbubble-based model analysis of liquid breakdown initiation by a submicrosecond pulse," J. Appl. Phys. **97**, 113304 (2005).

Rechtien, R. D., Hambacker, K. L., and Ballard, R. F., "A high-frequency sparker source for the borehole environment," Geophysics **58**, 660–669 (1993).

Reiser, M., *Theory and Design of Charged Particle Beams* (Wiley-VCH, New York, 1994).

Richardson, O. W., "On the negative radiation from hot platinum," Proc. Cambridge Philos. Soc. **11**, 286 (1901).

Richardson, O. W., "XIII. The electrical conductivity imparted to a vacuum by hot conductors," Philosophical Trans. Proc. R. Soc. London, Ser. A **201**, 497 (1903).

Richardson, O. W., "The emission of electrons from tungsten at high temperatures- an experimental proof that the electric current in metals is carried by electrons," Science **38**, 57 (1913).

Richardson, O. W., "The influences of gases on the emission of electrons and ions from hot metals," Proc. R. Soc. London, Ser. A **91**, 524 (1915).

Richardson, O. W., *The Emission of Electricity from Hot Bodies*, (Longmans, Green and Company, New York, 1916).

Richardson, O. W. and Young, A. F. A., "The thermionic work functions and photo-electric thresholds of the alkai metals," Proc. R. Soc. London, Ser. A **107**, 377 (1925).

Röhr, J. A., Moia, D., Haque, S. A., Kirchartz, T., and Nelson, J., "Exploring the validity and limitations of the Mott–Gurney law for charge-carrier mobility determination of semiconducting thin-films," J. Phys. Condens. Matter 30, 105901 (2018).

Rokhlenko, A., Jensen, K. L., and Lebowitz, J. L., "Space charge effects in field emission: one dimensional theory," J. Appl. Phys. **107**, 014904 (2010).

Schmidt, W. F., "Electron mobility in nonpolar liquids: the effect of molecular structure, temperature and electric field," Can. J. Chem. **55**, 2197 (1977).

Schmidt, W. F., "Electronic conduction processes in dielectric liquids," IEEE Trans. Electr. Insul. **EI-19**, 389 (1984).

Schoenbach, K., Kolb, J., Xiao, S., Katsuki, S., Minamitani, Y., and Joshi, R., "Electrical breakdown of water in microgaps," Plasma Sources Sci. Technol. **17** (2), 024010 (2008).

Schoenbach, K. H. and Becker, K. H., "20 years of microplasma research: a status report," Eur. Phys. J. D **70**, 29 (2016).

Segev, G., Rosenwaks, Y., and Kribus, A., "Loss mechanisms and back surface field effect in photon enhanced thermionic emission converters," J. Appl. Phys. **114**, 044505 (2013).

Schnyders, H., Rice, S. A., and Meyer, L., "Electron drift velocities in liquefied argon and krypton at low electric field strengths," Phys. Rev. **150**, 127 (1966).

Sharbaugh, A. H., Devins, J. C., and Rzad, S. J., "Progress in the field of electric breakdown in dielectric liquids," IEEE Trans. Electr. Insul. **EI-13**, 249 (1978).

Shneider, M., Pekker, M., and Fridman, A., "Theoretical study of initial stage of sub-nanosecond pulsed breakdown in liquid dielectrics," IEEE Trans. Dielectr. Electr. Insul. **19**, 1579–1582 (2012).

Shneider, M. N. and Pekker, M., "Cavitation in dielectric fluid in inhomogeneous pulsed electric field," J. Appl. Phys. **114**, 214906 (2013).

Tobazcon, R., "Prebreakdown phenomena in dielectric liquids," IEEE Trans. Dielectr. Electr. Insul. **1**, 1132 (1994).

Toijala, H., Eimre, K., Kyritsakis, A., Zadin, V., and Djurabekova, F., "Ab initio calculation of field emission from metal surfaces with atomic-scale defects," Phys. Rev. B **100**, 165421 (2019).

Townsend, J. S., "XVII. The conductivity produced in gases by the motion of negatively charged ions," Lond. Edinb. Dublin Philos. Mag. J. Sci. **1**, 198–227 (1901).

Townsend, J. S. *Electricity in Gases* (The Clarendon Press, Oxford, 1915).

Venkattraman, A. and Alexeenko, A. A., "Scaling law for direct current field emission-driven microscale gas breakdown," Phys. Plasmas **19**, 123515 (2012).

Venkattraman, A., "Generalized criterion for thermo-field emission driven electrical breakdown of gases," Appl. Phys. Lett. **104**, 194101 (2014).

Vogel, C. B., "A seismic velocity logging method," Geophysics **17**, 586-597 (1952).

Wada, T. and Freeman, G. R., "Density and temperature effects on electron mobilities in gaseous butene isomers," Can. J. Chem. **57**, 2716-2726 (1979).

Wada, T. and Freeman, G.R., "Temperature, density, and electric-field effects on electron mobility in nitrogen vapor," Phys. Rev. A **24**, 1066 (1981).

Wang, Y., Wang, J., Liu, W., Li, L., Wang, Y., and Zhang, X., "Correlation between emission behavior and surface features of scandate cathodes," IEEE Trans. Electron Devices **56**, 776 (2006).

Wu, Y., Duong, A., James, L., and Wyslouzil, B. E., in *The Delivery of Nanoparticles*, edited by Hashim, A. A. (IntechOpen, 2012).

Xu, N., Chen, J., and Deng, S., "Physical origin of nonlinearity in the Fowler–Nordheim plot of field-induced emission from amorphous diamond films: Thermionic emission to field emission," Appl. Phys. Lett. **76**, 2463 (2000).

Xu, L., Garner, A. L., Tao, B., and Keener, K. M., "Microbial inactivation and quality changes in orange juice treated by high voltage atmospheric cold plasma," *Food Bioprocess Technol.* **10**, 1778-1791 (2017).

Zahn, M., Ohki, Y., Fenneman, D. B., Gripshover, R. J., and Gehman, V. H., "Dielectric properties of water and water/ethylene glycol mixtures for use in pulsed power system design," Proc. IEEE **74**, 1182 (1986).

Zhang, P., Valfells, A., Ang, L. K., Luginsland, J. W., and Lau, Y. Y., "100 years of the physics of diodes," Appl. Phys. Rev. **4**, 011304 (2017).